STUDIES IN NEUTRON PHASE SPACE COOLING FOR COLD AND ULTRA-COLD NEUTRON SOURCES

Yunchang Shin

Submitted to the faculty of the University Graduate School

in partial fulfillment of the requirements

for the degree

Doctor of Philosophy

in the Department of Physics

Indiana University

September 2008

UMI Number: 3337262

INFORMATION TO USERS

The quality of this reproduction is dependent upon the quality of the copy submitted. Broken or indistinct print, colored or poor quality illustrations and photographs, print bleed-through, substandard margins, and improper alignment can adversely affect reproduction.

In the unlikely event that the author did not send a complete manuscript and there are missing pages, these will be noted. Also, if unauthorized copyright material had to be removed, a note will indicate the deletion.

UMI®

Accepted by the Graduate Faculty, Indiana University, in partial fulfillment of the requirements of the degree of Doctor of Philosophy.

Doctoral
Committee

—————————————————————
W. Michael Snow, Ph.D.
(Principal Advisor)

—————————————————————
Chen-Yu Liu, Ph.D.

—————————————————————
David V. Baxter, Ph.D.

August 15 2008

—————————————————————
Herman Nann, Ph.D.

ii

Acknowledgements

Abstract

This thesis addresses problems in the phase space compression of neutrons in two different energy regimes. The first part applies to the cold neutron regime. We constructed a microscopic model for the neutron dynamic structure factor $S(Q,\omega)$ of solid methane in phase II. The model treats the effects of molecular translations, intra-molecular vibrations and intra-molecular rotations as uncoupled. Total scattering cross sections were calculated from the model for the incident neutron energies of 0.1 meV $\sim$ 1 meV and compared with existing data. This model was tested by calculating and measuring the neutron brightness from the solid methane cold neutron moderator of the Low Energy Neutron Source (LENS) at the Indiana University Cyclotron Facility (IUCF) at 4K and 20K. Within the expected accuracy of our approximate approach, the model matches the measured neutron spectral intensity. We have also used the model to guide future investigations into other cold neutron moderator media in an attempt to reach the "very cold neutron" (VCN) energy regime.

The second part describes the study of solid oxygen as an ultra-cold neutron moderating medium. Ultra-cold neutrons (UCN) are neutrons with energy of a few hundred neV. A UCN source with higher intensity is necessary to measure fundamental properties of the neutron such as the neutron lifetime or the neutron electric dipole moment (EDM). Solid oxygen may be an attractive choice as a UCN source. Theoretical calculations for a perfect solid crystal predict high UCN brightness is possible from solid oxygen. However, it has been experimentally shown that the UCN production rate from solid oxygen depends strongly on the crystal condition, especially at low temperature. We tested crystal growth of solid oxygen over a wide range of temperatures and in external magnetic fields. In addition, the UCN production rate in solid oxygen was measured on FP-12 at Los Alamos Neutron Science Center (LANSCE).

Contents

List of Tables

List of Figures

1

Introduction

In this chapter, some of basic concepts used in this thesis such as the interaction of slow neutrons with matter, neutron moderation, and collective modes are discussed.

1.1   Interaction of Slow Neutrons with Matter

Neutrons with energies of less than a few meV are collectively referred to as "Slow Neutrons". The slow neutron energy ranges from the cold neutron region, in which the neutron energies are of the order of meV, and also the very cold neutron region, which extends from 1 meV to a few μeV or, in temperature units, from less than 10 K to approximately 10 mK. Neutrons whose energies are much less than few hundred neV are described as ultra-cold neutrons (UCN). Fig. 1.1 shows the

classification of the neutrons in terms of their energy, wavelength and temperature.
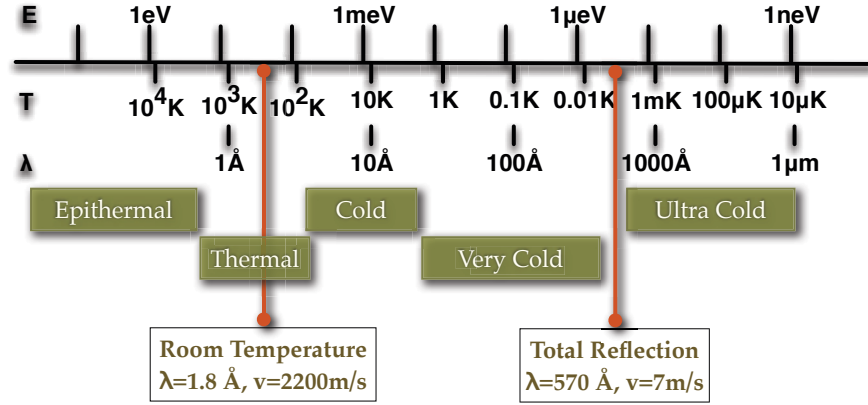
Figure 1.1: Classification of neutrons in terms of their energy, wavelength and temperature.

Many phenomena in slow neutron physics can be treated from a neutron optics point of view because of their wave properties. The wave properties of slow neutrons are responsible for typical optical phenomena, such as the refraction of neutron waves at the boundary between two media, total internal reflection, diffraction and small angle scattering[1].

Slow neutrons have been used in the analysis of the atomic structure of matter as in diffraction studies of hydrogenous compounds. Slow neutrons are also widely used in studies of crystals and liquids. Analysis of slow neutron scattering data provides information about the vibration frequency spectrum of the crystals lattice and phonon dispersion curve[2][3]. In liquids, the atomic dynamics is

particularly complicated and slow neutron scattering gives valuable information about the motion of atoms or molecules and about the diffusion mechanism[4].

Slow neutrons are also used for studying the properties of magnetic materials. They can be used to determine the orientation of atomic magnetic moments in magnetic materials and to study the magnetic dynamics of crystals[5].

Slow neutrons were originally employed in nuclear physics experiments[6]. Polarized neutrons are used to determine nuclear magnetic moments. Moreover, slow neutrons are used in investigations of the properties of the neutron itself, namely, the magnetic dipole moment, spin, half life and in searches for the electric dipole moment[7]. Studies of the neutron decay give valuable information about the nature of the weak interaction and the problem of parity violation in weak interactions[8].

With these two principal areas of study in slow neutron physics, the scattering of slow neutrons is also important in producing and moderating neutrons in low energy neutron sources. In this case, the energy transfer between neutrons and the moderating media, which is an effect not described with neutron optics, must be taken into account[9]. This energy transfer ensures that the neutrons gradually come into thermal equilibrium with the moderator. The process leading to equilibrium is often called "Neutron Thermalization", and the understanding of this process is important in the design of slow neutron sources[10][11].

1.2 Neutron Moderation

The phase space compression of neutron ensembles, usually called "Neutron Moderation", is concerned with the energy, space and time distribution of neutrons in a moderating medium. The fundamental object of interest in neutron moderation is $f(\vec{r}, \vec{v}, t)$, the phase space distribution function, where $f(\vec{r}, \vec{v}, t)d\vec{r}d\vec{v}$ is the average number of neutrons in the phase space element $d\vec{r}d\vec{v}$ at time t. Since the density of neutrons is orders of magnitude lower than the density of scatterers in a medium, neutron-neutron scattering can be ignored, and since the mean free path of neutrons in matter is much larger than the separation between atoms in the medium, the neutron motion between collisions can be approximated as classical motion with velocity $\vec{v}$. This leads to a linear integral equation for the neutron phase space density of the form

$$(\frac{\partial}{\partial t} + \vec{v} \cdot \vec{\Delta})f(\vec{r}, \vec{v}, t) = - \rho v \sigma_a(v) f(\vec{r}, \vec{v}, t) \tag{1.1}$$

$$+ \int [\rho v_0 \sigma_s(\vec{v}_0, \vec{v}) f(\vec{r}, \vec{v}_0, t) - \rho v \sigma_s(\vec{v}, \vec{v}_0) f(\vec{r}, \vec{v}, t)] d\vec{v}_0$$

where $v = |\vec{v}|$ is the neutron speed, ρ is the density of the medium, $\sigma_a(v)$ is the neutron absorption cross section, and $\sigma_s(\vec{v}_0, \vec{v})$ is the scattering kernel. The first term in the integral can be understood to represent "downscattering" of the neutron of velocity $\vec{v}_0$ to velocity $\vec{v}$ and the second term can be understood to represent

"upscattering" of the neutron of velocity $\vec{v}$ to velocity $\vec{v}_0$. In terms of the double differential scattering cross section $d^2\sigma$, defined as the average number of incident particles with velocity $\vec{v}_0$ scattered into the volume element $d\vec{v}$ per atom per unit time per unit incident flux, the scattering kernel is defined by

$$d^2\sigma = \sigma_s(\vec{v}_0, \vec{v})d\vec{v}, \tag{1.2}$$

which is expressed in spherical coordinates in terms of the scattered neutron energy $E = \frac{1}{2}mv^2$. If (θ, ϕ) are the polar coordinate of $\vec{v}$ with respect to $\vec{v}_0$ as polar axis, then $d\vec{v} = v^2 dv \sin\theta d\theta d\phi = \frac{v}{m} d\Omega dE$. The double differential scattering cross section becomes

$$\frac{d^2\sigma}{d\Omega dE} = \frac{v}{m}\sigma_s(\vec{v}_0, \vec{v}). \tag{1.3}$$

On the other hand, the usual expression for the double differential scattering cross section is

$$\frac{d^2\sigma}{d\Omega dE} = \left(\frac{\sigma_s}{4\pi\hbar}\right)\frac{v}{v_0}S(\vec{Q}, \omega), \tag{1.4}$$

where $S(\vec{Q}, \omega)$ is the dynamic structure factor[53], σ_s is the bound scattering cross section per atom, and $\vec{Q}$ and ω are the momentum and energy transfers from the neutron to the medium. Comparing Eq. 1.3 and Eq. 1.4, one can see that the

scattering kernel is directly proportional to the dynamic structure factor,

$$\sigma_s(\vec{v_0}, \vec{v}) = (\frac{m\sigma_s}{4\pi\hbar v_0})S(\vec{Q}, \omega). \qquad (1.5)$$

Neutron moderation theory has been developed for nuclear engineering and related applications in the energy regime between the typical energy which neutrons possess upon liberation from nuclei (MeV) to the kinetic energies of atoms in matter at room temperature ($\sim$25 meV)[12]. Since these energies are large compared to the kinetic energy and the binding energy of the atoms in the moderating medium, the total cross section is given to a good approximation by the incoherent sum of the scattering cross sections from the individual atoms in the medium. In this limit, the theory of neutron moderation only needs to apply energy and momentum conservation to a sequence of collisions of neutrons of mass m and initial energy E with target nuclei of mass M and zero kinetic energy. Such an analysis forms the core of neutron moderation theory in nuclear reactors. The large number of collisions typically needed to reduce the energy of a neutron by several orders of magnitude leads inevitably to neutron emission sources which are incoherent [12][13][14].

For neutron energies at or below the energies of motion of the moderating medium, however, the situation is qualitatively different. In this case the neutron

wavelength is larger than the separation between atoms in the medium, and in this case the scattering exhibits strong interference effects which depend on the details of the structure and modes of motion of the medium. There is also the quantum mechanical issue of the individual neutron collision events and the essentially classical neutron transport problem dealing with the distribution of neutrons resulting from multiple collisions [15].

Furthermore, the inelastic fraction of the total cross section, which the essential component for phase space compression, decreases as the neutron energy drops below the binding energy and the ~meV excitation energies of collective modes in the medium. In practice, the only efficient way at present to increase the neutron phase space density is through collisions in a medium[3].

In the individual scattering events of neutrons with molecules in the moderating medium, the basic problem is to understand the interchange of energy between the neutron and the states of excitation in the moderator. In a pseudo-potential approximation of neutron-nuclear interaction[16], the scattering of slow neutrons by free nuclei at rest is simply described with their scattering lengths which are measured for essentially all stable nuclei. Then, the understanding of the relevant molecular excitation is the main key to understand the slow neutron scattering process in moderator media[15]. For crystals, these can be inter-molecular vibrations (or quantized lattice vibrations), intra-molecular vibrations, intra-molecular

rotations or spin lattice excitations.

The amount of phase space compression per collision for slow neutrons in a moderating medium, therefore, tends to decrease as the energy decreases. In principle, we can continue to increase the phase space density in a neutron moderator indefinitely, in the absence of absorption, by cooling the medium to $T = 0$ K and allowing the neutrons to undergo an arbitrary number of collisions. In practice, however, the finite neutron absorption cross section of all media other than ^{4}He limits the number of collisions that can be tolerated. Then, once again, the amount of phase space compression per collision depends on the microscopic properties of the medium even at $T = 0$ K. In addition, the inelastic modes available in a condensed medium tend to freeze as $T \rightarrow 0$ K, thereby reducing the efficiency of the moderating medium even further.

As can be seen from the Boltzmann equation for neutron transport in Eq. 1.1, the rate of phase space compression per collision is proportional to the neutron dynamic structure factor $S(Q, \omega)$ in the medium, where $\omega = E_f - E_i$ and $\vec{Q} = \vec{k_f} - \vec{k_i}$ and E_f, E_i, $\vec{k_f}$, $\vec{k_i}$ are the final and initial neutron energies and momenta. In the theory of neutron phase space compression in the slow neutron regime, we are especially interested in the behavior of $S(Q, \omega)$ as $\omega \rightarrow 0$. This is because the width of the distribution of neutrons in phase space that we are interested in cooling is typically large compared to the range in (Q, ω) space where $S(Q, \omega)$ is large. When

the latter range is defined by the dispersion relation of a well-defined elementary excitation of the medium such as a phonon, magnon, libron, etc., for example, $S(Q, \omega)$ is large only over a narrow ridge in (Q, ω) space.

If the neutrons of interest for cooling also possessed a phase space distribution of comparable width, the obvious optimal solution to neutron cooling would be to match the elementary excitation spectrum to the neutron phase space to be cooled and reduce the neutron energy to zero by the creation of a single elementary excitation, with the refrigerator that maintains the moderating medium at $T = 0$ K providing the dissipation required for phase space compression.

This strategy is used in so-called superthermal neutron moderators optimized for the creation of ultracold neutrons[17]. For cooling a broader phase space distribution of neutrons to energies in the $100 \, \mu$eV $\sim$ meV range, however, multiple collisions are essential, and $S(Q, \omega)$ must therefore possess some strength near $\omega \to 0$ so that most neutrons in the distribution have energy losses ω_i in some sequence of collisions $S(Q, \omega_i)$ that can allow them to approach $E_f \to 0$. These considerations guide the search for improved neutron moderating media into some obvious directions.

Although the energy transfer cross section for slow neutrons is the main concern in the neutron moderation, the space and energy distributions of the neutrons are also important problems. If the moderator is long enough that the number of

scattering collisions is sufficiently large before absorption, neutrons may come to thermal equilibrium within the moderator. The thermal neutron flux spectrum is approximately a Maxwellian distribution,

$$\phi_M(E) = \frac{1}{(k_B T)^2} E \exp\left(-\frac{E}{k_B T}\right), \tag{1.6}$$

where k_B is Boltzmann's constant and T is the absolute temperature of the moderator.

The neutron thermalization problem was first formulated by Wigner and Wilkins in 1944[18]. In 1960, McReynold and Wittermore described the measurements of the cold neutron spectrum and the neutron thermalization in liquid and solid methane and in liquid hydrogen for cold neutron source design[19]. Later research also investigated liquid deuterium and D_2O ice[20]. Given the engineering constraints from heating of the moderator from fast neutrons and gamma radiation, liquid H_2 and D_2 quickly become the main choices for cold neutron sources at research reactors.

The development of pulsed neutron sources motivated more research on neutron moderation in other materials, since, in this case, the emission time distribution of the neutrons from the moderator is also important[21]. In 1982, Inoue *et al.* extended this study to various materials in their cold neutron moderator using a

pulsed neutron source and studied the neutron thermalization and neutron flux of different candidate materials[22]. In this experiment, they chose four different hydrogenous materials, CH_4, C_2H_6, H_2 and H_2O. The experimental spectra were obtained from these materials at various solid and liquid temperatures. They also investigated the behaviors of the effective neutron spectrum temperature of three moderators, CH_4, C_2H_6, H_2, as a function of moderator temperature. As seen in Fig. 1.2, the neutrons do not reach thermal equilibrium. It was suggested that this was caused by the low cross section for small energy transfers and competition between the slowing down and absorption of neutrons. Finally, this test showed that solid methane at low temperature was one of the most efficient cold neutron moderator media. Research on neutron moderator design and materials for pulsed neutron sources has continued[23].

1.3   Elementary Excitations

Crystalline solids, like poly-atomic molecules, contain a large number of strongly interacting particles. The energy levels of such systems cannot easily be deter-mined from first principles. A method of elementary excitations can be used to approximate the dynamics of the crystal[24].

A motion in a crystal involves all the particles in the crystal by the translational
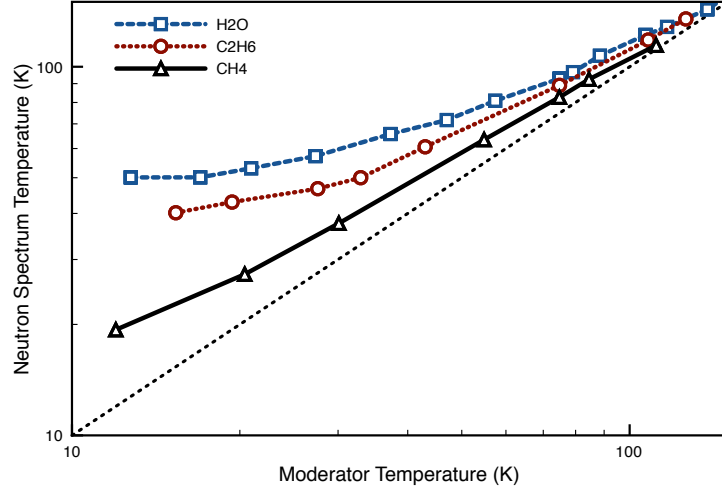
Figure 1.2: Neutron spectrum temperature versus moderator temperature[22].

symmetry of its lattice. Because of this symmetry, all the particles with a unit cell of the crystal can be treated as physically equivalent to those in any other unit cell. The excitation occurring in the crystal, therefore, can be transmitted throughout the entire set of particles. It is called "collective mode" [25].

The collective modes of a crystal can propagate in the form of plane waves throughout the specimen because of the translational symmetry of the crystal. At low temperatures, there are only a small number of collective modes populated in a crystal and they can be treated as independent. As a result of the quantization of waves propagating through the periodic structure, quasi-particles describing the collective modes in a crystal are called "elementary excitations". The dispersion

law for the excitations is strongly dependent on the dynamic properties of the particular crystal[24].

In terms of elementary excitations, the thermal energy of a crystal can be determined by the occupation of different excitation branches. For example, thermal lattice vibrations give rise to collective waves in terms of normal vibrations of the lattice. Quantization of these waves leads to quasi-particles known as "phonons". The collective modes in a ferromagnet, which were referred to as spin waves, are similarly associated with quasi-particles known as "magnons".

Each excitation branch (phonon, magnon, etc.) is characterized by a definite excitation spectrum $g_i(E)$, where the subscript i represents the branch. To determine the thermodynamic energy of the crystal, we must know the excitation spectra of all the branches and the statistics obeyed by the quasi-particles belonging to different branches. In the first approximation, in which each branch is treated as independent, the energy of the crystal can be expressed in the form [26]

$$E = \sum_i \int dE \, E f_T^i(E) g_i(E),$$
(1.7)

where the temperature dependence is determined by the thermal occupation factor f_T^i.

For example, a large number of phonons can be excited in a given state in any

system. In this case, the phonons obey Bose-Einstein statistics and the energy of the crystal is given by[27]

$$E = \int dE \frac{E}{\exp(E/k_B T) - 1} g_{ph}(E).$$ (1.8)

where $g_{ph}(E)$ is the phonon spectrum, which is the spectrum of normal vibration modes of the lattice.

In the case of a ferromagnet below the Curie point, both chemical and magnetic periodic structures can be present[10]. Therefore, both phonons and magnons can exist simultaneously. In this case, phonon-phonon, magnon-phonon and magnon-magnon interactions can all exist. These collision processes give rise to an equilibrium in the crystal. It had been shown that the interaction of spin waves with one another is typically stronger than the interaction of spin wave with the lattice. As a consequence, the time necessary to establish a relaxation in the magnon gas through magnon-magnon collisions is much shorter than the time required for magnon-phonon collision to bring the magnons into equilibrium with the phonons at low enough temperature[28]. Therefore, the temperature of spin waves and the lattice may differ from one another.

This phenomenon is also important when the excitation branch must take into account nuclear spin species. The excitation branch corresponding to molecular

rotations normally has multiple discrete excitation levels, either simple two levels or more complicated levels structure depending on the number of atoms participating in the motion. These level structures depend on the nuclear spin species of the molecule. Even in the simple case of hydrogen or deuterium, the very different scattering cross section of two different molecular species, ortho and para, depending on total nuclear spin states, is very important in the study of both the neutron scattering and UCN related fields. The nuclear spin species conversion in other hydrogenous molecules such as solid methane at low temperatures is also important for neutron moderation[29][30].

1.4   Motivations

There were motivations making this research interesting for practical applications to the low energy neutron source (LENS) at Indiana University Cyclotron Facility (IUCF). These include

1) the development of theoretical understanding of cold neutron scattering in low temperature solid methane,

2) the measurement of neutron energy spectra in LENS to make a comparison of theory with experiment,

3) the development of new concept to allow very cold neutron source to be

possible,

4) and the experimental study of solid oxygen for ultra-cold neutron production.

In this thesis, these issues will be the main topics in each chapter. Chapters 2 and 3 mainly deal with cold neutron scattering in phase II solid methane. Our main goal in chapter 2 is to understand cold neutron scattering in solid methane with different elementary excitations, to develop a theoretical formalism to get physical insight and to calculate the total scattering cross section, dynamic structure factor and frequency spectrum at different moderator temperatures.

We discuss extensively the experimental techniques and the results of neutron spectra measurement in chapter 3. Our objectives in this chapter are to see if these measurements agree with our predictions based on the formalism which we develop in chapter 2. The consideration of nuclear spin conversion in methane and the operation of the solid methane moderator at low temperatures form the subject matter of chapter 3.

Chapter 4 presents a specific idea of a possible moderating medium for a very cold neutron source. In order to have physical understanding of neutron moderation in a moderator, we decompose the collective modes of solid methane in our formalism and study the relationship of each collective mode with the neutron energy spectrum which would be produced in LENS TMR. In particular, we extract

the neutron effective spectrum temperature as a function of moderator temperature down to 4K and compare with Inoue *et al.*[22]. From this study, we propose a specific material, methane clathrate hydrate, as a very cold neutron moderator medium of practical interest.

In chapter 5, we discuss an experimental setup for our study of ultracold neutron production in oxygen using magnetic excitations of the solid system. We make a detailed description of our setup and operations and present our studies of the magnetic field influence on the formation of polycrystalline solid oxygen. This chapter also presents preliminary experimental results on the UCN production with this setup measured at LANSCE.

2

The Neutron Dynamic Structure

Factor of Solid Methane in Phase II

We have constructed an approximate microscopic model for the neutron dynamic structure factor of solid methane in phase II. We expect this model to apply for neutron energies below 1 eV at pressures near 1 bar and temperatures below 20 K where methane exists as a mixed phase of free rotors and hindered rotors of the tetrahedral molecules in the unit cell. Matrix elements needed to calculate the dynamic structure factor $S(Q, \omega)$ are adapted from earlier works by Ozaki *et al.*[31] [32]. The model treats the motions of molecular translations, intra-molecular vibrations and the free and hindered rotations of methane molecule as uncoupled. Total scattering cross sections calculated from the model agree with the cross section measurements by Grieger *et al.*[33] for the incident neutron energies of 0.5 meV $\sim$

1 eV. The effective density of states extracted from the model was compared with the Harker & Brugger frequency spectrum extracted from neutron scattering measurements conducted at 22 K[34]. Using this model, we can also isolate the separate contributions of the various orientational modes to the inelastic cross section in the cold neutron energy regime.

2.1   Introduction

Neutron scattering from solid methane has special importance for cold neutron moderation for a number of reasons. First of all, solid CH_4 possesses a high number density of hydrogen atoms, and since the isolated hydrogen atoms have a very large scattering cross section, the neutron mean free path is small and the neutron brightness emitted from such a source can be high. Second, the high symmetry of the CH_4 molecules leaves a significant fraction of the methane molecules free to rotate in the solid phase even close to $T \sim 0$ K. This property is shared by only a few other molecular solids such as solid hydrogen, γ-picolene, methane clathrate and their deuterated versions [35]. The resulting inelastic rotational modes are responsible for the experimental observation that solid methane is the brightest known cold neutron moderating medium[36].

Solid methane undergoes a phase transition at $T \sim 20$ K. Below this temperature, only 1/4 of the molecules remain freely rotating. The remaining molecules undergo librations and tunneling motions between equivalent librational ground states. We use the term "orientational modes" to refer collectively to these three possible motions (free rotation, libration, or tunneling between local orientational minima). Each of these modes can contribute to neutron moderation, but the relative contributions of each to the effectiveness of methane as a moderator below 20 K has not previously been clearly established.

The purpose of this work is to present a description of the dynamics of neutron scattering of solid methane in phase II and construct the dynamic structure factor $S(Q, \omega)$. The complete dynamics of the crystal include inter-molecular vibrations, intra-molecular vibrations and intra-molecular rotations. For methane molecules in the low temperature solid state, these collective modes are sufficiently decoupled to treat them as independent modes. Our model involves this specific assumption, which is necessary to obtain $S(Q, \omega)$ with reasonable accuracy from the first principles. Similar approaches have been used by Nelkin[37] in the analysis of neutron scattering from water and also used later in the analysis of the solid methane total cross section data by Grieger *et al.* [33].

Such an analytical treatment can also be easily applied to gain physical insight

into the cold neutron moderation process. It may be useful to analyze quantitatively the dependence of cold neutron brightness upon the individual dynamic modes of solid methane. It has been speculated that the cold neutron brightness from a methane moderator would be enhanced if the motion of solid CH_4 can be modified in some way so as to free all rotational modes. The motivation for this idea was mainly due to the high neutron cross section for the free rotation mode of the methane molecule. However, the librational and tunneling motions also introduce new energy levels into the excitation spectrum for the material, some of which are at lower energy than those of the free rotor states, and therefore these cannot be neglected in a complete description of the inelastic spectrum. Even though there was an interesting approximate analysis by Utsuro[38] of this issue, the relative importance of the various orientational modes to the effectiveness of neutron moderation at temperatures below 20K was not established.

Fortunately, the librational and tunneling energy spectra for solid phase II CH_4 have been measured[39][40]. These results can be incorporated directly into the inelastic neutron scattering calculation in combination with the matrix elements corresponding to different transitions. The matrix elements needed to calculate the dynamic structure factor from inter-molecular rotations were already calculated by Ozaki *et al.*[31][32], and we use these calculations in our work. In addition, the identity of four hydrogen atoms, which correlates the formation of the rotational

and spin wave functions through the overall symmetry they must possess under identical particle interchange, simplifies the calculations by reducing further the number of possible states.

Very recently, another interesting model for $S(Q, \omega)$ for solid phase II CH_4 has appeared [41] which uses a different approach and set of approximations for a different purpose. In particular, an incoherent approximation for the inelastic scattering is applied within the context of a model using a frequency spectrum approach to the description of the dynamic structure factor, and the effect of the spin correlations on the intramolecular contribution to the scattering function is included explicitly. This model agrees with the cross section data and also shows clearly that the spin correlations among the protons in the CH_4 molecule that come from identical particle constraints make an important contribution to the elastic cross section at low neutron energies. Our approach differs in that it explicitly accounts for the microscopic dynamics associated with the orientational degrees of freedom. This provides important insight into the relative importance of these various orientational modes in determining the unique low-temperature moderation characteristics of methane.

The remainder of the chapter is organized as follows. Section 2.2 discusses the structure of solid methane in phase II and summarizes relevant past works on both theoretical descriptions of the states of the system and key experimental
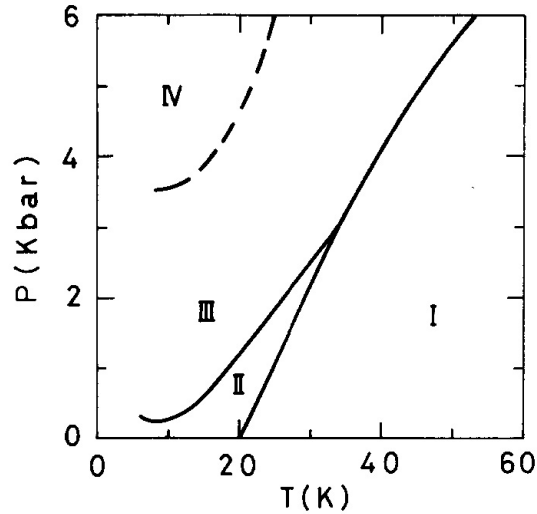
Figure 2.1: The phase diagram of solid methane [42].

results that are important for our calculations. Section 2.3 discusses our neutron scattering model of solid methane. We present the results including neutron cross section and spectral intensity in section 2.4.

2.2 Solid Methane in Phase II

Methane at low temperatures and pressures has two distinct solid phases. The detailed phase diagram is shown in Fig. 2.1. At equilibrium vapor pressure, phase I appears from the triple point temperature (90.6 K) to the transition temperature (20.4 K) into phase II. In phase I, methane has a face-centered cubic (*fcc*) structure with four orientationally disordered molecules per unit cell. This rotational motion

of tetrahedral methane molecules remains slightly retarded even near the melting point of the crystal[43].

The phase change is associated with the onset of orientational order and the introduction of sites with point group symmetry of D_{2d} and O_h in phase II[44]. The center of mass of each methane molecule is located on the site of the face-centered cubic lattice in phase II. Fig. 2.2 shows the partially ordered structure of phase II. It is called an eight-sublattice antiferrotational structure. The unit cell of phase II contains 32 molecules. Three-fourths of the molecules are hindered rotors which librate in the minima of a strong orientational potential of D_{2d} symmetry. The other $1/4$ of the molecules are free rotors.

This structure was predicted by James and Keenan[45] on the basis of electrostatic octopole-octopole interactions. The structure of phase II was experimentally determined by W. Press[46] through neutron diffraction on CD_4. In solid CD_4, phase II is stable in the temperature range 22 K $\leq T \leq$ 27 K. Although the direct structure of CH_4 was not possible to determine because of the high incoherent neutron cross section of protons, Press assumed that the experimentally measured symmetry of CD_4 implies the same orientational structure of CH_4.
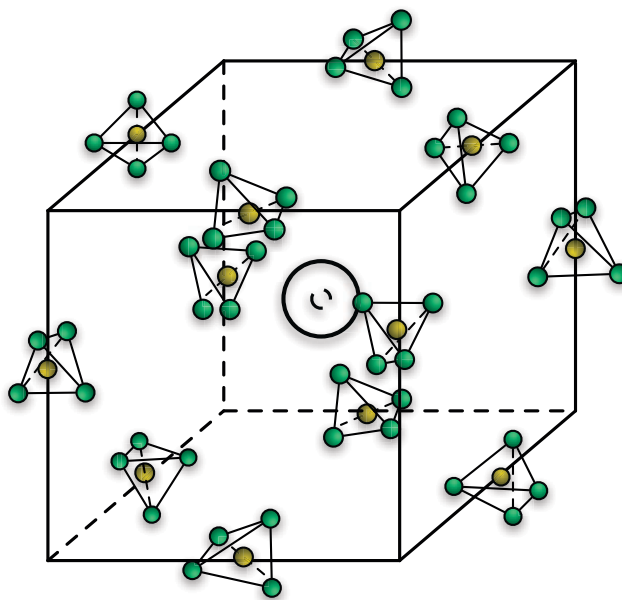
Figure 2.2: The structure of solid methane in phase II[33]. The circle at the center shows sites with almost free rotation of the molecule. The tetrahedra denote the orientationally ordered molecules in the structure.

Rotational Excitation of Free Rotor: O_h symmetry

In phase II, CH_4 is in a partially ordered state with respect to molecular orientations. The eight sublattice structure consists of six ordered sites with point symmetry D_{2d} and two disordered sites with point symmetry O_h. The orientational ordering results from octopole-octopole interactions with neighboring molecules at the lower-symmetry sites. At the sites of higher symmetry, the crystal field is much weaker and therefore the methane molecules on this site are almost free quantum rotors [35].

The Hamiltonian of the Extended James-Keenan (EJK) model for molecule i in a crystal field V_c is

$$H_i = K_i + f_c \sum_{l \geq 4} V_c(\omega_i^E) = K_i + f_c B(\beta_4(\omega_i^E) + \beta_6(\omega_i^E)), \tag{2.1}$$

using the notation of Yamamoto *et al.*[42]. The numerical values of β_4 and β_6 are listed in Table I of Yamamoto *et al.*[42]. K_i is the operator for the rotational kinetic energy. The parameter $f_c = 1.25$ was determined from experiments by fitting the strength of the observed crystalline field [42]. The rotational wave function is given by the standard Wigner functions $\mathfrak{D}_{k,m}^l(\omega)$. The rotational states of a tetrahedral rotor with potential parameters determined for CH_4 are shown in column B of Fig. 2.3.
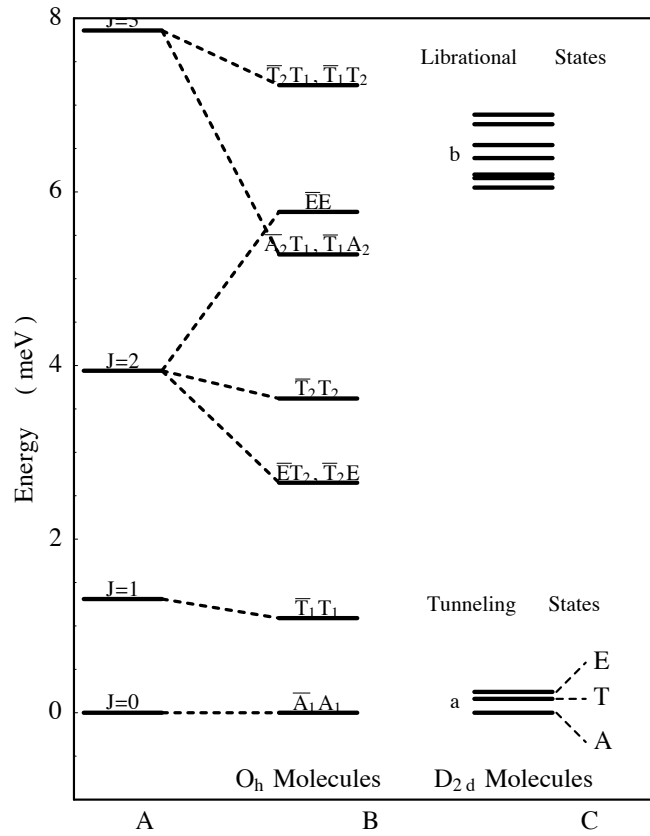
Figure 2.3: The energy levels[47] for the two different sites of CH_4 molecules in phase II: (a) O_h are the orientationally disordered molecules (b) D_{2d} are the orientationally ordered molecules.

The energy levels are classified through the symmetry $\bar{\Gamma}\Gamma$ of the corresponding wave function. The label $\bar{\Gamma}\Gamma$ denotes the 25 irreducible representations of the direct product group $\bar{\mathbf{O}} \times \mathbf{O}$ which describes the symmetry with reference to the crystal-fixed frame (Γ) and with reference to the molecular fixed frame ($\bar{\Gamma}$). The total wave function of a CH_4 molecule is the product of a rotational wave function and a spin wave function. Since protons are spin $1/2$ particles, the total wave function must be anti-symmetric under a permutation of any two protons. Therefore, each state is related to a representation A, T and E corresponding to the total nuclear spin $I = 2$ (ortho), $I = 1$(meta) and $I = 0$(para), respectively. By conservation of angular momentum in s-wave scattering, the state $\bar{E}E$ cannot be reached by neutron interaction from the ground state $\bar{A}A$[35].

A simple description in terms of the energy levels of CH_4 beginning with $J = 0$ (A symmetry, $I = 2$) for the ground state has been given by Ozaki *et at.*[31]. As may be seen in column A and B of Fig. 2.3, the $J = 1$ (T symmetry, $I = 1$) level is lowered from the free rotor value by 25% due to crystal field effects. The $J = 2$ (E symmetry, $I = 0$) level is split by the reduced local crystal field into four energy levels. The energies of the transitions between rotational energy levels are 1.09 meV for the $J = 0 \leftrightarrow J = 1$ transition, 1.56 meV for the $J = 1 \leftrightarrow J = 2$ transition and 2.65 meV for the $J = 0 \leftrightarrow J = 2$ transition.

The Orientational Tunneling in Molecular Field: D_{2d} symmetry

The molecule on the orientationally ordered lattice points of CH_4 not only librates in the minima of the orientational potential, but also tunnels between each of the indistinguishable equilibria in two or three dimensional rotational motions of the CH_4 molecule. The rotational tunneling is accessible from various librational states of the molecule. Since the rotating atoms are indistinguishable[48], this tunneling leads to a splitting between the states. The calculation of eigenstates for the orientational motion using free rotational wave functions was performed in the framework of the EJK model by Yamamoto *et al.*[42]. These procedures required a diagonalization of an infinite dimensional Hamiltonian matrix. Although the procedure converged quickly because of the weak orientational potential, the wave functions of these tunneling levels are only slightly different from those of the completely free rotor.

An alternative approach was developed by Hüller and Kroll using a "pocket state" to treat the rotational and tunneling excitations in molecular crystals[39][40]. A systematic representation is shown in column C of Fig. 2.3. A rotational potential with n minima on two or three dimensional unit sphere was considered. These minima have a symmetric relation to each other. A set of states $|i\rangle$ centered at each minimum, called "pocket states" are taken as the basis set. Applying the operator R_n from the symmetry group T of the CH_4 molecule, one obtains the states $|n\rangle =$

$R_n|i\rangle$. Here R_n denotes one of the 12 symmetry elements of the tetrahedral group T.

Hüller explicitly gave the transformation which diagonalizes the 12 Hamiltonian matrix $\langle n'|H|n\rangle$ of this system. For tetrahedral symmetry, there is just one $120°$ overlapping matrix element $h = h_1 = h_2 = h_3 = h_4$, as well as $180°$ overlapping matrix element $H = H_1 = H_2 = H_3 = H_4$. The h is related with rotations of the tetrahedron about its threefold axes and H is related with rotations of the tetrahedron about its twofold axes. Diagonalization yields states with A, T and E symmetry with the following eigenvalues

$$
\begin{aligned}
E_A &= D + 3H + 8h \quad \text{(singlet)} \\
E_T &= D - H \qquad \text{(three triplets)} \\
E_E &= D + 3H - 4h \quad \text{(doublet)},
\end{aligned}
\tag{2.2}
$$

where $D = \langle n'|H|n\rangle$ is the diagonal element of the Hamiltonian matrix. In such a condition, the tunneling states split into a quintet (A, $T1$, $T2$, $T3$, E) with nine allowed transitions of different energy transfer. In a strong orientational field (in case $H \ll h$), the tunneling associated with twofold axes can be neglected. The site symmetry increases so that the T levels become degenerate and the number of transitions is reduced[35][49].

The tunneling frequency depends on the overlap of the pocket states. From the Pauli principle, each rotational state of symmetry *A,T* and *E* is associated with a definite total spin of the four protons, $I = 2, 1, 0$ respectively. The energy levels of each state are 0, 0.16 and 0.24 meV respectively. The librational state starts at $E_{lib} = 6.5$ meV. Transitions between levels of different symmetry cannot be induced by phonon interaction alone, but are mediated by the weak dipole-dipole interaction among protons. As a consequence, the spin system shows slow thermal relaxation after a sudden change of the lattice temperature[50].

Theoretical and experimental work has been performed on the temperature dependence of D_{2d} energy levels below $T = 4$K. Yamamoto *et al.*[42] predicted the temperature dependence of the tunneling levels based on the EJK model. Their theoretical prediction was made for an equilibrium mixture of spin species. The tunneling level spacings at 0 K are about 10% larger than those at 4 K. Press and Kollmai[51] investigated the temperature dependence of the tunneling states as well as of the $J = 0 \rightarrow J = 1$ rotational transition in ordered rotational system at $T = 4.9$ K. By contrast, the rotational levels of O_h molecules were predicted to be independent of temperature. Press *et al.*[52] measured this level spacing of disordered rotational system of methane at $T = 5$ K and $T = 0.1$ K with inelastic neutron scattering. It showed that $J = 1$ energy level at $T = 0.1$ K remains unchanged at $T = 5$ K. Based on these results, in this paper we assume that the energy levels of

both ordered and disordered molecules are unchanged over the temperature range from $0 \, \mathrm{K} \leq T \leq 20.4 \, \mathrm{K}$.

2.3   Neutron Cross Section Model of Solid Methane

A methane molecule in a crystal shows three different dynamic modes depending on the incident neutron energy E_n. The rigid H_4 tetrahedron rotates about the central carbon atom. The whole molecule oscillates in the crystal lattice. Finally, the protons vibrate around their equilibrium positions within the molecule.

The total neutron scattering cross section is evaluated from the usual expression

$$\frac{d^2\sigma}{d\Omega dE} = b^2 \left(\frac{k_f}{k_i}\right) S(Q,\omega), \tag{2.3}$$

where b denotes the scattering amplitude and k_i and k_f the momentum of the neutron before and after the scattering. By integrating $S(Q,\omega)$ over the solid angle Ω and the neutron energy transfer ω, the total cross section σ_{tot} is obtained.

The scattering function $S(Q,\omega)$ depends on the complete set of modes of the methane molecule; intra-molecular rotations of the tetrahydrogen about the center, inter-molecular transitions of the center of mass and intra-molecular vibrations. If these modes are independent, then $S(Q,\omega)$ may be written as a convolution of the

dynamic structure factors for the different dynamic modes of the motion:

$$S(Q,\omega) = S_{rot}(Q,\omega) \otimes S_{trans}(Q,\omega) \otimes S_{vib}(Q,\omega). \tag{2.4}$$

Each dynamic mode in Eq. 2.4 is characterized by a definite excitation spectrum $\rho_i(\omega)$ of the quanta of each mode, called roton, phonon and vibron. To determine the excitation energies of the solid methane which can occur in neutron scattering, we must know the excitation spectra of all of the modes and the statistics obeyed by the quanta belonging to different modes. In the first approximation, the total excitation energy of the crystal can be represented as

$$E_{crystal} = \sum_i \int dE E f_i(E) \rho_i(\omega), \tag{2.5}$$

where $f_i(E)$ is a distribution function. At this stage, we assume that the coupling among the different dynamic modes can be ignored. This means that the total excitation spectrum is the sum of the contributions from rotations, translation and vibration. Denoting each contribution by $\rho_r(\omega)$, $\rho_t(\omega)$ and $\rho_v(\omega)$ respectively, we have

$$\rho_{crystal}(\omega) = \rho_r(\omega) + \rho_t(\omega) + \rho_v(\omega). \tag{2.6}$$

This is still a good approximation to the scattering function $S(Q,\omega)$ if each dynamic

mode is dominant in different incident neutron energy regimes E_n.

For $E_n \leq 6.5$ meV, the protons in solid CH_4 behave like bound particles. Only the lowest few orientational energy levels are thermally populated in the solid at low temperatures, while the molecules are in their translational and vibrational ground states [33]. Therefore, the scattering function $S(Q, \omega)$ in this energy region can be approximated as

$$S(Q, \omega) \approx S_{rot}(Q, \omega). \tag{2.7}$$

For 6.5 meV $\leq E_n \leq 165$ meV, the H_4 tetrahedron reaches its rotational "free" state and the librational degrees of freedom are active. The cross section for excitaiton of rotational degrees of freedom significantly decreases, and the cross section for molecular oscillations in the crystal lattice appears,

$$S(Q, \omega) \approx S_{rot}(Q, \omega) + S_{trans}(Q, \omega). \tag{2.8}$$

Finally, when neutrons reach the energy $E_n \approx 165$ meV, the protons start to behave like individual free particles. The neutron scattering is then not dominated by multiple inelastic scattering, but also experiences contributions from vibrations of the tetrahedrons,

$$S(Q, \omega) \approx S_{trans}(Q, \omega) + S_{vib}(Q, \omega). \tag{2.9}$$

Then the total scattering function $S(Q, \omega)$ of solid methane in the incident neutron energy range from 0.1 meV to 1 eV can be approximated as

$$S(Q, \omega) \approx S_{rot}(Q, \omega) + S_{trans}(Q, \omega) + S_{vib}(Q, \omega). \tag{2.10}$$

Rotational Excitation

The rotational excitations of solid methane in phase II were taken from Ozaki's work [31][32] which has a more complete description of rotational excitations of methane. The double differential cross section for rotational motion can be divided into two parts:

$$\frac{d^2\sigma}{d\Omega dE} = \left(\frac{d^2\sigma}{d\Omega dE} \right)_{spin-ind} + \left(\frac{d^2\sigma}{d\Omega dE} \right)_{spin-dep}. \tag{2.11}$$

Each term of Eq. 2.11 represents coherent and incoherent scattering in the rotational system as

$$
\left(\frac{d^2\sigma}{d\Omega dE}\right)_{spin-ind} = b_{coh}^2 \frac{k_f}{k_i} p_i(T) g_i g_f \sum_{l=0}^{\infty} (2l+1) j_l^2(\mathbf{kr})
$$

$$
\times F_l^{i,j} \delta(\hbar\omega + E_f - E_i) \times \mathrm{e}^{-\gamma_{rot}Q^2},
$$

$$
\left(\frac{d^2\sigma}{d\Omega dE}\right)_{spin-dep} = b_{inc}^2 \frac{k_f}{k_i} p_i(T) g_i g_f \sum_{l=0}^{\infty} (2l+1) j_l^2(\mathbf{kr})
$$

$$
\times G_l^{i,j} \delta(\hbar\omega + E_f - E_i) \times \mathrm{e}^{-\gamma_{rot}Q^2}, \tag{2.12}
$$

in which the coherent scattering corresponds to spin-independent part and incoherent part to spin-dependent one. The $p_i(T)$ are the occupation probabilities for the initial states in thermal equilibrium

$$
p_i(T) = \frac{\exp(-E_i/k_B T)}{\displaystyle\sum_i \exp(-E_i/k_B T)}.
$$

From Eq. 2.12, the scattering functions for molecular rotations in each rotational state are

$$S_{rot}^{coh}(Q,\omega)_{i,f} = p_i(T)g_ig_f \sum_{l=0}^{\infty}(2l+1)j_l^2(\mathbf{kr})$$

$$\times F_l^{i,j}\delta(\hbar\omega + E_f - E_i) \times e^{-\gamma_{rot}Q^2},$$

$$S_{rot}^{inc}(Q,\omega)_{i,f} = p_i(T)g_ig_f \sum_{l=0}^{\infty}(2l+1)j_l^2(\mathbf{kr})$$

$$\times G_l^{i,j}\delta(\hbar\omega + E_f - E_i) \times e^{-\gamma_{rot}Q^2}. \tag{2.13}$$

Here g_i and g_f denote the degeneracy of the initial and final states and $F_l^{i,j}$ and $G_l^{i,j}$ are transition integrals between the initial and final states which were calculated in Ozaki's works [31][32]. The $j_l(\mathbf{kr})$ are the spherical Bessel functions. The $\mathbf{r}$ stands for C−H distance within a methane molecule ($\mathbf{r} = 1.093$ Å) and $\gamma_{rot} = 2.15 \times 10^{-4}$ nm^2 represents an effective Debye-Waller factor, whose value we take from previous work by Grieger *et al.* [33].

After summing over all initial and final states, the complete expression for the scattering function for molecular rotations in solid methane including coherent and incoherent parts is

$$S_{rot}(Q,\omega) = \sum_{i,f}(S_{rot}^{coh}(Q,\omega)_{i,f} + S_{rot}^{inc}(Q,\omega)_{i,f}). \tag{2.14}$$

Intermolecular Vibrations : Multi-phonon Excitations

The incoherent scattering from a Bravais lattice due to one-phonon processes is

$$
\begin{aligned}
\frac{d^2\sigma}{d\Omega dE} =& b_{inc}^2 \sum_{q,s} \frac{k_f}{k_i} \delta(\hbar\omega \pm \hbar f) \left| \overline{\mathbf{Q}} \cdot \overline{\mathbf{V}} \right|^2 \\
& \times \frac{\hbar(n + \frac{1}{2} \pm \frac{1}{2})}{2Mf} \times \mathrm{e}^{-\gamma_{tran}Q^2},
\end{aligned}
\tag{2.15}
$$

where $\mathbf{Q}$ denotes momentum transfer and $\mathbf{V}$ is the polarization vector for each phonon mode[10]. The model parameter is $\gamma_{tran} = 2.08 \times 10^{-4}$ nm^2 which was found from fitting the experimental neutron scattering cross section data across 10 meV over all temperatures.

If $\left| \overline{\mathbf{Q}} \cdot \overline{\mathbf{V}} \right|^2$ in Eq. 2.15 is replaced by $\left| \overline{\mathbf{Q} \cdot \mathbf{V}} \right|^2$ where the bar denotes that an average over a constant frequency surface has been taken, the incoherent cross-section may be written as

$$
\begin{aligned}
\frac{d^2\sigma}{d\Omega dE} =& b_{inc}^2 \int_0^\infty df\, z(f) \frac{k_f}{k_i} \left| \overline{\mathbf{Q} \cdot \mathbf{V}} \right|^2 \\
& \times \frac{\hbar(n + \frac{1}{2} \pm \frac{1}{2})}{2Mf} \times \mathrm{e}^{-\gamma_{tran}Q^2} \delta(\hbar\omega \mp \hbar f),
\end{aligned}
\tag{2.16}
$$

where $z(f)$ is the frequency of the phonon mode and cubic symmetry has been assumed.

Since phonons of different wave vectors are independent in the incoherent approximation, the generalization of one phonon scattering to the multi-phonon case in this approximation is straightforward. We considered different phonon modes which change their population by ± 1 and thus the n-phonon cross section contains a product of n-factors of type $\left| \overline{\mathbf{Q} \cdot \mathbf{V}} \right|^2 |\phi|^2$. It can be shown that the cross-section for neutron scattering is

$$
\frac{d^2\sigma}{d\Omega dE} = b_{inc}^2 N \frac{k_f}{k_i} \frac{1}{n!} \prod_{i=1}^{n} \left(\int_{-\infty}^{\infty} df \frac{z(f_i)}{f_i} \frac{\hbar^2 Q^2 / 2M}{e^{\frac{\hbar f_i}{k_i T}} - 1} \right)
$$

$$
\times\, e^{-\gamma_{tran} Q^2} \delta\left(\hbar\omega + \sum_i \hbar f_i \right). \tag{2.17}
$$

Using the Debye approximation, it is possible to carry out the necessary integrations to obtain the cross-section σ_n^{inc}. The total inelastic incoherent cross-section is then given by

$$
\sigma_{inelastic}^{inc} = \sum_{n=1}^{\infty} \sigma_n^{inc}. \tag{2.18}
$$

The scattering function $S_{trans}(Q,\omega)$ is now written as

$$
\begin{aligned}
S_{trans}(Q,\omega) &= \sum_{n=1}^{\infty} S_{trans}^{n}(Q,\omega) \\
&= \sum_{n=1}^{\infty} \frac{1}{n!} \prod_{i=1}^{n} \left(\int_{-\infty}^{\infty} df \frac{z(f_i)}{f_i} \frac{\hbar^2 Q^2/2M}{e^{\frac{\hbar f_i}{k_i T}} - 1} \right) \\
&\quad \times e^{-\gamma_{tran}Q^2} \times \delta(\hbar\omega + \sum_{i} \hbar f_i).
\end{aligned}
\tag{2.19}
$$

Intramolecular Vibrations

From the simple harmonic oscillator model[53], the scattering function for intramolecular vibration is

$$
\begin{aligned}
S_{vib}(Q,\omega) = &\frac{1}{2\pi\hbar} \int_{-\infty}^{\infty} dt \, \exp(-i\omega t) \\
&\times \langle \exp(-i\mathbf{Q} \cdot \hat{\mathbf{r}}) \exp\{i\mathbf{Q} \cdot \hat{\mathbf{r}}(t)\} \rangle .
\end{aligned}
\tag{2.20}
$$

To calculate the response function for our model, we need to calculate the correlation function,

$$\langle \exp(-i\mathbf{Q} \cdot \hat{\mathbf{r}}) \exp\{i\mathbf{Q} \cdot \hat{\mathbf{r}}(t)\}\rangle$$

$$= \prod_{\alpha=x,y,z} \langle \exp(-i\mathbf{Q}_\alpha \cdot \hat{\mathbf{r}}_\alpha) \exp\{i\mathbf{Q}_\alpha \cdot \hat{\mathbf{r}}_\alpha(t)\}\rangle$$

$$= \exp\left\{-\langle(\mathbf{Q} \cdot \hat{\mathbf{r}})\rangle + \langle(\mathbf{Q} \cdot \hat{\mathbf{r}})\{\mathbf{Q} \cdot \hat{\mathbf{r}}(t)\}\rangle\right\}. \tag{2.21}$$

For an isotropic harmonic oscillator,

$$\langle(\mathbf{Q} \cdot \hat{\mathbf{r}})\{\mathbf{Q} \cdot \hat{\mathbf{r}}(t)\}\rangle = \frac{\hbar Q^2 \cosh\left\{\omega_0\left(it + \frac{1}{2}\hbar\beta\right)\right\}}{2M\omega_0 \sinh\left(\frac{1}{2}\hbar\omega_0\beta\right)}. \tag{2.22}$$

On setting $t = 0$, we find on the right side of the Eq. 2.22,

$$\langle(\mathbf{Q} \cdot \hat{\mathbf{r}})^2\rangle = \left(\frac{\hbar Q^2}{2M\omega_0}\right)\coth\left(\frac{1}{2}\hbar\omega_0\beta\right)$$

$$= 2W(Q) = \gamma_{vib}Q^2. \tag{2.23}$$

Using the identity,

$$\exp\left(y\cosh(x)\right) = \sum_{n=-\infty}^{\infty} \exp(nx)I_n(y) \tag{2.24}$$

where n is an integer and $I_n(y) = I_n(-y)$ is a Bessel function of the first kind. Using $x = \omega_0(it + \frac{1}{2}\hbar\beta)$ and $y = \frac{\hbar Q^2}{2M\omega_0\sinh\left(\frac{1}{2}\hbar\omega\beta\right)}$, the correlation function becomes

$$\exp\langle(\mathbf{Q}\cdot\hat{\mathbf{r}})\{\mathbf{Q}\cdot\hat{\mathbf{r}}(t)\}\rangle = \sum_{n=-\infty}^{\infty} I_n(y)\exp\left\{n\omega_0(it + \frac{1}{2}\hbar\beta)\right\}. \qquad (2.25)$$

We obtain the scattering function of the vibrational mode as

$$S_{vib}(Q,\omega) = \exp(-\gamma_{vib}Q^2 + \frac{1}{2}\hbar\omega\beta) \sum_{n=-\infty}^{\infty} I_n(y)\delta(\hbar\omega - n\hbar\omega_0) \qquad (2.26)$$

where ω_0 is normal vibration frequency. A methane molecule has four normal vibrations with characteristic energies of $\hbar\omega_0 = 168$, 172, 376, and 391 meV [54]. The model parameter, $\gamma_{vib} = 0.31 \times 10^{-4}$ nm^2, was calculated from Eq. 2.23 using the first two characteristic energies $\hbar\omega_0 = 168$, 172 meV.

2.4   Results and Discussion

Scattering Function $S(Q,\omega)$ of Solid Methane

The total scattering function of solid methane is the convolution of scattering functions of the three different modes. In our approximate model, we treat this total scattering function as the linear combination of each scattering function in Eq.
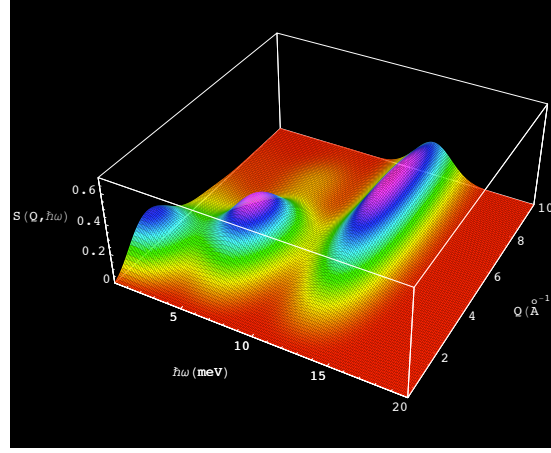
(a) 20 K
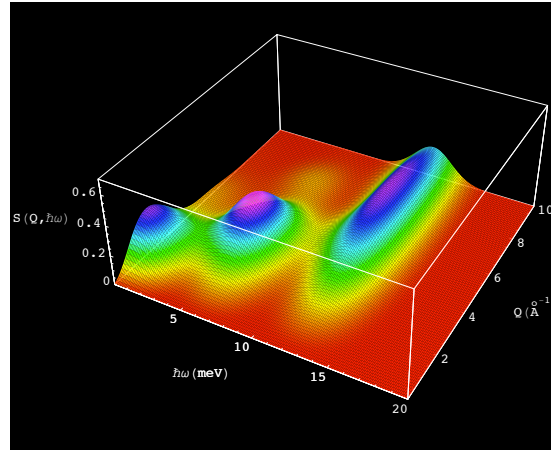
(b) 4 K
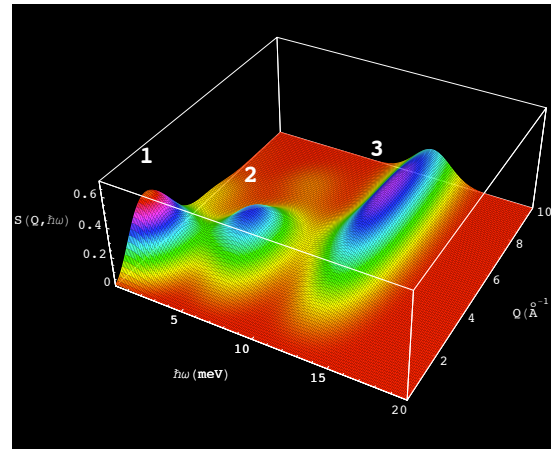
(c) 0 K

Figure 2.4: 3D plots of the dynamic structure factor $S(Q, \omega)$ for solid methane in phase II at 20 K, 4 K and 0 K. There are three peaks labeled as 1, 2 and 3. Peak 1 corresponds to orientational tunnelings in D_{2d} symmetry and low energy excitations in O_h symmetry. Peak 2 comes from rotational librations in D_{2d} and high energy excitations in O_h. Peak 3 represents the multi-phonon scattering.

2.7, Eq. 2.8, and Eq. 2.9 depending on incident neutron energy as mentioned in Eq. 2.10. This is an approximation to calculate the total scattering function in which each different scattering mode dominates in different neutron energy regimes. We show the 3D plots of $S(Q, \omega)$ at 20 K and 4 K as a function of momentum transfer ($Q = 0 \sim 10\text{Å}^{-1}$) and energy transfer ($\hbar\omega = 0 \sim 20$ meV) in Fig. 2.4(a) and Fig. 2.4(b). Based on our assumption in Section 2.2, the scattering function of solid methane at $T = 0$ K is also presented in Fig. 2.4(c).

In these figures, the two peaks with lower energy transfer ($0 \leq \hbar\omega \leq 10$ meV), labled as 1 and 2, represent energy and momentum transfers from the orientational modes. The long hump around $\hbar\omega \approx 12$ meV comes from multi-phonon excitations. For lower temperatures, the overall probability for energy transfer from the rotational mode is increased while the energy transfer from multi-phonon scattering is suppressed as the temperature drops. The integrated intensity in the three peaks for different temperatures is listed in Table.2.1

The main difference of $S(Q, \omega)$ at 0 K from 20 K and 4 K is the scattering probability in the low (Q, ω) region labeled as peak 1. It increases by 40% at 0 K from 4 K and 20 K. On the other hand, the intensity of peak 2 reduces by 20% and peak 3 changes less. The reason is that, as the temperature lowered below 4 K, the spin conversion begins to occur among the tunneling levels of different symmetry and the ground state with A $(I = 2, J = 0)$ symmetry become increasingly populated.

T(K)	Peak 1	Peak 2	Peak 3
20K	13	32	55
4K	14	32	54
0K	18	28	54

Table 2.1: The relative intensity (%) of the three peak regions for $S(Q, \omega)$ of phase II solid methane at 20K, 4K and 0K. The identification of each peak is shown in Fig. 2.4.

Consequently, this makes the $A \rightarrow T$ transition more intense[42].

Generalized Frequency Spectrum

The dynamics of a given system can be described by establishing the corresponding space-time correlation functions $G(r, \tau)$. If the system includes a large number of particles, one can use the statistical independence of widely separated particles and assume that if the particle B is far distant from particle A, one can forget about the existence of the neighboring particles.

For small r and τ, it is expected, on general grounds, that the important part of the scattering law for neutron thermalization is the self-term $G_s(r, \tau)$ defined as the Van-Hove self-correlation function

$$G_s(r, \tau) = \frac{1}{N} \left\langle \sum_n \int_v dr' \delta(r + r_n(0) - r')\delta(r' - r_n(\tau)) \right\rangle, \qquad (2.27)$$

which gives rise to the scattering function

$$S(Q, \omega) = \frac{1}{2\pi} \int e^{i(\mathbf{Q} \cdot \mathbf{r} - \omega \cdot \tau)} G_s(r, \tau) dr d\tau. \tag{2.28}$$

Eq. 2.27 is the velocity-velocity correlation function for the motion of an atom in the medium[55]. The interpretation of this function as a generalized frequency spectrum is as follows: one imagines that the velocity of an atom is measured at certain time t_1. Then its velocity is remeasured at a later time t_2. The product of these two velocity measurements is taken and averaged over all values of the velocity which may be generated by thermal excitation of the system to define the function $P(\omega)$[56].

$$
\begin{aligned}
&\left(\frac{\omega^2 \exp\left(-\frac{\hbar\omega}{2k_B T}\right) S(Q, \omega)}{Q^2} \right)_{Q \to 0} \\
&= \frac{\exp\left(-\frac{\hbar\omega}{2k_B T}\right)}{2\pi} \int_{-\infty}^{\infty} \langle v_Q(0) v_Q(\tau) \rangle \, e^{i\omega\tau} d\tau \\
&= \frac{k_B T}{2M} P(\omega).
\end{aligned}
\tag{2.29}
$$

The function $P(\omega)$ defined in this way is a complex function and its real and
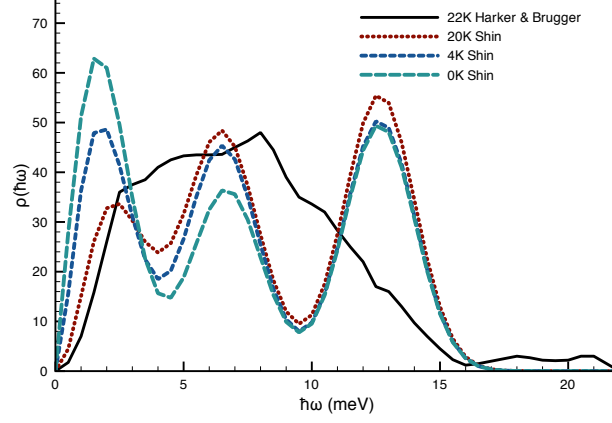
Figure 2.5: The frequency spectrum of solid methane at temperatures of 20 K (dotted line), 4 K (short dashed line) and 0 K (long dashed line) extracted from our model. The Harker & Brugger spectrum at 22 K (solid line) was inferred from an experimental measurement [34].

imaginary parts are related to the $P(\omega)$ as

$$\text{Im}\,\langle v_Q(0)v_Q(\tau)\rangle = \frac{\hbar}{2M}\int_0^\infty \omega\rho(\omega)\sin(\omega\tau)d\omega$$

$$\text{Re}\,\langle v_Q(0)v_Q(\tau)\rangle = \frac{k_BT}{2M}\int_0^\infty \frac{P(\omega)\cos(\omega\tau)}{\cosh(\hbar\omega/2k_BT)}d\omega, \tag{2.30}$$

where $\rho(\omega) = P(\omega)\frac{\sinh(\hbar\omega/2k_BT)}{\hbar\omega/2k_BT}$ is the generalized frequency spectrum, with normalization condition $\int_0^\infty \rho(\omega)d\omega = 1$. For a solid, the function $\rho(\omega)$ is the same as the frequency distribution. In solid methane, the frequency spectrum represents all characteristics of the rotational, translational and vibrational behaviors of a molecule[55]. The total excitation spectrum is an additive as shown in Eq. 2.6.
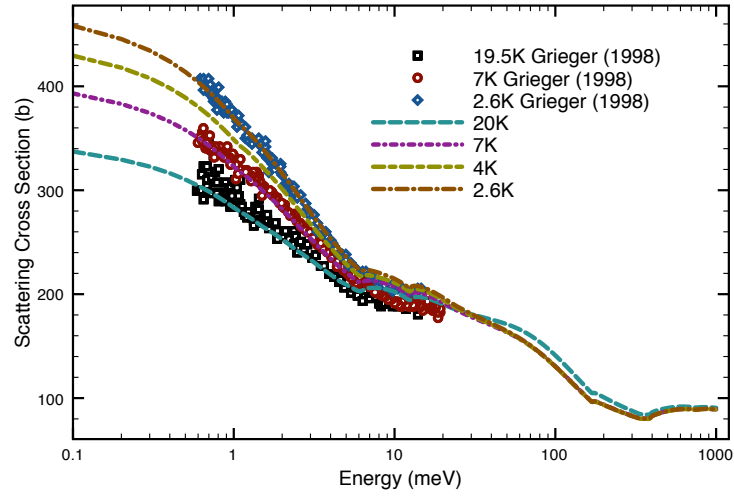
(a) Total Neutron Scattering Cross Section
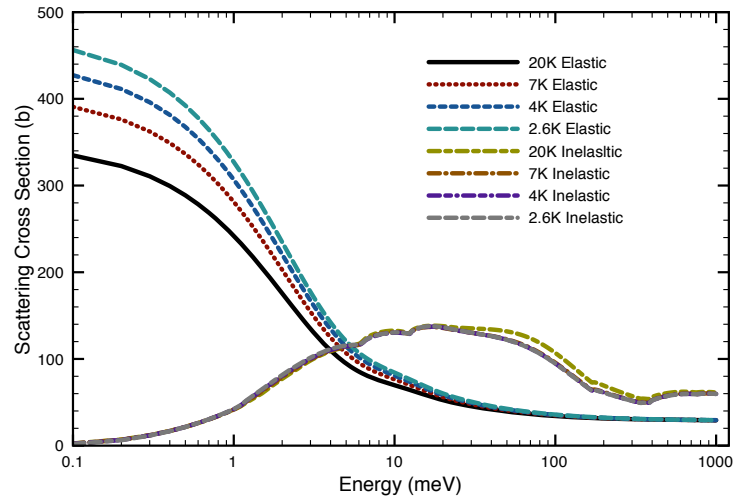
(b) Elastic and Inelastic Scattering Cross Sections

Figure 2.6: (a) The total neutron scattering cross section of solid methane at 20 K (long dashed line), 7 K (dot-short dashed line), 4 K (short-long dashed line) and 2.6 K (dot-long dashed line) calculated from the model, compared to the measurement data from Grieger *et al.*[33]. (b) The separation of elastic and inelastic neutron scattering cross section at each temperature.

Fig. 2.5 shows the frequency spectra of solid methane at three temperatures in phase II, 20 K, 4 K and 0 K, compared with the 22 K Harker & Brugger's frequency spectrum[34]. We plotted these spectra up to $E \approx 22$ meV which means this plot includes only orientational and phonon modes. The black solid line is the Harker & Brugger's frequency spectrum at 22 K which was generated by interpolation from neutron scattering data in 1960 [34]. The red dotted line is the frequency spectrum at 20 K. The blue short-dashed line is at 4 K, and the light blue long dashed line is at 0 K. The frequency spectra are computed from our model. The first peak around 2 meV in the frequency spectrum at 20 K, 4 K and 0 K represents the linear superposition of the energy excitations from ground and the first excited rotational energy states to higher states in O_h molecules and the tunneling among ground state multiplets (three lowest states) in D_{2d} molecules. The second peak comes from the linear superposition of energy excitations to the higher rotational states in O_h molecules and the librational states in D_{2d} molecules. The final peak around 12.9 meV is a multi-phonon mode corresponding to the Debye temperature of solid methane ($T_D = 145$ K)[57]. The multi-phonon scattering and higher excitations in orientational modes are suppressed at low temperature. However, the transition probabilities from ground state in the free rotor state increase, and the tunneling probabilities among ground state multiplets in hindered rotor also become larger.
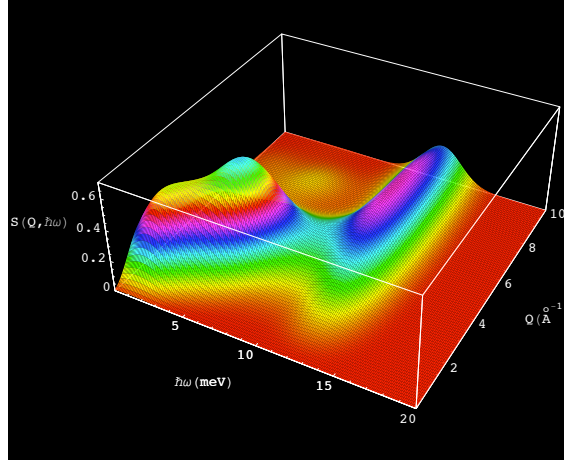
(a) 20K
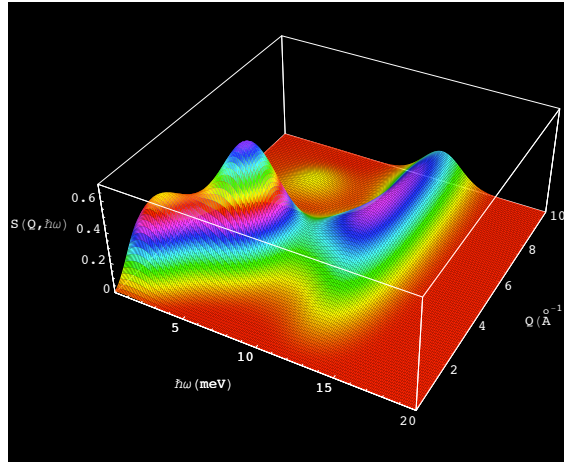
(b) 4K
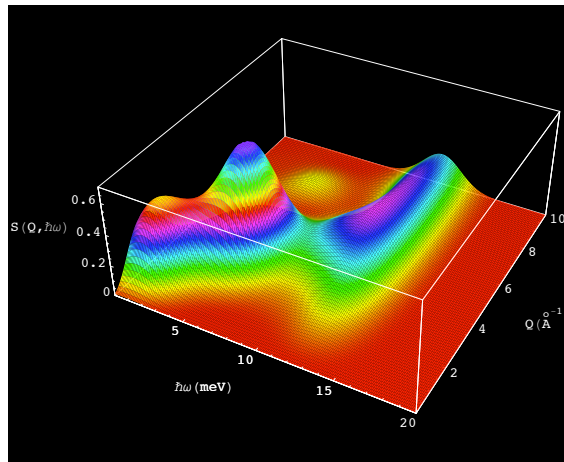
(c) 0K

Figure 2.7: The $S(Q,\omega)$ for free rotation and phonon modes. The origin of the three peaks is descibed in the caption to Fig. 2.4(c).

Total Neutron Scattering Cross Section

We compared our model with the measured total cross section for methane in phase II as a function of neutron energy. In the low neutron energy limit, the total cross section is mainly due to elastic scattering from free and hindered rotors. We calculated the elastic coherent and incoherent scattering of hydrogen from Ozaki [31][32]. For 10 meV $\leq E_n \leq$ 100 meV, σ_{tot} mainly depends on translational excitation. In the higher energy region, the vibrational excitation becomes more important than the rotational and translational scattering.

Fig. 2.6 shows the total neutron scattering cross section at 20 K, 7 K, 4 K and 2.6 K. The theoretical calculations are compared to the measured data at 20 K, 7 K and 2.6 K[19]. Around $E_n = 10$ meV, the total cross section is almost temperature independent. For lower neutron energies, the total cross section depends strongly on temperature. The increase of the cross section from $E_n = 10$ meV down to $E_n = 0.1$ meV is about 150 barns at 20 K and 300 barns at 2.6 K. Independent of temperature, above $E_n = 10$ meV, the cross section decreases from 200 barns to 100 barns around $E_n = 100$ meV and then converges to 80 barns, which is the single free hydrogen scattering cross section, for large E_n.
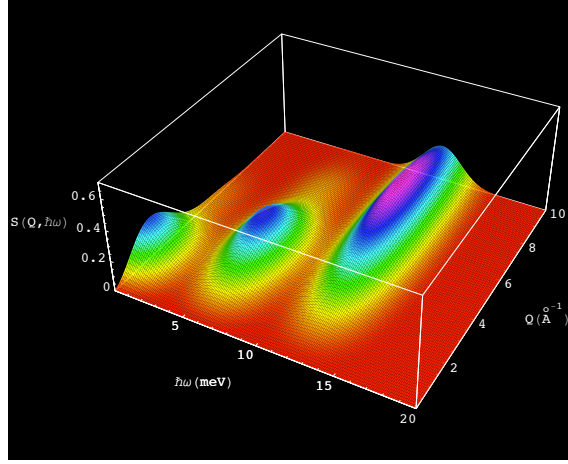
(a) 20K
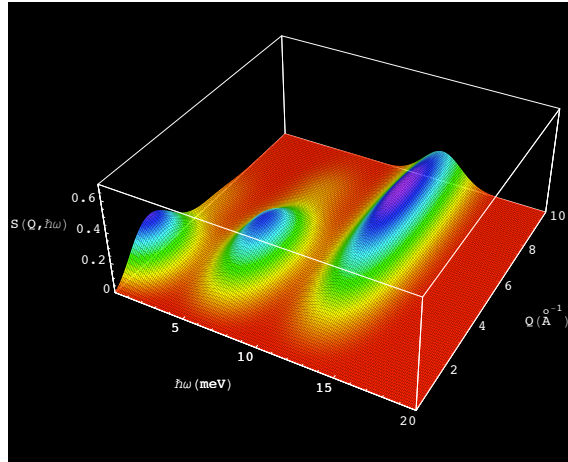
(b) 4K
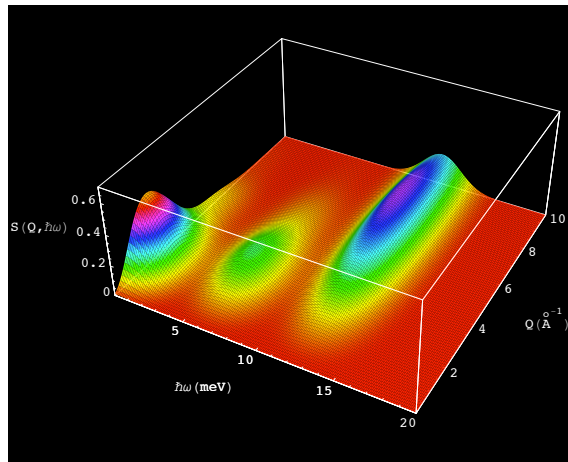
(c) 0K

Figure 2.8: The $S(Q,\omega)$ for hindered rotation and phonon modes. The origin of the three peaks is described in Fig. 2.4(c).

Contribution of the Two Orientational Modes to $S(Q,\omega)$

Our model can be used to understand the relative importance of free and hindered rotations for neutron moderation in solid phase II methane. We assumed that one of the two types of rotational modes in phase II of CH_4 could be turned off in our model so that the rotational degrees of freedom was either a completely free mode or a completely hindered mode, with the multi-phonon scattering and vibrational modes unchanged. Part of the motivation to consider this possibility comes from the fact that it is known that hindered rotation can disappear in certain argon-methane mixtures[58], and it is therefore of interest whether or not the higher inelastic cross section for the free rotor modes possible in such a system justifies its investigation as a possible moderator medium.

Fig. 2.7, 2.8 show the scattering functions at 20 K, 4 K and 0 K for free rotations and tunnelings/librations respectively. From these plots of $S(Q,\omega)$, one can see immediately the significantly greater spectral weight present at low energy transfers in the free rotor spectrum (Fig. 2.7, compared to the hindered rotor/tunneling spectrum in Fig. 2.8). At the same time, the hindered rotation mode produces two separate contributions to the scattering function corresponding to the orientational tunneling at low energies and the librations in the high energy region.

These features are also present in the frequency spectrum plot in Fig. 2.9. The
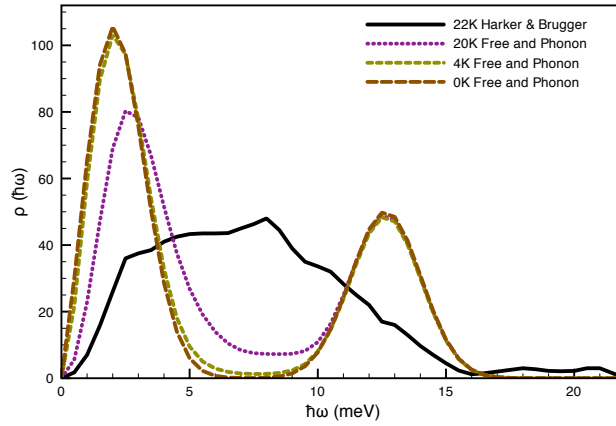
(a) Free rotation and Phonon
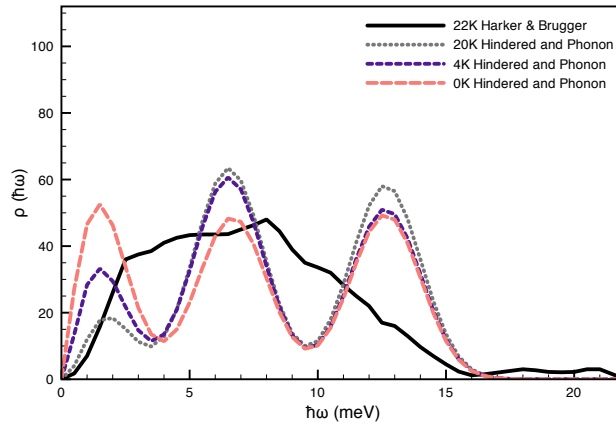
(b) Hindered rotation and Phonon

Figure 2.9: The frequency spectra of solid methane in free rotation and hindered rotation at 20 K (dotted line), 4 K (short-dashed line) and 0 K (long-dashed line). The Harker & Brugger spectrum was measured at 22 K.

spectral weight in the free rotation mode is roughly twice that in the hindered rotor

mode in the low Q limit. The scattering intensity from librations of the hindered

rotors is also low. This higher probability for inelastic scattering from the free ro-

tors is primarily responsible for the larger neutron inelastic scattering cross section

at low temperatures in Fig. 2.10. We also note from Fig. 2.7 and 2.8 that the scatter-

ing probability for the free rotation and tunneling modes increases with decreasing

temperature while that of the librations falls considerably from 20 K to 0 K. There-

fore, it is clear from our studies that the small number of free rotors in phase II

of solid methane are more important to the cold-neutron moderation properties of

methane below 20K than are the librations and tunneling modes contributed by

the hindered rotor sites.
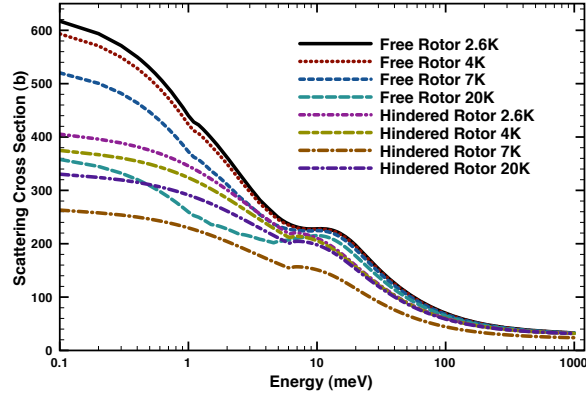
(a) Total Neutron Scattering Cross Section
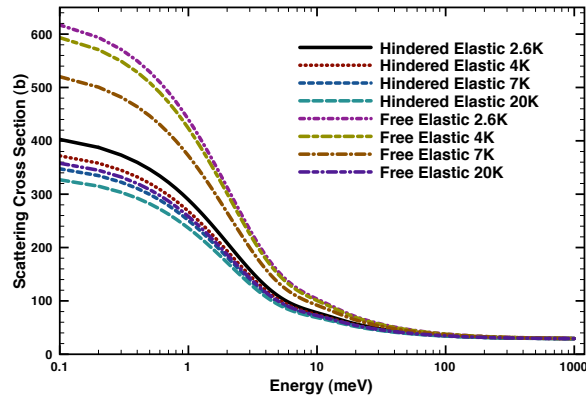
(b) Elastic Neutron Scattering Cross Section
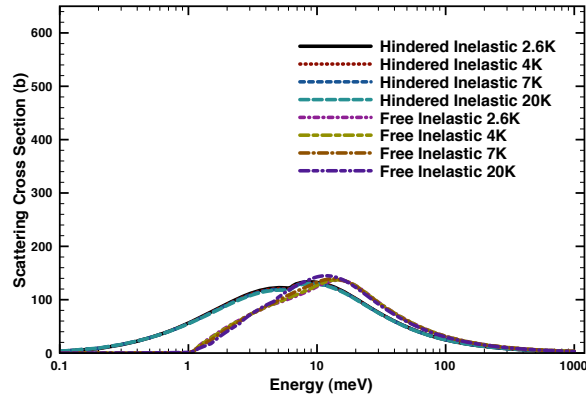
(c) Inelastic Neutron Scattering Cross Section

Figure 2.10: (a) The total neutron scattering cross section from the free rotation mode and the hindered rotation mode in solid methane with multi-phonon mode at 20 K, 7K, 4 K and 2.6K. (b) Elastic neutron scattering cross section at each temperature. (c) Inelastic neutron scattering cross section at each temperature.

3

Measurements of the Neutron

Brightness at LENS

Measurements of the neutron brightness from a solid methane moderator were performed at the Low Energy Neutron Source (LENS) at the Indiana University Cyclotron Facility (IUCF) to characterize the source and to test our new neutron scattering model of phase II solid methane[59]. A time-of-flight method was used to measure the neutron energy spectrum from the moderator in the energy range of 0.1 meV $\sim$ 1 eV. Neutrons were counted with a high efficiency ^{3}He detector. The solid methane in the moderator occupied phase II and the energy spectra were measured at 20 K and 4 K. We tested our newly-developed scattering kernels for phase II solid methane by calculating the neutron brightness expected from the

methane moderator at the LENS neutron source using MCNP (Monte Carlo N-particle Transport Code). Within the accuracy of our approximate approach, our model correctly predicts the neutron brightness at both temperatures.

3.1 Introduction

The Low Energy Neutron Source (LENS) at the Indiana University Cyclotron Facility (IUCF) is a university based pulsed cold neutron source designed for education, research and neutron instrument development. LENS produces neutrons from low energy (p,xn) reactions in Be target[60]. LENS possesses a cold neutron moderator to convert the MeV neutrons from the Be target to slow neutrons with an energy spectrum and pulse widths suitable for neutron scattering experiments in condensed matter[23]. Elastic scattering from hydrogen atoms at rest in the reflector reduces neutrons from MeV to eV energies[61]. The moderator is primarily responsible for lowering the neutron energy from ∼eV to the energy range of 10 meV∼0.1 meV of primary interest for neutron scattering.

Solid methane is the brightest known moderating medium for pulsed cold neutron sources. This is because of its high hydrogen density and the presence of free rotor modes in the solid at low temperatures. The free rotor excitation offers a mode of energy loss to the neutrons with relatively high neutron cross section not

present in most other cold hydrogenous materials. Unfortunately, its use at high power spallation neutron sources is constrained by engineering difficulties associated with the radiation damage and hydrogen production in solid CH_4 in the intense radiation field near the spallation target [62][63]. The radiation damage at lower power pulsed cold neutron sources such as LENS can be low enough that one can operate the moderator at low temperatures for extended periods of time and at temperatures that are lower than practical at higher-power sources.

Most neutron source facilities which use solid methane as a moderator choose not to operate the moderator below 20 K. For temperatures below 20 K, solid methane enters a phase (called phase II) in which only 1/4 of the rotational modes remain free while the remaining 3/4 of the modes undergo librations and tunneling motions. Since phase I possesses free rotor modes for all sites whereas 3/4 of these free modes are frozen in phase II, it is not obvious that the colder spectrum that one might be able to achieve by operation of the moderator at lower temperatures can be realized in practice due to the loss in free rotor modes. It was observed that the effective temperature of the neutron spectrum, which is typically about a factor of two larger than the physical moderator temperature for most cold neutron moderators, showed strong deviations from the physical temperature of the methane in phase II[64] (see also Fig. 1.2). Furthermore, at high-power neutron sources it is necessary at some point to warm and refreeze the moderator to

release radiation damage energy stored in the lattice in a controlled way before a spontaneous recombination occurs which can produce high transient pressures and burst the moderator vessel [65]. The added inconvenience of repeatedly cycling the moderator through the solid-solid phase transition at 20K between phases I and II in the course of releasing the stored energy from radiation damage, combined with the belief that only small changes in the neutron spectrum are to be expected from operation in phase II, accounts for the 20 K operating temperature chosen by most sources.

However, the LENS neutron source operates in a qualitatively different regime. Since it is based not on spallation nor on fission, but rather uses (p,xn) reactions in a Be target and because the time-averaged neutron production is somewhat lower than typical reactor and spallation sources, it is practical to operate the moderator at much lower temperatures and with greatly reduced radiation damage effects compared to other sources. This possibility allows for the operation of a methane moderator at low temperatures well into the phase II regime.

Since no present cold neutron moderators using solid methane operate in phase II, existing neutron scattering kernels do not consider the modification of the neutron scattering dynamics which should occur in solid methane as a result of this phase transition. This circumstance motivated us to construct a model which describes the physics of all the scattering processes in phase II. The model can be

used as a scattering kernel to calculate the LENS moderator brightness and to estimate the moderator brightness in different conditions. We have developed an approximate model of $S(Q, \omega)$ for solid methane in phase II which is consistent with the known spectroscopy of the low energy modes and the measured neutron total cross section[59]. This model was presented in Chapter 2.

In this chapter, we describe our measurement method, present the experimental results for the moderator brightness measurements from the LENS solid CH_4 moderator in phase II at temperatures of 4 K and 20 K, and compare the measurements with MCNP simulation using our newly-developed scattering kernel. The remainder of this chapter is organized as follows. Section 3.2 reviews the physics of spin conversion in solid methane in phase II which influences our procedure for filling and cooling the moderator. Section 3.3 describes the experimental details of the neutron spectrum and brightness measurements at temperatures of 4 K and 20 K. Section 3.4 describes the theoretical calculations and shows the comparison to experiment. Section 3.5 applies this model to investigate the optimum moderator thickness for the solid methane moderator for the LENS target/moderator/reflector (TMR).

3.2   Solid Methane in Phase II: Spin Conversion

The CH_4 molecules in solid methane may be viewed as quantum mechanical spherical rotors. At temperatures below $\sim$20 K (phase II), the methane in this phase consists of two sublattices. One fourth of the molecules rotate almost freely. The lowest energy levels are at 0, 1.09 and 2.56 meV. The remaining 3/4 of the molecules librate in the deep minima of a strong orientational potential and form a threefold multiplet with levels of 0, 0.16 and 0.24 meV associated with tunneling motion between orientational minima. The librational state energies are present at 6.5 meV and above. As a consequence of the Pauli principle as applied to the 4 identical protons in the CH_4 molecule, each rotational state of symmetry *A*,*T* and *E* are associated with a definite total spin of the four protons, $I = 2, 1, 0$ respectively. Transitions between levels of different symmetry, which require a change in the spin state of the protons, cannot be induced by phonon interactions alone but must be mediated by spin-dependent interactions such as the weak dipole-dipole interaction among protons. As a consequence, the spin system shows very slow relaxation to thermal equilibrium after a sudden change of the lattice temperature[50].

Fig. 3.1 and 3.2 show the relative populations of the CH_4 molecules in the free rotation and hindered rotation groups. These spin populations are calculated assuming a Boltzmann distribution. As the temperature is lowered, the ratios
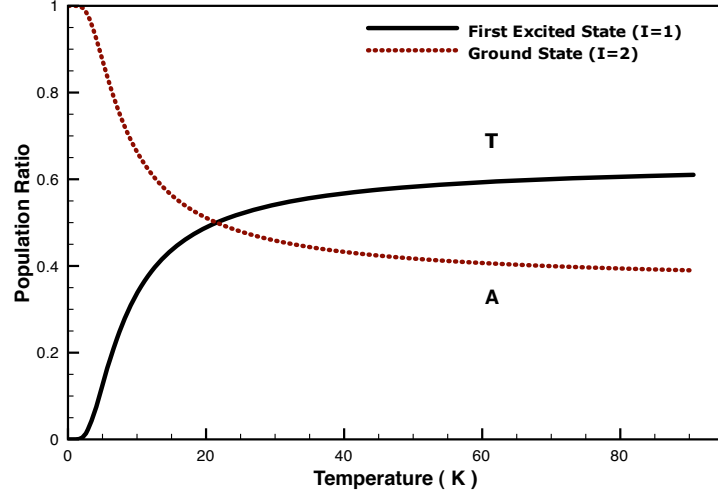
Figure 3.1: The spin population of the free rotation mode

change little from their room temperature values even at the melting point of solid methane ($\sim$90.6 K). The approximation by a two energy state system in free rotation and a three energy state system in hindered rotation is justified at low temperature due to the weak population of higher excited states[66]. The spin distribution function is

$$P_i = g_i \frac{\exp(-E_i/k_B T)}{\displaystyle\sum_i \exp(-E_i/k_B T)} \tag{3.1}$$

where g_i is occupation number of each state.

It has been noticed in several experiments that methane shows only slow relaxation of the spin system even after the change of the lattice temperature. This phenomenon is well understood. The theory of nuclear spin conversion was first
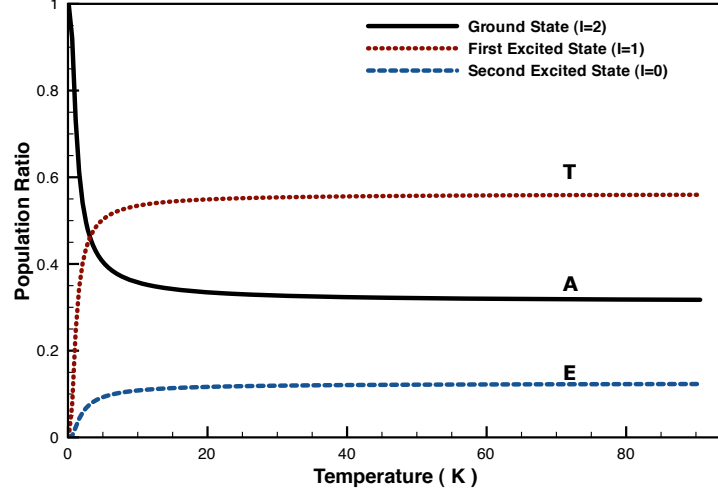
Figure 3.2: The spin population of the hindered rotation mode.

developed for the ortho-para transition of hydrogen and later was extended to solid methane by Nijman & Berlinsky[29]. The importance of the spin-spin interaction had already been shown by Curl *et at.*[67]. The effect of paramagnetic O_2 impurities had been discussed by Kim *et at.*[68].

Nijman & Berlinsky have explained the physics behind the conversion process at a microscopic level. Rates of the conversion from $T \rightarrow A$ symmetric states are evaluated using the Fermi golden rule,

$$\alpha = \frac{1}{\tau} = \frac{2\pi}{\hbar} \sum_{i,f} P_i \mid \langle \Psi_f \mid H^{tr} \mid \Psi_i \rangle \mid^2 \delta(E_i - E_f). \qquad (3.2)$$

The perturbation operator H^{tr} couples different initial and final states $\mid \Psi_i \rangle$ and

$\mid \Psi_f\rangle$. E denotes the energy of the states and P_i the relative occupation of the initial state. There have to be at least two different kinds of interactions to induce a conversion process from one spin species to another. For energy conservation, the coupling to phonons has to be considered. Additionally spin states have to be changed. This requires the presence of magnetic field gradients, i.e. unpaired electrons (e.g. O_2 impurities) or dipole-dipole interactions of protons[50].

The calculation of the total neutron scattering cross section of rotating molecules had shown that

$$\sigma_{tot} \propto \langle I(I+1)\rangle \text{ with} \langle ..\rangle : \text{thermal average} \tag{3.3}$$

is a good approximation for long wavelength neutrons[50]. Since each rotational state is related to a distinct total nuclear spin I, σ_{tot} is proportional to their occupation number g_i in Eq. 3.1. σ_{tot} increases with decreasing temperature because I is higher for the lowest spin levels. The higher temperature limit is determined purely by the number of protons. In the case of methane, it may include the scattering from free and ordered molecules,

$$\sigma_{tot} = \frac{1}{4}\sigma_{free} + \frac{3}{4}\sigma_{hindered}. \tag{3.4}$$

Ozaki *et at.*[31] have calculated the absolute value of the total neutron scattering

cross section for methane in this phase.

Both the liquid-solid and solid-solid phase transitions, which can lead to nonuniformities in the solid methane density, and the sensitivity of the neutron scattering in methane to the spin state of the protons can cause difficulties in accurately predicting the neutron energy spectrum from a practical moderator. To mitigate these possible problems, we added a small concentration of O_2 paramagnetic impurity to boost the nuclear spin conversion rate, and we cooled the moderator slowly in an attempt to avoid cracks and holes in the moderator. Cracks and holes in the moderator may appear during the thermal contraction of the moderator material and will change the macroscopic neutron cross section. The relative populations of spin species of both the free rotor and hindered rotor systems affect the total scattering cross section σ_{tot}. The conversion rate of two rotational systems are different. For temperature above $\sim$4 K, the occupation number of the hindered modes are always near their high temperature limit and consequently the conversion behavior is dominated by the free rotation mode[50].

3.3   The Neutron Spectrum Measurement

The Configuration for the Measurement

The LENS neutron source had three neutron beam lines oriented at $-20°$, $0°$ and $20°$ relative to the normal surface of the moderator when these measurements were performed. The neutron spectrum measurements were performed on the beam line at $-20°$. Fig. 3.3 shows the layout for the neutron spectrum measurement.
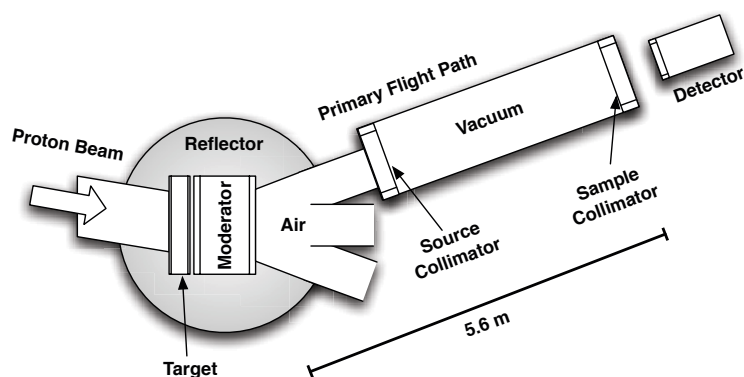
Figure 3.3: The systematic view of LENS beamline.

Neutrons were generated in the Be target from ^{9}Be(p,xn) nuclear reactions with protons. The incident protons are introduced from a commercial linear accelerator with the energy of 7 MeV. In the linac, protons have square-shaped pulse widths of 170 μs. The peak current of the linac was 8.5 mA and the frequency of the accelerator was chosen to be 15 Hz for these measurements. The Be target thickness

was chosen for its neutron yield and mechanical strength under steady-state and transient thermal stresses induced by the proton beam[69]. The proton beam of area 4×4 cm^2 is incident on the target surface at a 45° angle.

The moderator is placed right next to the target with a minimum vacuum space of 5.5 cm. The current design of TMR (Target, Moderator and Reflector) system has a room temperature light water reflector surrounding the Be target and the moderator. The cross-sectional area of the moderator was 12×12 cm^2 and the thickness of 1 cm was optimized using MCNP model[69] calculation based on the 22 K solid methane scattering kernel "*smeth22K*". This MCNP calculation exhibited a broad maximum from 1 cm to 3 cm. Therefore, we decided to choose a moderator thickness on the low end of the distribution to minimize the total amount of matter and, therefore, the neutron and gamma heat load on the moderator. In section 3.6 we revisit this optimization using our improved moderator kernel.

We used a 5.6 m primary flight path for the energy spectrum measurements. The entrance beam window of the flight tube is 1.4 m from the moderator surface. The tube was evacuated to a pressure of 0.1 mbar. A beam collimator of 7.62 cm diameter was mounted on the moderator side of the tube and the sample collimator with 2.54 cm diameter was on the detector side.

The neutrons, which are emitted from the moderator surface, first pass through 1.4 m of air and enter the vacuum tube through a single crystal Si window of 5.82

mm thickness. The neutrons leave the vacuum tube through a second 5.82 mm thick Si window and were collimated by a pinhole with 1 cm diameter. A high effi-ciency ^{3}He detector pressurized to 10 atm was placed 0.05 m past the exit window of the primary flight path to scan neutron counts. The total neutron flight length was therefore 5.65 m. The 7 MeV proton linac trigger signal was used to define the time zero for the time-of-flight measurement of the neutrons.

The Moderator Cooling

We measured the neutron energy spectrum for the solid methane moderator held at temperatures of 20 K and 4 K. The moderator vessel is made with *6061* alu-minum and is anchored to a high-purity aluminum rod (99.999%) for cooling with a mechanical refrigerator. The moderator vessel was connected to the gas handling system through a gas feed line wrapped with a 50 W wire heater to prevent freez-ing of the methane. Methane of 99.99% purity was condensed from room temper-ature with an addition of 1% of O_2 gas to ensure the neutron spin relaxation in the solid phase. The temperature of the moderator was controlled with a wire heater and an additional 50 W heater on the rod and monitored with two calibrated *Cer-nox* temperature sensors which are directly attached to the top and bottom of the cell. During the measurement, the temperature gradient between the two sensors was less than 0.1 K.

To be successful in minimizing possible cracks and holes in cooling and solid-ifying the solid methane in the moderator vessel, we followed the general procedures used for single crystal growth. The moderator vessel was first evacuated to 10^{-6} mbar at room temperature and cooled to 93 K, which is just above the crystallization temperature of solid methane. The methane gas was liquified at this temperature with a 0.5 mbar overpressure. After condensation, the liquid methane was cooled toward the solidification point at a rate of 1 K/15 min. At the crystallization temperature, the methane was annealed for 4 hours. The annealed methane was then cooled to 54.1 K. The average cooling rate in this step was about 0.5 K/min. Then the methane was cooled again toward the solid-solid phase transition temperature in methane with the same cooling rate and held at 20.4 K for 3 hours to complete the phase transformation. The moderator was then cooled to 20 K to measure the neutron spectrum. The neutron spectrum measurement at 4 K was performed after we cooled the moderator at a 0.1 K/min rate and held the moderator at 4 K for 3 hours.

Data Analysis

Mean Emission Time Correction

We want to extract the neutron energy spectrum from the observed time-of-flight measurement. Due to effects such as the finite geometry of the moderator and statistical fluctuations in the moderation process, it is possible for a neutron emitted from the moderator with one energy to overtake a slightly slower neutron that was emitted earlier. Therefore neutrons with different energies can arrive at the detector at the same time, which complicates the conversion of time-of-flight information to neutron energy [21][15].

The neutron energy spectra were calculated from the following formula,

$$C(t) = A \int_0^t dt' \int_0^\infty dE \phi(E, t') \varepsilon(E), \qquad (3.5)$$

where $\phi(E, t)$ is the energy spectrum at time t and $\varepsilon(E)$ is the efficiency of the detector. The number of counts accumulated in each time channel t_0 is

$$\frac{dC(t_0)}{dt_0} = A \int_0^\infty \phi(E, t)\varepsilon(E)dE, \qquad (3.6)$$

where $C(t_0)$ is the total number of count in the time interval $0 < t < t_0$ with $t = t_0 - \frac{L}{v}$. In the ideal case in which the flight path is very long and the emission

time distribution from the moderator is narrow one might write

$$\phi(E,t) = \phi(E)\delta(t_0 - \frac{L}{v}).$$ (3.7)

If we assume that all neutrons of a given energy are emitted from the assembly at the same instant, this equation can still hold with,

$$\phi(E,t) = \phi(E)\delta(t_0 - \tau_a(E)),$$ (3.8)

where $\tau_a(E)$ is the emission time. The emission time can be defined as

$$\tau_a(E) = \frac{\int \phi(E,t)t\,dt}{\int \phi(E,t)\,dt}.$$ (3.9)

We relied on an MCNP simulation to determine the mean emission time distribution from our methane moderator since the neutron intensity at LENS during this measurement was insufficient to determine it experimentally[69].

When we substitute Eq. 3.8 into Eq. 3.6 and integrate, we find

$$\frac{dC(t_0)}{dt_0} = A\phi(E)\varepsilon(E)\frac{2E}{\tilde{t}}\left|1 - \frac{d\tau_a(E)}{dt}\right|_{t=t_0},$$ (3.10)

where $\tilde{t} = t_0 - \tau_a(E)$. In Eq. 3.10, dt_0 is now the unit time Δt_0 and $dC(t_0)$ is

the counting rate $N(\Delta t_0)$ in the unit time with units of n/s. $N(\Delta t_0)$ should be background subtracted and normalized. This equation now includes the correction for the effect of finite emission time. Then, the neutron flux $\phi(E)$ is

$$\phi(E) = \frac{N}{\Delta t_0 A \varepsilon(E) \frac{2E}{\bar{t}} \left| 1 - \frac{d\tau_a(E)}{dt_0} \right|} \tag{3.11}$$

with the units of n/cm^2/s/meV.

The quantity we used in the paper for the comparison is the neutron spectral density $I(E)$ from the following relationship,

$$E \times I(E) = \frac{L^2}{i_p} E \times \phi(E), \tag{3.12}$$

where the i_p is the proton current averaged during the time interval. The neutron intensity $I(E)$ has units of n/meV/μC/sr.

Data Corrections

The neutron energy spectra were corrected for the effects of attenuation by the 1.4 m length of air gap, the two 5.82 mm Si windows[70], the 0.5 mm of stainless steel cylindrical detector body and for the efficiency of ^{3}He detector.

The first correction was the attenuation caused by the air gap. Between the

moderator and the vacuum tube, there was $1.4m$ length of flight pass filled with 1 atm air which also attenuates the neutron intensity. We assumed that the air contains roughly 78.1% of Nitrogen, 20.96% of Oxygen and 0.94% of Argon in 1 atm. The attenuation due to the air varies from 11% to 3.8% for 0.1 meV $\sim$ 1 eV respectively.

The 4.2 m tube was evacuated with two mechanical pumps during the experiment. In addition, it had two single crystal *Si* windows on each side which had a thickness of 5.82 mm. The correction for the *Si* windows was obtained from an effective cross section approximation.

The use of large single crystals of various materials like *Si* as a filter for thermal neutron beam has long been known[10]. At high neutron energies, greater than about 1 eV, the total neutron cross-section σ_t of each of the materials is in the range of a few barns. But, at lower energies, much of the coherent "Bragg" scattering is disallowed. Then, the effective cross-section for the single crystal is reduced to the several contributions: absorption σ_a, incoherent σ_{inc}, coherent inelastic σ_{inel} and any residual Bragg scattering σ_{el}. The effective cross section is thus determined by [70]

$$\sigma_{eff} = (\sigma_a + \sigma_{inc} + \sigma_{inel} + \sigma_{el}). \tag{3.13}$$

In Table 3.1, we list the relevant cross section of the material we used for the

correction. The values of σ_a refers to 1.8Å(25 meV) neutrons.

Element	Absorption	Incoherent	Coherent	Total
Al	0.230	0.1	1.469	1.43
Si	0.16	0.02	2.163	2.25
Fe	2.56	0.4	11.22	11.62

Table 3.1: Cross Sections of Elements in unit of ($b = 10^{-24}cm^2$).

All these cross-sections are reasonably well known quantities and are independent of orientation, perfection and temperature of crystals. The lowest possible effective cross section is obtained when the contributions of σ_{inel} and σ_{el} are eliminated [70],

$$\sigma_{eff} = (\sigma_a + \sigma_{inc}).$$ (3.14)

The attenuation due to these windows ranges from 12 % to 6.8 % for 0.1 meV $\sim$ 1eV respectively.

The attenuation for the 0.5 mm thickness of stainless steel detector body was about 10.5% to 2.5% for 0.1 meV $\sim$ 1eV respectively.

The efficiency of the neutron detector depends on ^{3}He absorption cross section through the reaction

$$_2^3He + _0^1 n \rightarrow_1^3 He + _1^1 p, \ Q = 0.764 \text{ MeV}.$$ (3.15)
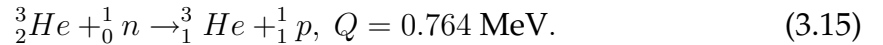
The thermal neutron cross section for this reaction is 5330 barns for a 25 meV neutron. The detector efficiency for the neutron incident along the ^{3}He detector tube is approximately given by

$$\varepsilon(E) = 1 - \exp(-n\sigma_a l), \tag{3.16}$$

where n is the number density of the atom, σ_a is absorption cross section of ^{3}He at energy E and l is active length of the detector tube. Using Eq. 3.16 we find the calculated efficiency for the 1 cm diameter tube filled with 10 atm of ^{3}He is 99.14% at thermal neutron energy (25 meV) but drops to 3.9% at 1 eV. Thus a ^{3}He tube exposed to neutrons with various energies responded principally to the slow neutron component. Eq. 3.16 slightly over estimates the neutron counting efficiency because there usually are some regions near the end of the tube in which charge collection is inefficient. This results in a reduced neutron detection efficiency. This dead space near the wall was considered in the efficiency correction [71]. The efficiency correction for the dead space near the wall end can be expressed as:

$$\varepsilon(E) = \exp(-n\sigma_a \Delta l)\left[1 - \exp(-n\sigma_a l)\right], \tag{3.17}$$

where Δl is the length of dead space at the end of the wall ($\Delta l/l \approx 0.001$ for this correction)[72].

Energy Resolution

In time-of-flight measurements, distortions of the spectrum come from the uncertainty of the flight path length (δL), the finite width of the time channels (δt_c) and from the imprecise determination of time zero when neutrons start along the flight path (δt_f)[15]. The contribution to the energy resolution arising from the finite channel width, the uncertainties in the flight-path length and uncertainty in the flight time is [15]

$$\delta E \simeq E \left(\left(\frac{2\delta t_f}{t_f} \right)^2 + \left(\frac{2\delta t_c}{t_f} \right)^2 + \left(\frac{2\delta L}{L} \right)^2 \right)^{1/2}, \qquad (3.18)$$

where δt_f is the $\tau_a(E)$ and t_f is flight time, and δt_c is the time channel width Δt_0 [15]. For the high efficiency ^{3}He detector, $\delta L = \lambda(E)$, the energy-dependent absorption mean free path of neutrons in the detector. The correction for the spectrum distortions gives a slight change for neutrons with energy less than 2 meV.

3.4   Neutron Energy Spectrum Calculation

The MCNP neutron transport code was used to calculate the neutron energy spectrum. The MCNP scattering kernels were produced using NJOY nuclear data processing system with the frequency spectrum for solid methane at 20 K and

4K from our model[59]. We named these kernels "*y-smeth20K*" and "*y-smeth4K*".
The geometry for MCNP simulation was the same as that used for the time-of-flight measurements. A schematic view of the TMR (Target-Moderator-Reflector) is shown in Fig. 3.3. The neutron energy spectra emitted from the moderator was evaluated by point tally. Fig. 3.4(a) and 3.4(b) show the calculated neutron energy spectrum at 20 K and 4 K. In the 20 K plot, the neutron energy spectrum calculated with MCNP scattering kernel at 22 K (*smeth22k*) from Harker & Brugger frequency spectrum[34] is also shown. The calculation with the 22 K scattering kernel is close to our 20 K kernel although there is a difference in neutron energy below 100 meV. This kernel was used in the initial design of the LENS TMR system[69].

3.5   Results and Discussion

Fig. 3.5 shows the neutron energy spectra from the solid methane moderator in the LENS TMR system. The neutron energy range extended from 0.1 meV~ 1 eV. The simulations were compared to the measurements at 20 K and 4 K. The MCNP simulation used new scattering kernels, "*y-smeth20K*" and "*y-smeth4K*" at each temperature. In the 20 K plot, we also present the MCNP simulation with "*smeth22K*" which was generated from the frequency spectrum as determined by a measurement by Harker & Brugger at 22 K. In this figure, we present the data as
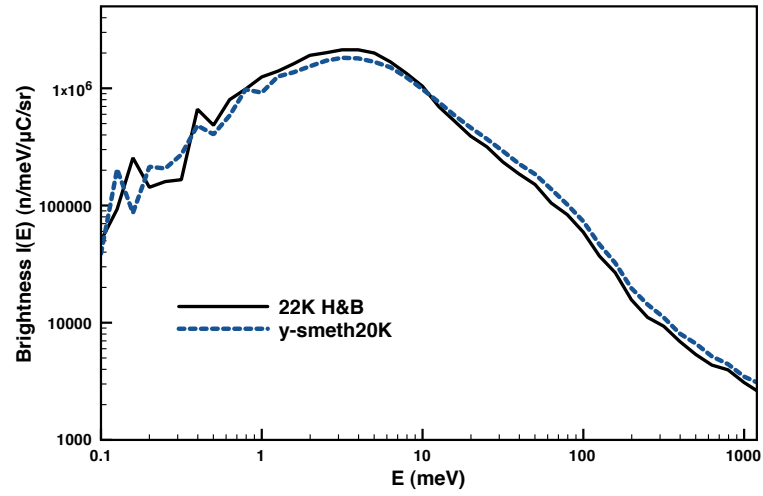
(a) 20K
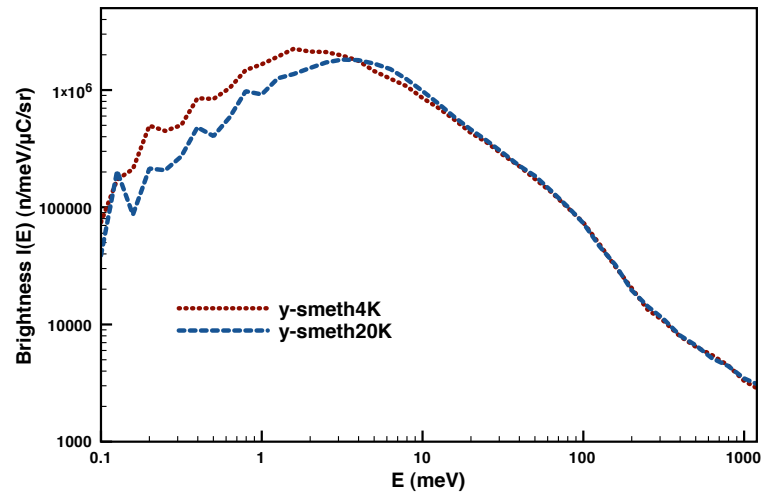
(b) 4K

Figure 3.4: The energy spectra of solid methane at 20K and 4K with 1cm moderator thickness.

a lethargy plot to allow the difference between the data and calculation at lower energy to be easily discerned.

The measured neutron energy spectrum at 20 K shows very good agreement with the MCNP simulation using our "*y-smeth20K*" kernel throughout the neutron energy range. The MCNP simulation with "*smeth22K*" kernel overestimates the measured intensity in the spectrum in the energy range below 10 meV.

The measured neutron energy spectrum at 4 K agrees with the MCNP simulation with our "*y-smeth4K*" kernel in the energy range above 5 meV. There is a significant difference between data and model in the 4 K case at energies below 2 mV. Fig. 3.6 is the comparison of the measured neutron spectrum at the 20 K and 4 K. It is clear that the 4 K measured spectrum lies slightly below the theoretical prediction around 2 meV neutron energy.

3.6   Sensitivity of LENS Neutron Brightness to the CH_4 Moderator Thickness

In Fig. 3.7, we also present the ratio of neutron spectrum from the 4 K and 20 K moderator temperatures from measurement and from simulation. The ratio
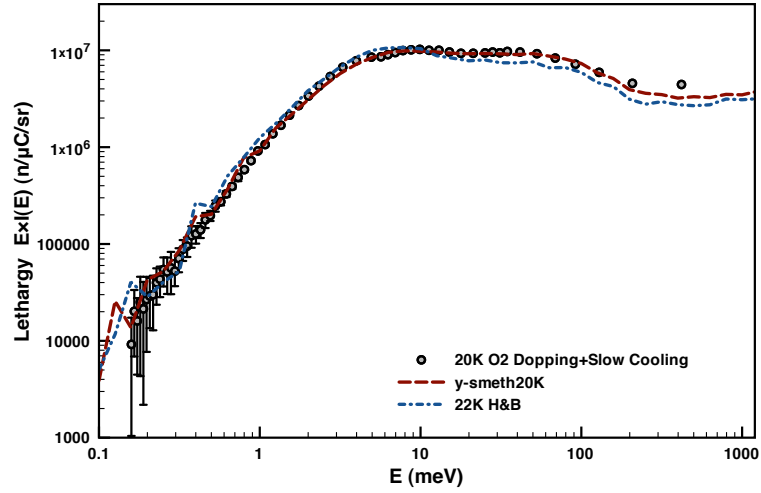
(a) 20K
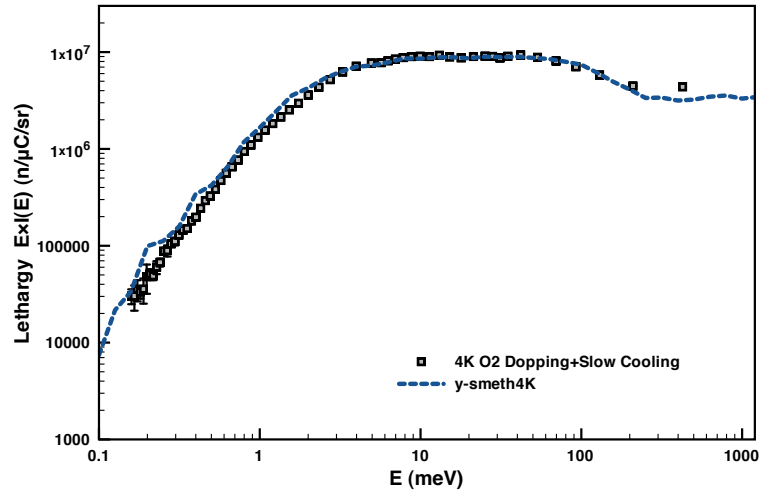
(b) 4K

Figure 3.5: The measured neutron lethargy at 20 K and 4 K compared with the MCNP calculation using the scattering kernel *y-smeth20K* and *y-smeth4K*.
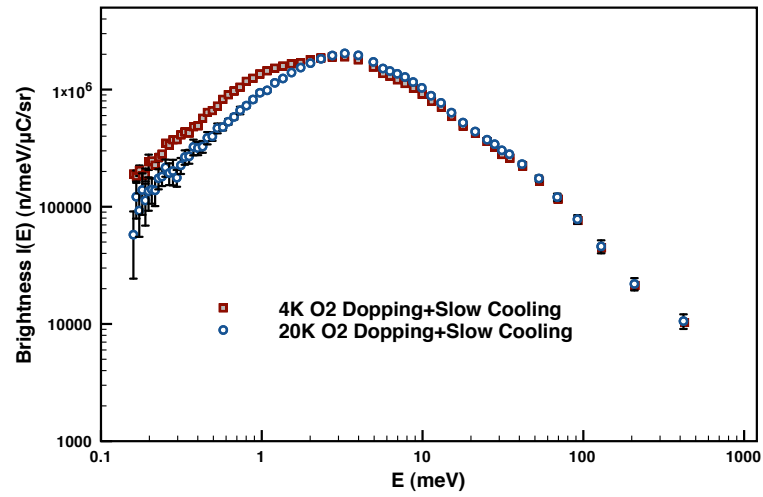
Figure 3.6: Neutron energy spectrum at 20 K and 4 K.
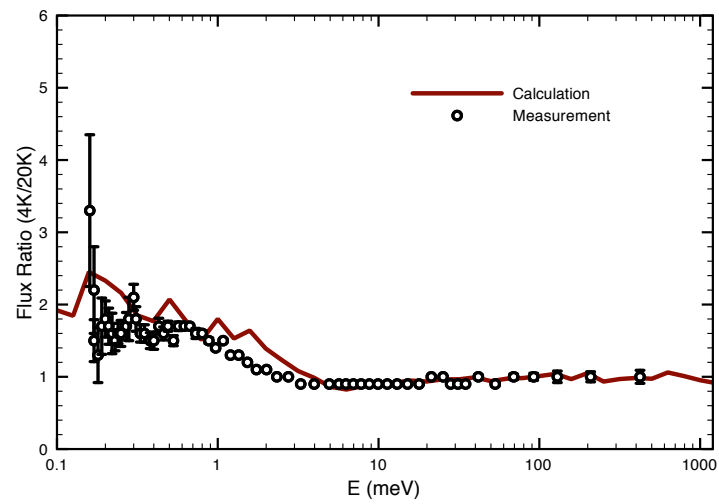
Figure 3.7: The ratio of 4 K and 20 K neutron energy spectra.
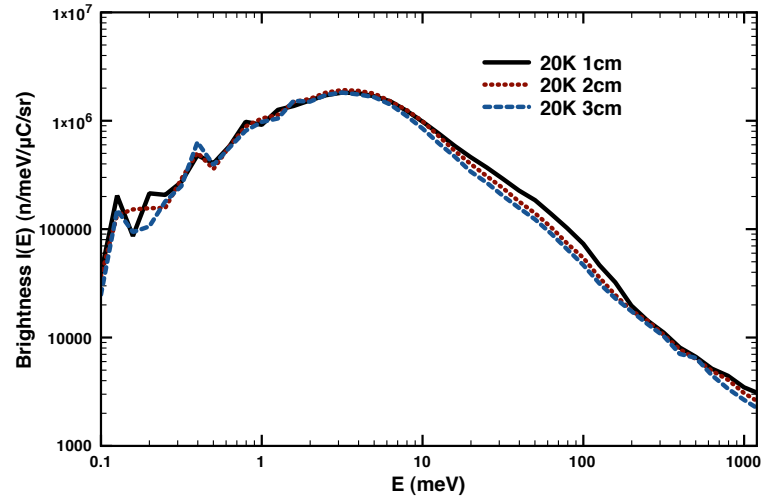
(a) 20K
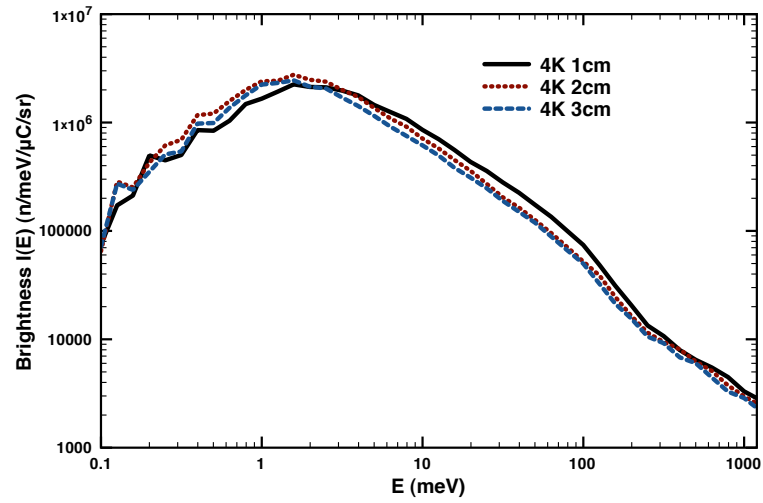
(b) 4K

Figure 3.8: The energy spectra of solid methane at 20K and 4K with various moderator thicknesses.

cancels some common systematic errors in the two measurements and should be more sensitive to the temperature dependence of the methane moderation physics. The intensity of cold neutrons is increased for the lower moderator temperature as one would expect, and the ratio agrees quite well with the expectation from the MCNP simulation with our new scattering kernels, "*y-smeth20K*" and "*y-smeth4K*".
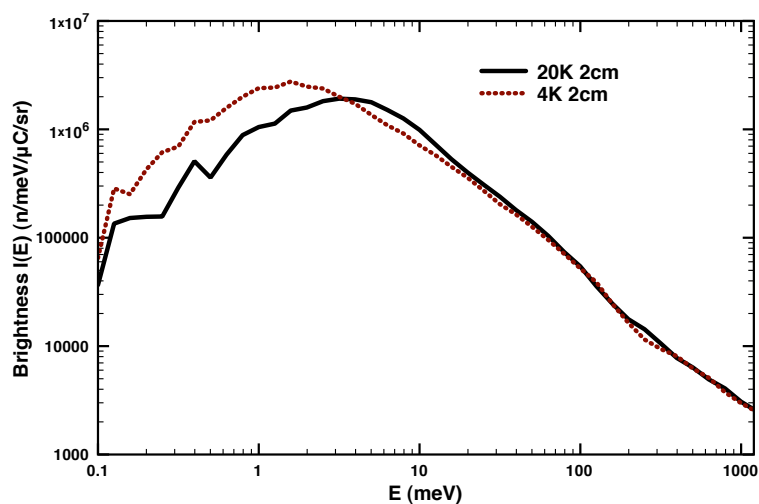
Figure 3.9: The neutron energy spectra with 2cm moderator thickness.

We also use these kernels to investigate the relationship of the LENS neutron spectrum to the methane moderator thickness. We increased the moderator thickness in the MCNP model from 1 cm to 2 cm in our simulation and then to 3 cm and performed MCNP simulations with our 20 K and 4 K kernels. At 20 K, the shape of the spectrum is unchanged and the intensity of cold neutrons is reduced by

about 35% as the thickness is increased from 1 cm to 3 cm. This result implies that the moderator with 1 cm thickness is the optimal thickness in the 20 K moderator temperature with our LENS TMR configuration.

As the moderator thickness is increased to 2 cm at 4 K, shown in Fig. 3.8(b), the neutron spectrum is shifted to a lower energy region and the cold neutron intensity increases by 20%. With a further increase of the thickness to 3 cm, the cold neutron intensity decreases. We therefore predict an increase in the cold neutron brightness from our 4 K solid methane moderator at LENS by about 20% with an increase of the moderator thickness to 2 cm.

4

Methane Clathrate as a Moderating Medium for Very Cold Neutron Source

"Very Cold Neutrons" (VCN) are neutrons in the subthermal energy range below 1 meV which still move quickly enough to form recognizable beams. VCN beams with sufficient phase space density would be of great interest for scientific studies in neutron physics and scattering. Existing neutron moderator materials used for cold neutron sources do not possess a sufficient density of low energy modes to produce a spectrum with a peak in the VCN regime. We present a study of the separate contributions of different low energy excitation modes to the neutron moderation and calculate the effective neutron spectrum temperature from

separate modes as a function of moderator temperature for the LENS TMR geometry. We suggest an example of an existing material, methane clathrate, as a possible VCN neutron moderator. Unlike present cold moderator media, methane clathrate possesses low energy free rotor modes of sufficient density and neutron scattering cross section at low temperatures to act as a VCN moderator.

4.1   Introduction

Recent progress in cold neutron moderation makes an important contribution to the improvement in the quality of low energy neutron sources. Using low temperature hydrogenous condensed moderator systems, the intensity of cold neutrons with the energy range between 0.1 meV∼5 meV produced in various facilities has been significantly increased over the last few decades. However, the range of energies in the spectrum has been almost unchanged for this period of time. Very recently, several research groups in the world attempted to produce much colder neutron beams and to search for their application to condensed matter and fundamental physics. Among these colder neutrons, the neutrons with the wavelength longer than 10Å are generally called "Very Cold Neutrons". So far VCNs have been usually produced as a "by-product" from ultra-cold neutron (UCN) sources. They are extracted through bent or curved guide tubes to the experimental area.

The intensity of VCN is, however, still very low compared with the intensity of cold neutrons.

The motivating idea behind a very cold neutron (VCN) source is to shift the neutron energy spectrum into the VCN energy regime while keeping their intensity in this energy regime as close as possible to present cold neutron intensities. The VCN energy regime is loosely defined as a regime below 1 meV, and its lower limit is defined in practice by the point at which the effects of the Earth's gravity on neutron trajectories are so great that it is no longer possible to produce a recognizable neutron beam for neutron scattering measurements. Some early studies of the potential scientific impact and possible source and instrument designs of a VCN neutron source have appeared in the literature[73]. If intense very cold neutron beams can be realized, they could have a large impact on scientific areas such as nano science, soft condensed matter and energy related research.

For neutron moderation in the VCN regime, we are typically trying to shift a broad distribution of neutron velocities to values below 1 meV. As mentioned in chapter 1, the width of the neutron distributions in phase space that we wish to cool is typically larger than the range in (Q, ω) space over the moderator medium. Normally, the intensity of $S(Q, \omega)$ is large only in narrow range of (Q, ω) space because of the presence of well-defined elementary excitations of the medium such as phonons, magnons, librons, etc. For cooling a broader phase space distribution

of neutrons to energies in the $100~\mu$eV ~ 1meV range, it is important for $S(Q,\omega)$ to possess some strength near $\omega \to 0$ so that the largest number of neutrons in the distribution have energy losses ω_i in some sequence of collisions $S(Q,\omega_i)$ that can allow them to approach $E_f \to 0$. Therefore, the creation of single elementary excitation which can process multi-energy excitations with small ω_i may be necessary in the VCN moderation.

In this chapter, we present the characteristics of neutron slowing-down in condensed matter moderator medium with different excitations. These considerations guide the search for improved neutron moderating media into some obvious directions. From this study, we suggest that methane clathrate can be an excellent candidate for a VCN moderator medium. Methane clathrate is a nonstoichiometric inclusion of methane in an ice cage. The interesting feature of the motion of the methane molecules in this matrix is that, to a reliable approximation, it is close to that of a free 3D rotor. The dynamics of the methane motion in this material is actually simpler than that for the motion of solid methane in phase II, in which $1/4$ of the methane molecules are on lattice sites that allow free rotation and $3/4$ are in positions which possess hindered rotations. Recently we have completed a microscopic theory for the dynamic structure factor $S(Q,\omega)$ of CH_4 in phase II whose predicted moderator spectra are in good agreement with measurements performed

at the Low Energy Neutron Source (LENS) at the Indiana University Cyclotron Facility (IUCF)[59]. We have adapted our theory for CH_4 in phase II to the dynamics of CH_4 in clathrate based on the neutron scattering information provided in recent work on this material.

4.2   The Effective Neutron Spectrum Temperature

Our search for very cold neutron moderator material was motivated by a need to increase the neutron intensity below 1 meV. McReynold and Whittermore[19] first studied the cold neutron spectra and the effective neutron temperature of methane and hydrogen for the pulsed cold neutron source with limited results. Inoue *et al.*[22] studied several cold neutron moderator materials for their capability to produce appropriate spectral shapes and sufficient cold neutron gains in moderator operation. This study included methane, ethane, hydrogen and light water at various temperatures down to 15K.

All neutron spectra exhibited their own characteristic shapes due to the different threshold of the excitation in molecular motion of moderator materials. The behavior of the effective neutron spectrum temperature of three different moderator materials as a function of moderator temperature were presented as shown

in Fig. 4.1. The neutrons seemed to be prevented from reaching thermal equilibrium with the moderator. It was suspected that this phenomenon was mainly caused by the ineffectiveness of the smallest energy transfer mechanism available. Among the neutron spectra, the one from solid methane at 12K showed the lowest spectrum temperature ($\sim$20K).
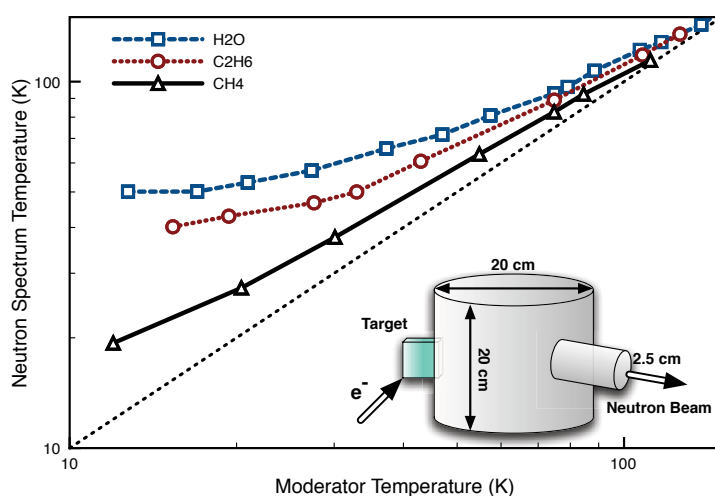
Figure 4.1: Effective neutron temperatures of three moderator materials as a function of moderator temperature from Inoue *et al.*[22].

At about the same time, Utsuro[11][38] developed an analytical approach to understand the neutron slowing down process in moderator material. In his papers, Utsuro attempted to derive the effective neutron spectrum temperature in a cold moderator from the separate collective modes of the moderator material such as inter-molecular lattice vibrations and intra-molecular rotations. As pointed out

by Inoue[22], cold neutron moderation and the formation of the spectral peak in cold moderator were strongly affected by the excitation giving the smallest energy transfer.

In the present chapter, we investigate the relationship between the moderator temperature and the spectrum temperature of cold neutrons slowed down by individual collective modes of the moderator material in the LENS TMR geometry. This relation was formulated by Utsuro in high temperature limit[11] and also experimentally examined by Inoue down to 20K limit[22]. It was claimed by Inoue that there is a certain limit of the neutron spectrum temperature below which it couldn't be lowered even if we lower the moderator temperature further. Thus, the present work addresses an important issue for very cold neutron moderation.

In condensed matter systems at low temperature, only a few elementary excitations are responsible for the internal energy of the system, including intramolecular vibrations, inter-molecular lattice translations and intra-molecular rotations.

The intra-molecular vibrations form the optical branch of lattice vibrations. These optical branches are characterized by relatively narrow frequency bands which can approximately be represented by a single frequency in frequency spectrum. The excitation energy of vibrations is in most cases larger than the energy of

cold neutrons. For example, solid methane has four normal vibrations with characteristic energies of $\hbar\omega_0 = 168, 172, 376$ and 391 meV [54]. These are rather effective at cooling neutrons to the energy range of $\sim$ eV.

In addition, the inter-molecular translational motions have a broad band of low frequency acoustic branch of lattice vibrations in the solid. These provide a slowing-down mechanism effective for cold neutron moderation in many moderator media.

However, it is no longer effective for very cold neutron moderation. Utsuro[11] showed the neutron spectrum temperatures as a function of Debye temperature of the solid which is a useful average characterization of lattice vibration energy considering the neutron moderation only by phonon creation. This study indicates that the neutron slowing-down by lattice vibration loses its effectiveness in shifting the neutron spectrum temperature to the very cold energy regime ($E_n <$ meV).

On the other hand, there are intra-molecular single particle rotations with multiple excitations spectrum which play an important role in the further slowing-down of cold neutrons. In some materials, the rotational motions are weakly hindered so that their motion is almost free. In other cases, this motion is strongly hindered by the crystal field so that they show tunneling among rotational ground states or libration in higher energy states. Inter-molecular rotation in solid methane is one of the most weakly hindered cases due to the high symmetry of methane

molecule.

Solid methane in phase I ($T > 20$ K) has an almost free rotational mode. However, in the low temperature phase, solid methane has two different rotational motions at the same time. While solid methane shows a mix of ordered and disordered states with respect to its rotational motion below 20 K, the orientationally disordered symmetry still provides low-lying energy levels of free rotation in molecules even at $T \sim 0$ K.

Recently, we developed a microscopic model of neutron structure factor of solid methane in phase II[59]. Using this model, we could study the separate contributions of individual collective mode in solid methane to the inelastic cross section in the cold energy regime. We tested this model by calculating the neutron brightness expected from the solid methane moderator at 20 K and 4 K using the Monte-Carlo MCNP code. Our model correctly predicted the neutron brightness of the LENS moderator at both temperatures.

We apply this model to study the effective neutron spectrum temperature as a function of solid methane moderator temperature in a low temperature limit. The geometry we used for this study is based on the TMR assembly of the Low Energy Neutron Source (LENS) at Indiana University Cyclotron Facility (IUCF). The details of this setup are described in Ref. [69]. Our neutron flux simulations started from a 2 cm thickness moderator with a 12cm $\times$ 12cm surface area since it was

shown in our previous works described in chapter 3 that the neutron brightness

with 2 cm thickness of the moderator has the most intensity at the lower tempera-

ture.

First, the neutron brightness from solid methane moderators at 10 K, 7 K and

4 K were calculated to find the effective neutron spectrum temperatures. We as-

sumed the total nuclear spin relaxation for the protons in CH_4 in the simulation.

The neutron brightness for the three different moderator temperatures are plotted

in Fig 4.2.
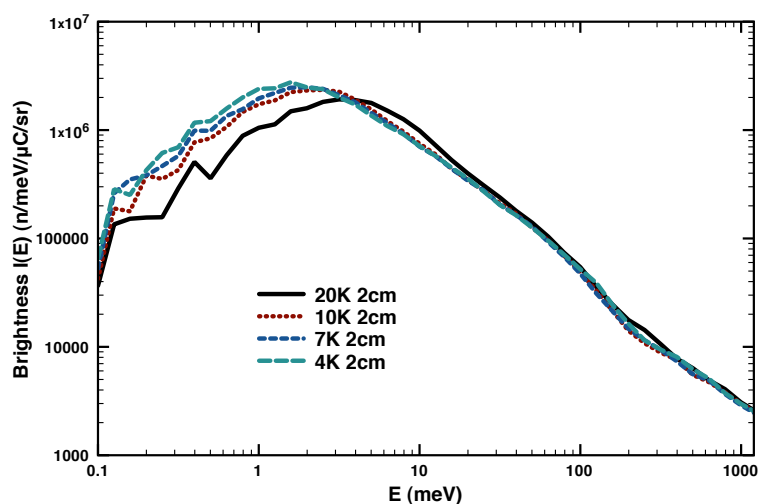
Figure 4.2: Neutron spectra of solid methane moderator at low temperatures.

In the neutron spectra plot, the spectrum temperatures converge to a 19.7K

Maxwellian temperature of the neutron spectrum as the moderator temperatures

are lowered. This means that even though we cool further down the solid methane moderator below 4K, we may not expect further spectrum temperature shifts. This is because the inter-molecular vibrations strongly hinder the neutrons slowing down so that this mode no longer contributes to neutron moderation. This is also consistent with what Utsuro[11] claimed in the relationship of neutron temperature with Debye temperature of solid. Solid methane has a 145K Debye temperature, and the limiting temperature of 150K Debye temperature is about 20K in his calculation.

Next, we separate the excitation modes, which solid methane has in the low temperature limit, into four different combinations of modes: hindered rotation and phonon mode, hindered rotation only mode, free rotation and phonon mode and free rotation only mode. We include intra-molecular vibrations in all cases since it is due to the intrinsic motion of single molecules and therefore must be always present. The thickness of moderator was varied from 1cm up to 3cm.

Fig. 4.3 shows the neutron brightness in the four different excitation modes of solid methane at 4 K. Fig. 4.3(a) and 4.3(b) present the neutron spectrum from hindered rotation with phonon and without phonon, resepctively. In these cases, the neutron brightnesses are the same as normal solid methane at 4 K or even less in the case of hindered rotation with phonon mode. For the cases of free rotation
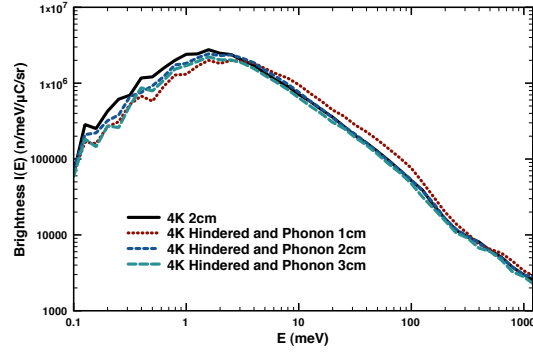
(a) 4K Hindered Rotor and Phonon
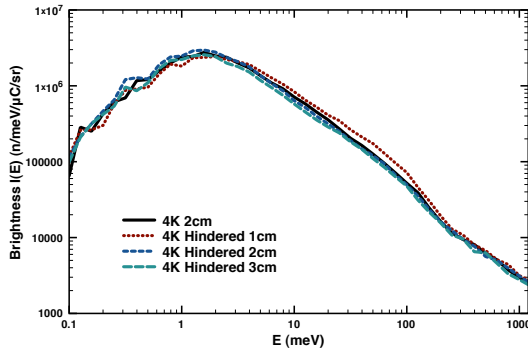
(b) 4K Hindered Rotor
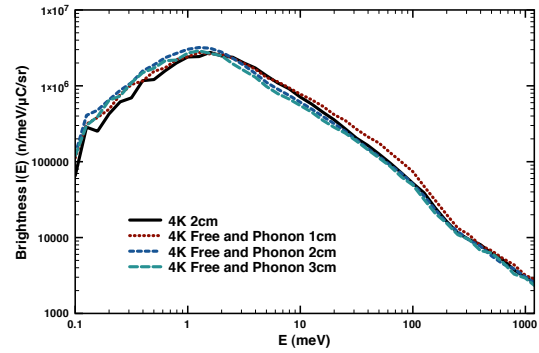
(c) 4K Free Rotor and Phonon
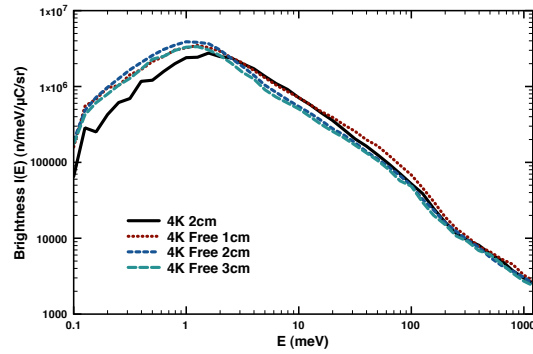
(d) 4K Free Rotor

Figure 4.3: Neutron brightness from different combinations of excitation modes in solid methane at 4 K.

with and without phonon modes, Figs. 4.3(c) and 4.3(d), respectively show a significant improvement of the neutron brightness at the energy range below 1 meV. In both cases, the neutron brightness shows the maximum intensity with the 2cm moderator thickness. The relative comparison of these four different combinations of modes in solid methane at 4 K with 2cm thickness is presented in Fig. 4.4.
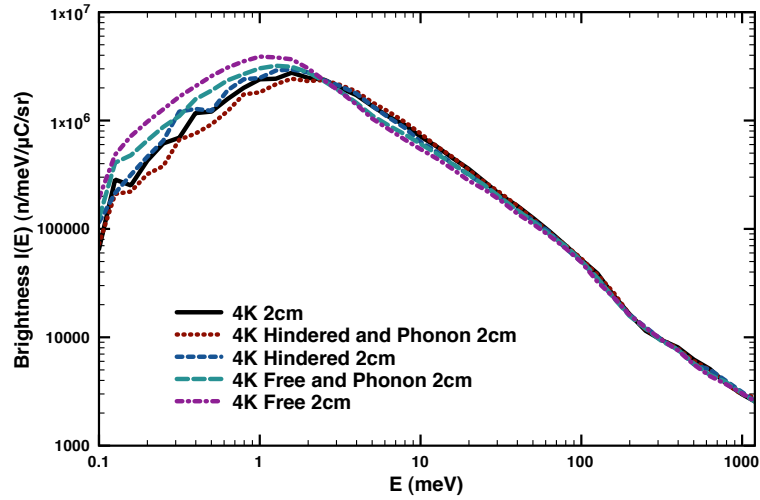
Figure 4.4: Neutron spectra of solid methane moderator with different excitation modes at 4 K.

The effective spectrum temperature of each case is fitted with a Maxwellian distribution,

$$\phi_M(E) = \frac{1}{(k_B T)^2} E \exp\left(-\frac{E}{k_B T}\right), \tag{4.1}$$

where k_B is Boltzmann's constant and T is the absolute temperature of the moderator. This is the distribution for thermodynamic equilibrium between neutrons

and moderator. Fig. 4.5 shows the effective neutron spectrum temperatures in each case together with solid methane at 12 K from Inoue *et al.*[22]. The effective neutron spectrum temperature from solid methane at 4 K moderator temperature is around 19K. However, with only free rotation mode of solid methane at 4 K, the spectrum temperature can be shifted to ∼12 K. This is because the multiple energy excitations spectrum of free rotations in solid methane provides more effective energy transfer to a broader range of incoming neutrons with small transferring energies ($\sim$ 1meV). Even though the hindered rotations have similar excitation spectrum, this mode is mainly separated into two branches, tunneling modes and librations. The tunneling levels among ground states are still too small in energy ($0.1 \sim 0.2$ meV) and the librations are too high in energy (~ 6.5 meV) so that the hindered modes are actually effective only for a limited energy range of incoming neutrons. Therefore, the almost free (weak hindrance) and intense rotational motions are the desired modes for very cold neutron moderation.

4.3   Methane Clathrate Hydrate

Almost free quantum rotations of the methane molecule even in a solid state are a rare phenomenon and only a few other materials share this property[35].
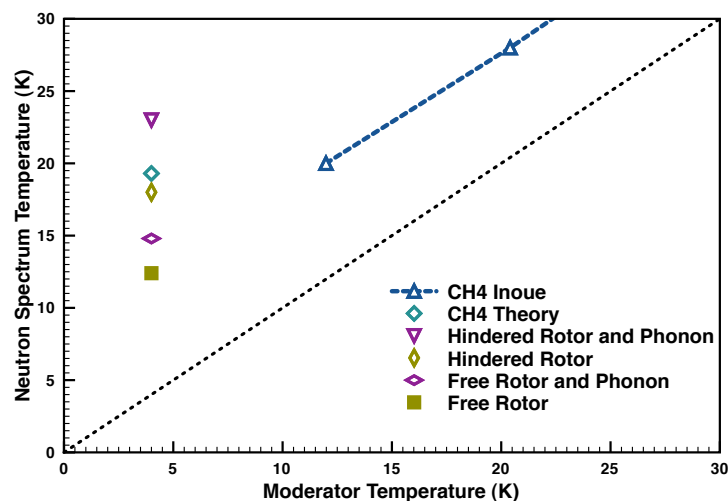
Figure 4.5: Effective neutron temperatures of four different modes of solid methane at 4K moderator temperature compared with data from Inoue *et al.*[22].

Clathrate Hydrates are a special class of inclusion compounds, in which small hydrophobic guest molecules or atoms are trapped in a cavitiy formed by an ice-like host lattice of water molecules[74]. The cavity is large enough to cage only a single guest. This unique structure makes clathrate suitable for molecular isolation. Most of low molecular weight gases including methane form hydrates at low temperatures and high pressures. There are elements and molecules that can be a guest molecule such as O_2, Ar, N_2, CH_4 and Xe[75].

Methane hydrate is a nonstoichiometic inclusion compound of methane with

host framework of water cages in a unit cell. The cages allow for almost free rotation of the methane molecule at low temperature; The molecular motion is quantitatively described as a single particle quantum rotation in a weak orientational potential[76].

Most of methane hydrate has one of the two different crystal structures, cubic structure type I or cubic structure type II. Structure type I hydrates consist of 2 small spherical cages and 6 large ellipsoidal cages, whereas the structure type II is formed of 16 small and 8 large cages, both of which are nearly symmetrical. As 80% of both structures consist of hydrogen bonded water molecules, many of their properties resemble those of ordinary ice[77].

The rotational motion of methane has been an interesting subject for a long time in many area of physics including cold neutron source design. Methane hydrate can be regarded as a discrete system of methane molecular motion because the methane molecules are separated from each other by water cages. Therefore, methane hydrate can be considered as a possible candidate material for a very cold neutron moderator in a pulsed neutron source because of the almost free rotations of single methane molecule in a cavity. There were inelastic neutron scattering experiments[78] and spectral measurement of methane clathrate at 20 K which show the free rotor motion[79].

Among the several types of methane hydrate, methane in a polycrystalline of

deuterated (D_2O) structure I clathrate hydrate may be an attractive medium for VCN moderator for several reasons[78].

First of all, methane hydrate possesses free rotations of the methane molecules. The frequency of the low energy rotation is similar to free rotation of solid methane in phase II or CH_4 isolated in a rare gas matrix[58]. This peak is mainly assigned to the $J = 0 \rightarrow 1$ quantum rotational excitation inside the clathrate hydrate cages. At 4K, most of CH_4 molecules occupy their rotational ground state. The observed rotational excitation energy is 1.03meV. Those of CH_4 isolated in solid argon, krypton, and xenon matrix have 0.89, 0.98, and 1.13 meV, respectively[80]. These values are close to the free rotor limit of 1.3 meV. It indicates that the rotational motion is slightly shifted by the molecular field created by the water molecule forming the cavity. On the other hand, inter-molecular vibrations of methane molecules are strongly restricted with the deuterated ice cages.

Second, ^2D and ^{16}O have very low absorption cross sections with the $^2D = 5.2 \times 10^{-4}$b and $^{16}O = 1 \times 10^{-4}$b. This low absorption cross section of D_2O ice may be a help to increase the VCN flux. The total scattering cross section of D_2O ice is also low enough to minimize the neutron interaction with D_2O ice with relatively strong coherent scattering, $^2D = 5.59$b and $^{16}O = 4.23$b, than incoherent one, $^2D = 2.04$b and $^{16}O = 0$b. Fig. 4.6 shows the total neutron scattering cross section of D_2O ice at 77 K and 15K[81].
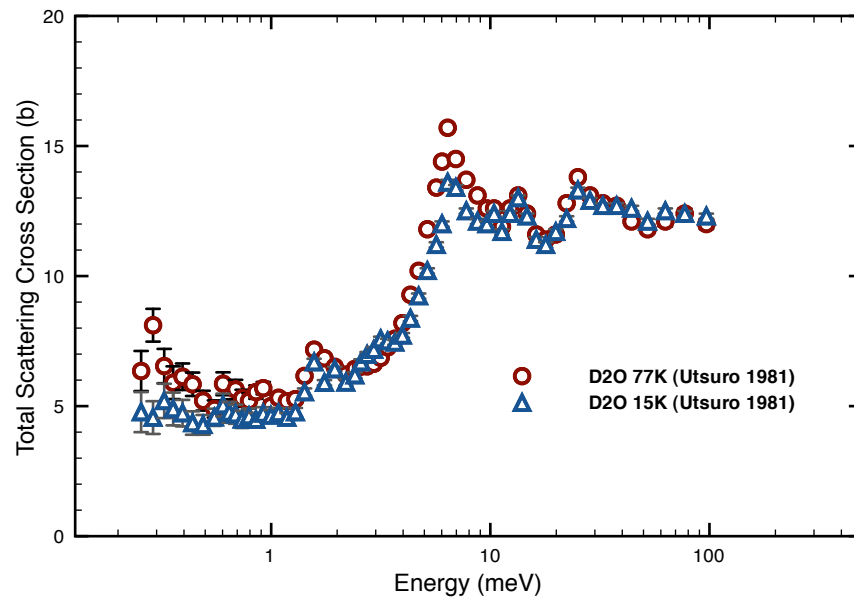
Figure 4.6: Total neutron scattering cross section of D_2O ice at 77K and 15K[81].

Therefore, we suggest methane clathrate at low temperatures can be a potential very cold neutron moderator material because it combines the strong neutron slowing down properties in free rotations of methane molecules with the effective exclusion of phonon scattering from the methane lattice and the very low absorption cross section of heavy ice.

5

Experimental Setup for Ultra-cold

Neutron Production in Solid Oxygen

Solid oxygen is a material with a new concept of ultra cold neutron production using neutron down-scattering from a single magnon excitation. The magnon excitation in solid α oxygen for UCN production was first suggested by Liu *et al.*[82]. The characterization of solid oxygen crystal is needed to judge the solid oxygen as a UCN converter material. This chapter presents a setup for crystal growth of solid oxygen and a neutron scattering experiment including a cryogenic solid oxygen cell, magnet system and gas handling system. We also report on the preliminary experimental test of ultracold neutron production with the setup.

5.1   Introduction

Ultra-cold neutrons (UCN) are neutrons with very low energies of a few hundred neV, or several mK. Their energy is low enough to undergo total reflection from a given surface at any incident angle. Therefore, they can be stored in material vessels for significant periods of time when their kinetic energies are lower than the potential of the material. At the same time, they can be lost through nuclear absorption or be up-scattered through thermal inelastic scattering from the material surface. If their energy is sufficiently higher than Fermi potential of the material, they also can be lost by quasi-elastic scattering. UCN offer the attractive possibilities of important applications to fundamental physics experiments such as measurement of electric dipole moment of neutron[7].

Among a few methods of UCN production[83], Golub and Pendlebury proposed the super-thermal method[84]. In a super-thermal source, UCN are produced by down-scattering of cold neutrons. Cold neutrons lose their energy by exciting the collective modes of the converter material and are thereby down-scattered. However, neutrons can be up-scattered if the neutron gains energy from the excitation of the converter. Up-scatterings can therefore be suppressed by lowering the temperature of the converter. The translational motion plays an important role for producing UCN in converter material as a super thermal source. The

nuclear absorption mainly limits the increase of UCNs in a converter. Super-fluid ^{4}He and deuterium molecules in solid (liquid) are very attractive UCN source materials because of their small (zero for ^{4}He) absorption cross sections.

Their common principle of the UCN moderation is to expose the converter to a high flux of cold neutrons and to down scatter a fraction of the cold neutrons to UCNs. In this case, the UCN production rate obviously depends on several conditions such as cold neutron flux, extraction efficiency and transport efficiency.

Recently, Liu *et al.*[82] proposed solid oxygen as an alternate UCN converter material and compared the UCN production rate in solid oxygen with solid deuterium. Solid oxygen has about five times smaller nuclear absorption cross section than solid deuterium. In addition, solid molecular oxygen O_2 at low temperature possesses a long range anti-ferromagnetic spin system. When this system is disturbed by neutron scattering, the exchanged energy is shared among neighboring spins and spreads out through the spin system. This behavior is very similar to lattice vibrations. The only difference is that it happens in the spin system. The excitations are called "spin waves" and its quantum is called a magnon. Fig. 5.1 illustrates the spin wave in the spin system. Liu *et al.*[82] performed a theoretical study of UCN production in solid oxygen using the neutron interaction with this magnon. It was shown in the calculations that the interaction rate is comparable to that with phonons.
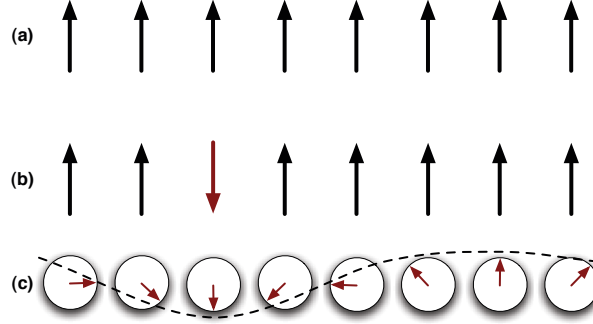
Figure 5.1: (a) Ground state spin alignment of a simple ferromagnet. (b) An isolated spin is reversed, which costs a lot of energy. (c) A lower energy excitation is achieved by sharing the disturbance among neighboring atoms[5].

In this chapter, we present an experimental setup for solid oxygen crystal growth and for utilizing the magnon interaction in UCN production. This chapter also reports on the result of preliminary measurements of UCN production in solid oxygen.

5.2   Solid Oxygen

Oxygen is a homonuclear diatomic molecule with two unpaired electrons in the π_g valence molecular orbitals derived from the $2p$ shell of each oxygen atom. The ground-state molecular-orbital configuration of the oxygen molecule is [85]

$$(1\sigma_g^+)^2(1\sigma_u^+)^2(2\sigma_g^+)^2(2\sigma_u^+)^2(1\pi_u^+)^4(3\sigma_g^+)^2(1\pi_g^+)^2. \tag{5.1}$$

Three molecular states may arise from the open-shell $(\pi_g)^2$ configuration, $^1\Sigma_g^+$ ($S = 0, l = 0$), $^1\Delta_g$ ($S = 0, l = 2$), and $^3\Sigma_g^-$ ($S = 1, l = 0$), which are a result of the six possible ways for the two electrons to be placed in the π_g orbitals. The degeneracy of each state is given by $(2S + 1)$ for $l = 0$ and by $2(2S + 1)$ for $l \neq 0$, where S is the total spin quantum number and l is the component of the resultant electronic orbital angular momentum parallel to the internuclear axis. The subscripts g and u in the spectroscopic notation for the molecular states denote even and odd states under inversion through the center of the molecule, and the superscripts $+$ and $-$ for the Σ states refer to even and odd states with respect to reflection in any plane containing the internuclear axis[86].

In the absence of external fields and at low temperatures, all oxygen molecules in the solid are in their electronic ground state $^3\Sigma_g^-$[87]. In this case, the low-energy excitations (meV range) correspond to lattice excitations such as acoustic vibrations (phonons) and libration of the molecules as a whole (librons), which are common to all diatomic molecular solids. In addition, there are magnetic excitations (magnons) that are not present in other molecular crystals[88]. These magnetic excitations are possible because of the triplet ($S = 1$) ground state of the oxygen molecule[86]. As a consequence, solid oxygen has both the properties of a molecular crystal and of a magnet.

Under equilibrium vapor pressure, oxygen can be condensed into a paramagnetic liquid phase in the temperature range 54.4 K$< T <$ 88 K[43]. It transforms upon subsequent cooling into three crystallographic modifications. The crystal in the first solid γ phase (43.8 K$< T <$54.4 K) is a rotator crystal and behaves as a paramagnet. Two orientationally ordered phases are known to exist in the temperature range 23.9 K$< T <$ 43.8 K (β oxygen) and below 23.9 K (α oxygen).

β oxygen has one molecule per primitive cell. The structure of intermediate β phase of solid oxygen was established by Hörl[89] in an electron-diffraction study. It was shown that β-O_2 has a rombohedral lattice of symmetry $R\bar{3}m$ with the same extremely simple orientational structure as α-O_2. This lattice can be seen as a distorted *fcc* structure obtained by packing dumbbell shaped molecules oriented along one of the spatial diagonals of the cube. The molecules are also orientationally ordered.

The lowest temperature phase of oxygen at atmospheric pressure is the solid α-O_2. It is stable below 23.9 K, has monoclinic structure (space group $C2/m$) and one molecule per primitive unit cell (Fig.5.2)[90] . The molecular axis is perpendicular to the a-b plane. These planes have center-rectangular symmetry and each molecule has four-nearest neighbors at 3.2Å, and two second-nearest neighbors, at 3.43Å. The third-nearest neighbors of each molecule, four in number and at an intermolecular separation of 4.19Å, are in adjacent planes. Monoclinic α-O_2 is the

only elemental solid that is known to be both electrically insulating and antiferro-

magnetic. It is known that all spins are aligned along the monoclinic axis $\pm\mathbf{b}$, with

all nearest neighbors in an antiparallel arrangement to each other. The presence of

antiferromagnetic long range order was inferred from the macroscopic magnetic

susceptibility in the lowest temperature phase[91].
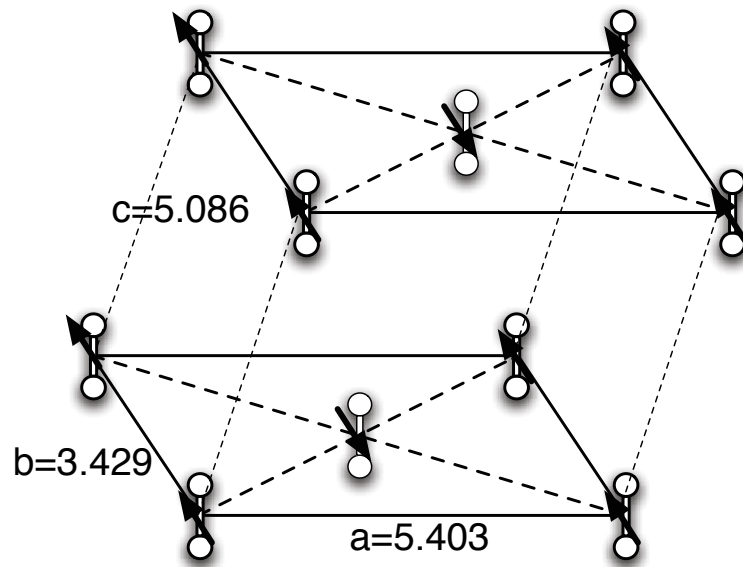
Figure 5.2: Crystal structure of solid α-oxygen molecules. All lattice constants are in Å[92].

5.3   Design

The ultra-cold neutron source system was designed to maintain up to 200 *c.c* of solid O_2 at about 8 K in a high cold neutron flux region. The UCN target cell is vacuum insulated and cooled by helium gas from a liquid helium flow cryostat with the capability of removing 1.5W of heat at 10K. The helium cooling liquid is passed through a transfer line.

Our experimental setup was designed to study the magnetic field influence on the UCN production rate in solid oxygen. For this purpose, the target cell assembly was installed inside the central bore of a superconducting magnet. Our setup is also designed to measure the effective mean free path of UCN in solid oxygen. Various depths of front cell *Al* windows were prepared for this purpose. The main design elements include the target cell assembly, the magnet system and the gas handling system.

Target Cell

The target cell is made of *Al* and has a cylindrical body with 3.3″ of OD and 2.85″ of ID. The front window is also made of *Al* and has 6/1000 ″ thickness. The volume of the oxygen cell can be varied by replacing the front window flange with various depths of recess. Five windows were prepared to investigate solid oxygen

with 1.475, 1.15, 0.825, 0.5 and 0″ of depths. The volume of the solid oxygen ranges

from 183 cm^3 to 30 cm^3 depending on the recess of the windows. The detailed

relationship among windows, cell volume and gas volume are listed in Table 5.1.

Flange Depth ($inch$)	Cell Volume (cm^3)	Gas Volume ($Liter$)	ΔP ($mbar$)
1.475	28.784	30.0	230
1.15	62.7237	65.5	500
0.825	96.6991	100.9	771
0.5	130.674	136.4	1042
0	182.944	190.9	1458

Table 5.1: The relative relationship of different cell volumes with different window depths and gas volumes. ΔP is the pressure difference on the 200 liter gas recovery tank when one condenses the oxygen gas at its vapor pressure (1.464 mbar at 54.6K). 1 atm=1013.18 mbar, 1 pascal=0.01 mbar. Inner-Diameter of the Cell (I.D)=2.85 inch.

There is one gas fill line connecting the cell to the gas handling system. Inside

the cryostat, the fill line is made from 1/8″ copper tubing. O_2 gas tends to freeze

in gas fill line while it is being cooled. To prevent a blockage of the gas return,

a 50 W *Nichrome* wire heater is tightly wound on the tubing along with a *Cernox*

temperature sensor mounted on the fill line.

In addition, a 0.5″ diameter rupture disk made of *Ni* with 25 μm thickness is

attached to the backside of the cell to satisfy safety concerns. The rupture disk

is set to consistently burst at 28 *psig*. The inner surface of the cold cell body is

coated with *Ni* so that the UCN generated in the solid oxygen can be bounced

back towards the thin front *Al* window. The thickness of the *Ni* layer is about 1

μm.

The target cell is covered with a long cylindrical cold shield made of *Al*. The

cold shield is connected to the first stage of the cryostat and provides a temperature

shielding layer to the target cell. The shield also works as a UCN guide and a

reflector. The UCN produced in the cell will be bounced back along the cold shield

(see Fig. 5.8 and Fig. 5.7). The backside of the target cell is mounted to a cold head

extension made of *Al*. Fig. 5.3(a) and 5.3(b) show the target cell assembly with a

gas fill line and a rupture disk.

Magnet System

A superconducting magnet provides some strength of magnetic fields to per-

turb the magnetic dispersion curves in the condensed system of oxygen. The in-

fluence of magnetic fields on the UCN production in solid oxygen will be studied

with the magnet system.

The oxygen target cell is placed inside the horizontal bore of the magnet. With

full current in the solenoid, the field strength in the center of the bore is about 5.5

Tesla. The chamber of the cryostat which houses the solenoid is made of steel, and

thus serves as the flux return. The solenoid is placed at the height of the beam
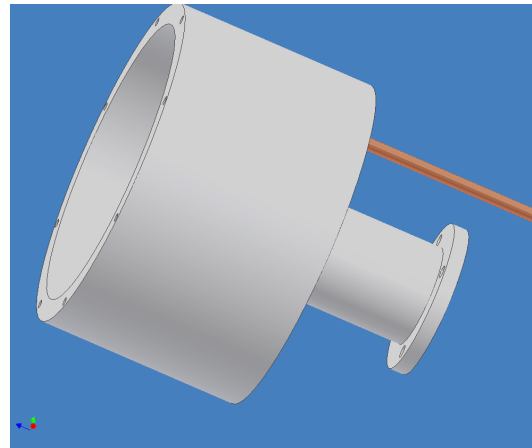
(a) Target Cell Side View
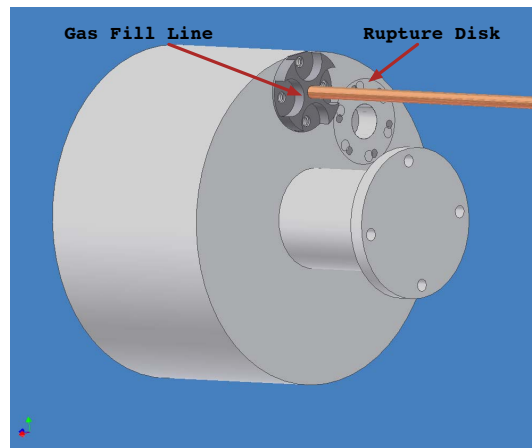
(b) Target Cell Rear View

Figure 5.3: A drawing of the solid oxygen target cell with gas fill line and rupture disk.

line, and is about 1.36 *m* from the floor. A cross-sectional view of the magnet is presented in Fig. 5.4.
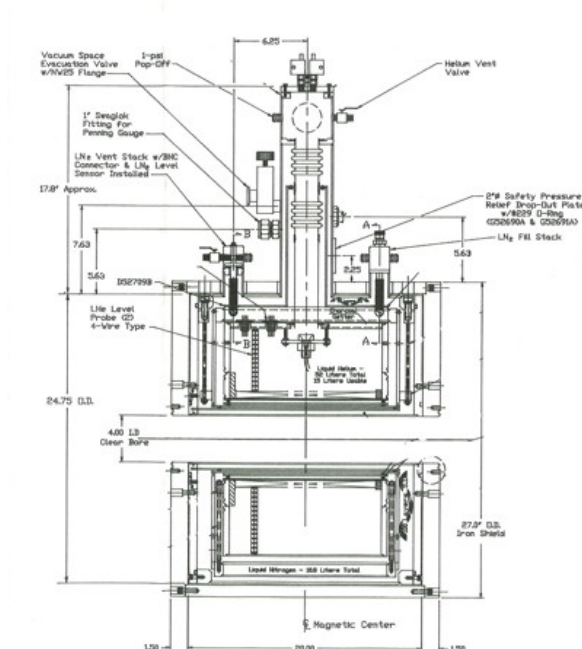
Figure 5.4: A cross section view of the superconducting solenoid magnet. The central warmbore has 4.25 ″ diameter.

This superconducting magnet has two cryogenic insulating volumes with liquid nitrogen and liquid helium. Liquid nitrogen is filled into the cold shield to reduce the radiation heat load into the liquid helium volume. For the initial cool down, liquid nitrogen is used to pre-cool the magnet. Liquid helium is filled from the top neck. It takes about 100 *l* of liquid helium in the initial fill, and 30 *l* for subsequent fill. Each fill would last approximately 24 hours. Level meters for both

liquid nitrogen and liquid helium are used to monitor the depletion of the cryogens.
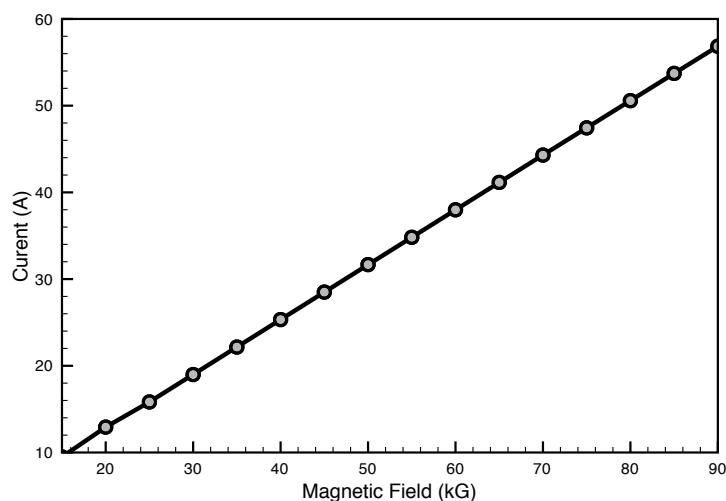
Figure 5.5: The field strength of the magnet as a function of applied current.

Once the magnet volume is filled with liquid helium, the solenoid can be energized. The rated operating current of power supply is 90A. A factory calibrated current to magnetic field relationship is presented in the Fig. 5.5

Oxygen Gas Handling System

The oxygen gas handling system provides preparation, filling, evacuation and storage of the oxygen gas. The whole system is constructed mainly with 1/4″ VCR stainless steel fittings and stainless steel tubings. A pressure relief valve is also

connected with different pressure settings. The schematics of the gas handling

system is shown in Fig. 5.6
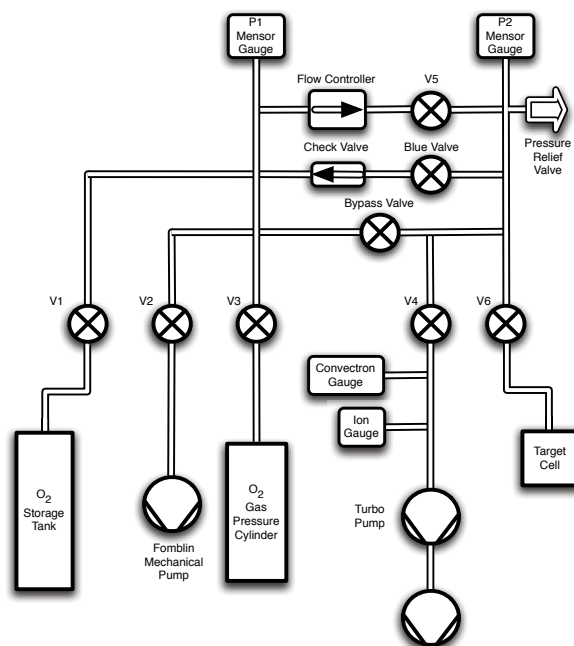
Figure 5.6: Gas handling system for the solid oxygen experiment for UCN production and crystal growth.

   The oxygen gas was recycled throughout the run. It requires about 150 l of STP

oxygen gas to condense to 183 cm^3 of solid oxygen. A 200 l stainless steel tank

assembly is attached through the *V1* valve to serve as gas storage. The storage

tank is pumped out and then filled by connecting the pressurized O_2 gas cylinder

to the gas system. During the filling of the cold cell, the bypass valve stays closed.

The oxygen is condensed in the target cell with variable flow rates. The flow rate

is controlled with the *flow controller*. The flow rate can be controlled from 0.5 *slm* (Standard Liter per Minute) to 0.05 *slm*. Two *Mensor* pressure gauges are placed upstream (*P1*) and downstream (*P2*) of the *flow controller*. There is a pressure relief valve connected downstream section of the gas handling system. The return path is through the check valve, which is set to open at 15 *psi*.
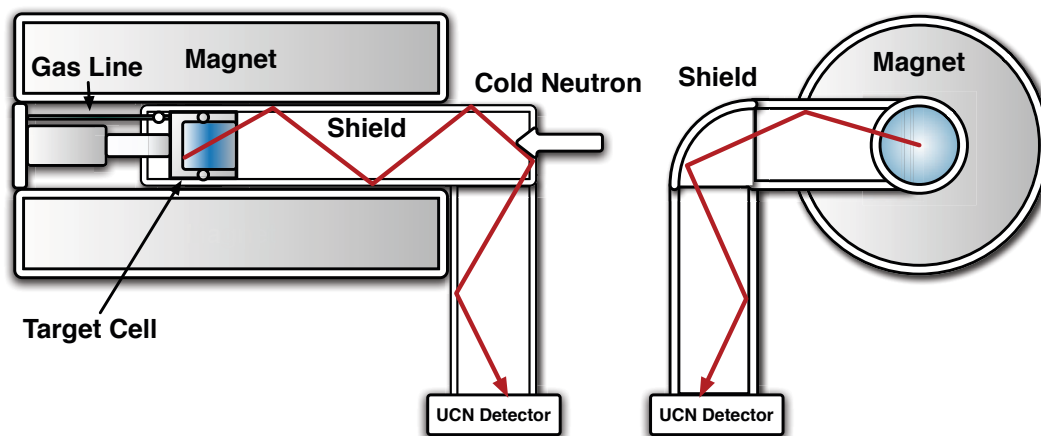
Figure 5.7: Side view and in-beam view of our experimental setup for UCN production with solid oxygen target cell. Incident cold neutron beam is illustrated as a thick arrow and outgoing UCNs are illustrated as a thin red arrow.

The system has two pumping ports, one connecting to a *Fomblin* filled mechanical pump, and another connecting to a dry turbo pumping station. The mechanical pump can be used to handle a high volume of oxygen gas. After the system is rough-pumped to below the range of the *Mensor* gauges, the turbo pump is used to further reduce the pressure of the system.
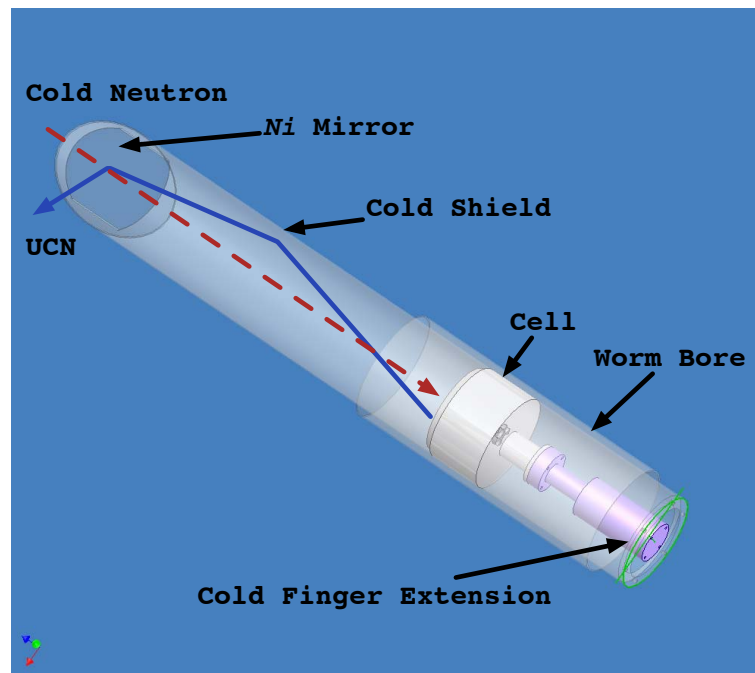
Figure 5.8: Solid oxygen target cell assembly in the bore of the magnet with target cell, cold shield, Ni mirror and cold finger extension. The incoming cold neutron beam is illustrated as a red dashed line and UCN is illustrated as a blue solid line. UCN produced in the cell are reflected back to the front of the cell and transported through the cold shield and reflected on the Ni mirror to the guide.

Setup Assembly

Fig. 5.7 shows the schematic of the experimental setup. The target cell and cold shield have to be installed inside the central bore of the magnet and aligned with incident cold neutrons. A UCN guide assembly is mounted sideways relative to the cold neutron flight path. Cold neutrons have to pass through two thin *Al* windows to reach the solid oxygen target. Some of the cold neutrons are down scattered to be UCNs. With *Ni* coated cell body, many of UCN produced in the cell can be reflected and transported back through front window and front cold shield. In that case, the mean path of UCN in the oxygen will be doubled. There is a ^{58}Ni thin foil with $45°$ angle with cold neutron incident direction at the front of guide tube to reflect UCNs to a detector side. Fig. 5.8 shows the detailed assembly in the bore including the cell, cold shield, ^{58}Ni mirror.

5.4 Operation

Gas Operation

First, the 200 l storage tank has to be filled with O_2 gas from the pressurized O_2 gas cylinder. During the filling of the gas storage tank, the bypass valve, *V1* valve, and flow controller valve are closed and the pressure of gas storage tank is

monitored by P_1 pressure gauge. Once the storage tank is filled with O_2 gas, *V3* valve is closed.

Before the cell is filled with oxygen gas, the cell has to be evacuated. The dry pump has to run to evacuate the line between *V4* valve and the pump while *V6* valve are closed. Once the pumping port is clear, *V4* valve is opened first to pump out residual gas inside the line. *V5* valve has to be opened to confirm pumping out all remaining gas between the *Flow Controller* and *V5* valve. Then, *V6* is opened slowly and the turbo molecular pump can start running at this stage. Once the cell is evacuated, *V4* valve, bypass valve are closed while *V6*, Blue valves stay opened.

The oxygen gas flows thorough the *flow controller* to the target cell. The pressure of the cell is monitored through the pressure gauge P_2. When oxygen is condensed in the target cell, the Blue valve and *V6* stay open. It ensures an open path for the oxygen gas to return to the storage tank, in case of accidental warm-up that turns the condensed oxygen into oxygen gas. The return path is through the check valve, which is set to open at 28 *psi*. There is a pressure relief valve connecting to the downstream of the gas handling system with 1500 *mbar* pressure setting.

Target Cell Operation

The target cell operation includes the temperature control of gas fill line and cell. The temperature control of the cell will be described in detail in the next section. The temperature of the gas fill line has to keep at a higher temperature than the melting point of solid oxygen while the oxygen gas is filled, condensed and frozen. A 50 W *Nichrome* wire heater tightly wound around the tubing is used to maintain a certain temperature of gas fill line with the feedback of a *Cernox* sensor mounted on the fill line.

The target cell is cooled by the cold head of a helium flow cryostat made of *Al*. Two *Cernox* sensors are mounted on the top and bottom of the cell to monitor the temperature gradient along the cell body. The temperature control range varies from 300 K down to 4 K. The temperature of the cell can be controlled with a 50 W heater mounted on the rear side of cold head. The ramping function in *Lakeshore 340* temperature controller can be programmed to cool down the cell and grow solid oxygen polycrystals with a temperature stability of mK.

Temperature Control

A *Lakeshore 340* cryogenic temperature controller provides temperature readings with a resolution of as low as 0.1 mK at 4.2 K. The specific temperature response curve for *Cernox* sensors are loaded in the control unit. The *Lakeshore 340* offers two proportional-integral-derviative (PID) control loops. A PID control algorithm calculates control output based on the temperature set-point and feedback from temperature sensor. Control output is generated by a high resolution digital-to-analog converter for a smooth continuous control. The PID value can be set manually. The PID value optimized for this experiment was 200 (P), 10 (I), and 5 (D) with our helium flow cryostat. This combination may vary with a different setup. The main heater output for this control unit is a well-regulated variable DC current source. The heater output can provide up to 100W of variable DC power to control loop 1.

The set-point ramp feature allows smooth, continuos changes in set-point. This feature permits faster experiment cycles, since data can be taken as the system is changing in temperature. It can also be used to make a more predictable approach to a set-point temperature. With this function, the unit can run a set of instrument instructions called an internal program. Each program represents the temperature changes needed to conduct an experiment. The set-point can be programmed with different ramping up or down rates.

With this function combined with regulating the helium flow rate, we could get a slow cooling rate and we can control the temperature of the cell with a rate of less than $1\mathrm{mK}/h$. The detailed control rate and method will be presented in section 5.5.

Magnet Operation

The operation procedure of a superconducting magnet is as follows. First, we have to fill the insulating volume with liquid nitrogen. While the liquid nitrogen is filled, the level of the nitrogen can be monitored in our control unit. Then liquid helium is filled from the top of the magnet neck. Once they are filled, we energize the super-conducting magnet solenoid. The following steps detail procedures of magnet current supply operations.

1. Check the previous current setting applied to the magnet. It is usually 0 A if we run a new magnet.

2. Match the magnet current by adjusting the current on the power supply located on bottom of rack.

3. Turn on the persistent heater by switching on the key.

4. Adjust or change the magnetic field by changing the current knob located on the top of rack to the desired value.

5. Power off the heater and record current on the sheet before switching off

heater.

6. Turn down the current to zero on current supply.

7. Turn off the current supply.

5.5   Solid Oxygen Crystal Growth

The tendency of micro-crystals to form in solid O_2 may limit the effectiveness of a large UCN source[93]. This required the investigation of the principal source of UCN loss in solid oxygen and the demonstration of super-thermal performance via its characteristic temperature dependence. While nuclear absorption and magnon up-scattering losses are theoretically well understood, this is not the case for the effects of polycystal formation and various lattice defects. The previous experience [94] with solid deuterium indicates that finite crystal effects do not introduce additional measurable scattering in this case.

However, this statement might not be applicable to solid oxygen because of its very different thermal properties. Since α-O_2 must be prepared by cooling γ-O_2 through two structural phase transitions, it produces considerable lattice contraction and strain. The phase transition from γ oxygen to β oxygen involves a large molar volume change in solid state. In the γ to β phase transition, the volume change (ΔV) is about $1.18 cm^3/mole$ and corresponding transition heat (ΔH)

is about $730J/mole$. In comparison, the volume change (ΔV) in β to α phase transition is about $0.05cm^3/mole$ and corresponding transition heat (ΔH) is about $92J/mole$[43].

This volume change and the corresponding emission of heat during the phase transition affect the formation of the polycrystalline and finally cause the development of holes and cracks along the grain boundaries. These defects in the solid system might trap the UCN produced in the solid and reduce the UCN extraction rate.
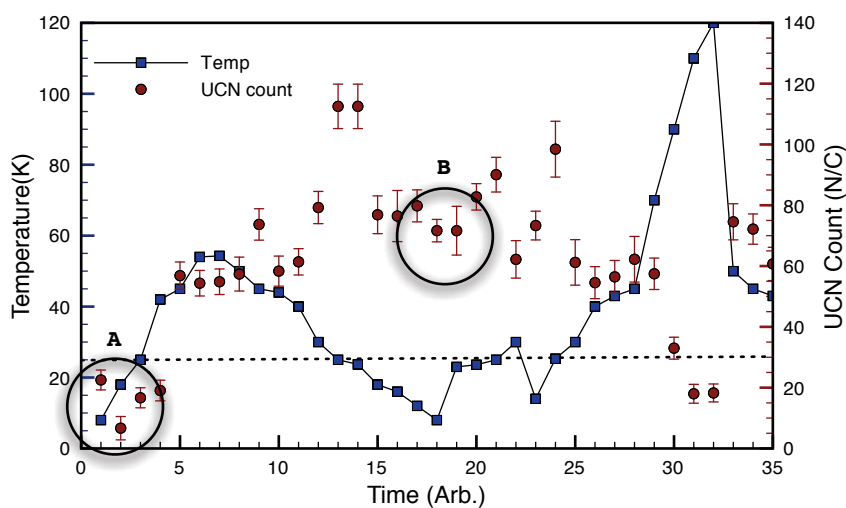
Figure 5.9: UCN production rate as a function of temperature and cooling time. The red filled circle is UCN production rate corresponding to right y-axis. The blue square with a line is the temperature of the cell corresponding to left y-axis. x-axis represents the evolution of cooling time with arbitrary unit.

We found a simple relationship between the condition of solid oxygen and the UCN production rate in our previous experiment at PSI, Switzerland. The experiment was carried out at the PSI spallation neutron source, SINQ, using the polarized cold neutron beam line for fundamental physics (FUNSPIN). The basic idea of this experiment was simply to introduce cold neutrons into a target cell and monitor the cold neutrons leaving the cell and also to detect UCNs produced from the cell. The target cell was mounted on a helium flow cryostat and filled with D_2, O_2 and CD_4. The temperature of the cell was controlled from 8 K to room temperature. We measured the UCN production of oxygen at various temperature from gas to solid with different cooling rates. As shown in Fig. 5.9, the UCN production rate at 8K with slow cooling rate (5.2K/h) in circle A was about 3 time higher than that with fast cooling rate (17K/h) in circle B. This indicated that the UCN production rate strongly depends on the transparency of the crystal. Therefore, the growth of polycrystalline samples with less cracks and holes is an important goal of our experiment.

In order to grow big polycrystalline samples with fewer defects, we followed the general principles of the single crystal growth procedure from Brodyanski *et al.*[95] and adapted these for our demands. They had successfully grown single oxygen crystal of 1 *cm* in diameter and 2.05 *cm* in thickness. We used oxygen gas with purity of 99.999%.
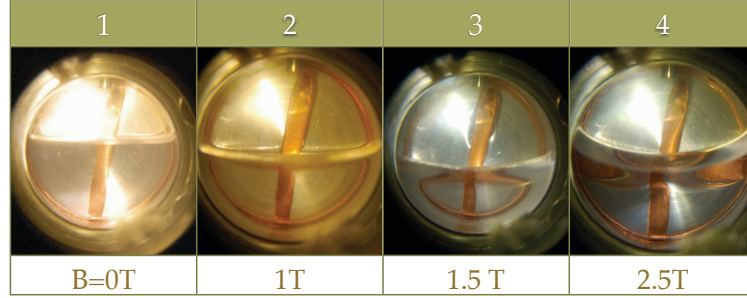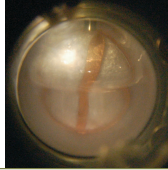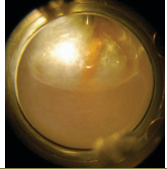
Figure 5.10: Liquid oxygen at $T = 54.6$ K under different magnetic fields from $B = 0$ T to $B = 2$ T.
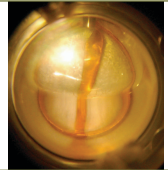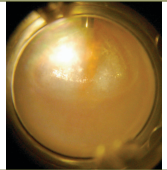
The procedure is as follows. At first, the cell was evacuated up to 10^{-6} *mbar* at room temperature. After that, the empty cell was cooled down to a temperature a bit lower than the boiling point of oxygen. After condensation, the liquid oxygen was cooled down 3 K/h towards the melting point slowly 0.1 K/h to grow the crystal. Around the crystallization point, the crystal was annealed for $3 \sim 5h$.

The averaged cooling rate within the temperature region of high-temperature phases in solid was about $0.5 \sim 1$ K/h. In the temperature range of a solid-solid phase transition, the sample was cooled with a more slow rate of 0.05 K/h. Later, we annealed the crystal during a low-temperature phase transition for $10 \sim 12h$ by keeping the sample at a constant temperature (43.6 K). After the phase transformation is completed, we applied very slow 0.02 K/h cooling to prevent stresses developing in the crystal.
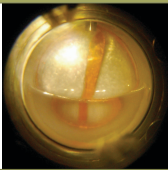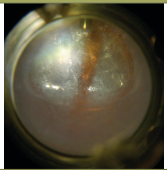
We also applied various magnetic fields up to $2T$ while we were growing a poly

(a) B=0T

(b) B=1T

(c) B=1.5T

(d) B=2T

Figure 5.11: Solid oxygen under different magnetic fields shows different crystallographic structure.

crystal from liquid oxygen. To check the transparency of the crystal, a copper bar with spiral ring has been inserted inner cell body. The cell has been filled to about the half of the volume to compare the transparency of solid with empty space. The front window was made of Mylar, biaxially-oriented polyethylene terephthalate (boPET) polyester film, with indium thin layer of vacuum seal. Mylar is used for its high tensile strength, good chemical and dimensional stability and transparency. The detailed comparison of crystal growth under different magnetic fields shown in Fig. 5.10 and 5.11. Fig. 5.10 shows liquid oxygen at $T = 54.6$ K under magnetic fields. Since it is magnetic with a large molar moment, liquid oxygen climbs up along the side wall under high magnetic fields. In all cases, the liquids look transparent.

The four tables show a change in the transparency of crystal around γ-β phase transition temperature $T_{\gamma-\beta}$ under different magnetic fields. Fig. 5.11(a) shows the change under zero magnetic field. When the temperature of the cell reaches $T_{cell} \sim 44.47$K, the temperature was set. About two hours later, there was a sudden temperature drop to $T_{cell} \sim 44.21$K and the transparency of the cell worsened. Under $B = 1$T in Fig. 5.11(b) and 2T in Fig. 5.11(d), the same phenomenon was observed after $3h$ and $4h$ and in these cases, the transparencies were still bad. Under $B = 1.5$T in Fig. 5.11(c), however, it took longer time ($t \sim 6h$) than other conditions and the transparency of the cell was also improved. The temperature change was

from $T \sim 44.56$K to $T \sim 44.23$K. Therefore, we could see a certain dependence of poly crystal of oxygen on magnetic field strength.

5.6   Preliminary Experiment on UCN Production in Solid Oxygen

The experiment of UCN production is strongly correlated with the intensity of incident cold neutron flux, low background rate and the temperature control of target cell. First, the incident neutron beam should be as intense as possible because the UCN production rate per incident cold neutron is very small. For example, the production rate in solid D_2 is $1.95 \times 10^{-8} \Phi_0$ and the calculated production rate from solid α-O_8 is $3.5 \times 10^{-8} \Phi_0$, where Φ_0 is cold neutron flux as shown in Fig. 5.12[82].

Second, the background noise rate in the experiment has to be kept low enough to discriminate the UCN count rate from the noise. The background noise usually comes from leakage radiation from cold neutron beam. Some noise comes from neighboring experiments and fast neutrons scattered from unphased chopper or guide tube. During our experiment at FP-12 of LANSCE, we suffered from a high background noise rate.

We applied a time-of-flight (TOF) method to discriminate the UCN count rate
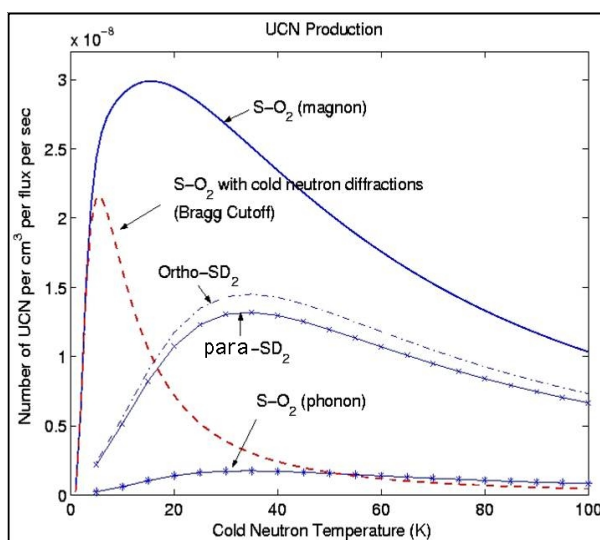
Figure 5.12: UCN production density as a function of incident cold neutron temperature. A Maxwell distribution of the cold neutron spectrum was assumed. UCN production density in solid oxygen using magnon interaction shows a maximum value with 12K spectrum temperature of incident cold neutrons. At the same time, the maximum production density in solid deuterium is with 30K incident cold neutron spectrum[82].

from the high background rate, and reflecting the UCN by Ni plated mirror inserted in front shielding tube further reduced the background rate. A multi-channel scaler (MCS) was used for collecting counting rate. MCS records the counting rate of events as a function of time. When a scan is started, the MCS begins counting input events in the first channel of its memory. At the end of the preselected dwell time, the MCS advances to the next channel to count the events. This dwell is repeated until MCS scan all of channel in the memory. MCS has two methods of synchronizing the scans with starting of the events. Either the start of a scan in the MCS can provide either internal trigger mode or external trigger mode. In the external trigger mode, a positive TTL logic signal can initiate the scan in the MCS.

We first tried the internal trigger mode to get the UCN count rate. However, a high background rate, which mainly comes from fast and cold neutrons or γ-ray, was seen in all of the channels so that it was not possible to discriminate the UCN count rate from the background rate. Using external trigger mode, we determined that this high back ground rate were counted mainly before $5\,ms$. The proton beam was operated at $20Hz$ frequency. Therefore, we set the channel width to $0.1ms$ and one set of scanning time as $50ms$ with external triggering mode. The total pass length for each run was 20,000 times so that total scanning time was 1000 s.

The results obtained on the solid oxygen, with these methods, is shown in Fig. 5.13. The initial cold neutron background is attenuate by $5 \sim 6ms$ after initial
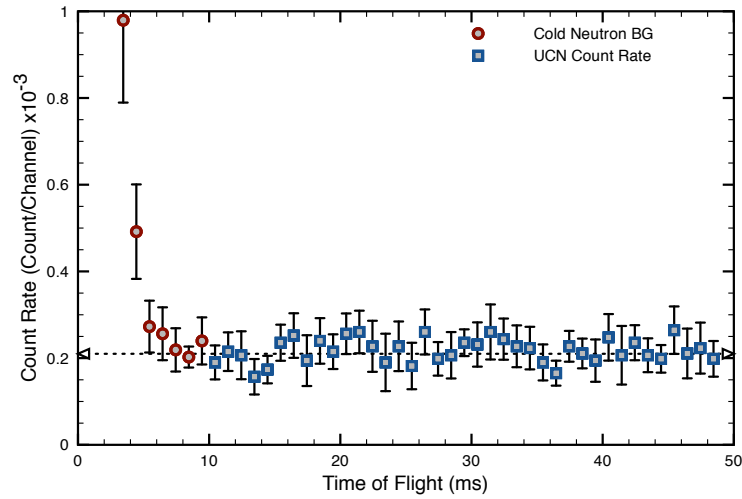
Figure 5.13: UCN count rate before subtracting background rate. The dotted line across 0.21 represents the averaged background rate. The cold neutron background rate is denoted as a red circle. x axis denotes the time-of-flight and y axis represents the count rate with counter per channel unit.

proton pulse is triggered. We considered the count rate at initial $10ms$ as cold neutron background. This is a sufficiently long enough time to discriminate the UCN count rate from the initial cold neutron background. And the count rates in the range of $49.1ms \sim 50ms$ channels were also considered as a background since this count rate might be dominated by next proton pulse. Therefore, the only channels we considered for the UCN counts were from the $10.1ms$ to $49ms$. The constant background rate is given as about $(8.4 \pm 0.4) \times 10^{-3} n/s$, which is still very high. The average count rate throughout the run before background subtracted is about $(8.487 \pm 0.3) \times 10^{-3} n/s$. The net count rate after subtracting background rate is $(0.087 \pm 0.5) \times 10^{-3} n/s$. This is the averaged result through the 242 runs and the background rate was averaged over 25 runs with empty cell. We couldn't see any temperature dependence of the count rate due to the high background rate.

6

Summary

In this thesis, we have investigated neutron phase space cooling in condensed matter media, from the cold neutron regime to ultra-cold regime, using both theoretical and experimental approaches. The first part of this work dealt with the neutron scattering in the cold neutron regime. We performed theoretical studies of the neutron scattering cross section model of solid methane in phase II. Based on the model, we evaluated the scattering function $S(Q, \omega)$, the frequency spectrum $\rho(\omega)$ and the total scattering cross section for solid methane at 20 K, 4 K, and 0 K. The model also implicitly uses experimental input from neutron scattering, light scattering and thermodynamic measurements which determine the energy spectra and other properties for the different modes in solid methane. The total scattering cross sections are shown to be consistently explained by our model. Moreover, the relative contributions of the free and hindered rotational modes in the scattering

function, frequency spectrum and scattering cross section have also been estimated using our model.

We also measured the neutron brightness from the solid methane moderator of the LENS neutron source with the moderator operated in phase II at 20 K and 4 K. We compared the measured spectra with MCNP simulations of the Target-Moderator-Reflector (TMR) system in the same geometry as used in the measurement, using as the source for our cold neutron scattering kernel our new neutron scattering model of solid methane in phase II. We added O_2 to the solid methane to ensure spin temperature equilibrium, and we slowly cooled and thermally cycled the methane in an attempt to minimize possible cracks and holes in the solid methane. The prediction of the simulations with the newly-developed scattering kernel are in good agreement with experiments at both temperatures. The neutron energy spectrum at 4 K shows a colder and brighter spectrum than the 20 K one. This observation encourages us to continue investigations into other moderator media and geometries in order to further increase the cold neutron brightness and to further cool the neutron spectrum.

We investigated the optimal thickness of our moderator of different temperatures with our kernels and discovered that further increases in brightness are possible. We plan to continue further brightness measurements from solid methane under different conditions in the future.

We have extended our theoretical work of neutron moderation to the very cold energy regime. We have shown the separate contributions of collective modes in solid methane to neutron moderation and calculated the effective neutron spectrum temperature at 4K from the different collective modes in LENS TMR geometry. The free only rotation mode in solid methane shows the lowest neutron spectrum temperature. We inferred from this result that methane clathrate can be a good moderating medium for very cold neutron production. Methane clathrate is now the first known example of a material which, as we have shown, has the potential to produce a bright neutron spectrum in the VCN energy regime. This result supplies encouragement for the continued investigation of other moderator media which may demonstrate higher brightness and lower spectral temperatures. We will improve our calculation by including D_2O scattering cross section at low temperature.

The second part was the study of solid oxygen as an ultra-cold neutron moderating medium. We have presented an experimental setup for the study of crystal growth in solid oxygen and for its use as a UCN converter utilizing the magnetic properties of solid oxygen. The setup included a cryostat with a target cell for the neutron scattering experiment, oxygen gas handling system, magnet system and an optical monitoring system for oxygen crystal growth.

We also tested solid oxygen as a new type of UCN converter at FP-12 of LAN-SCE. The UCN count rate was about $(0.087 \pm 0.5) \times 10^{-3} n/s$. During the experiment, there was high background noise in the experimental area which mainly came from the leakage of cold neutrons. We applied a time-of-flight method to try to discriminate UCN count rate from the background rate.

For the temperature control of the converter cell, we couldn't cool the cell below 15K due to low cooling efficiency after the cold shield being assembled. From the preliminary calculation of UCN production[82], the cell should be cooled down below 8K to see the magnon interaction with neutrons. There was also certain cold neutron flux reduction during our experiment and we need to understand this. We plan to conduct another UCN production experiment at LANSCE in the near future.

Bibliography

[1] R. Pynn. Neutron Scattering-A Primer. *Los Alamos Science*, 19:1, 1990.

[2] P. A. Egelstaff. Solid and Liquid State Research with Cold Neutron. *British Journal of Applied Physics*, 10:1–9, 1959.

[3] P. A. Egelstaff and P. Schofiled. On the Evolution of the Thermal Neutron Scattering Law. *Nuclear Science and Engineering*, 12:260–270, 1962.

[4] P. A. Egelstaff. *An Introduction to the Liquid State*. Oxford University Press, 1994.

[5] T. Chatterji. *Neutron Scattering from Magnetic Materials*. Elsevier, 2006.

[6] D. Dubbers. Particle Physics with Cold Neutrons. *Progress in Particle and Nuclear Physics*, 26:173–252, 1991.

[7] I. B. Khriplovich and S. K. Lamoreaux. *Cp Violation Without Strangeness*. Springer, 1997.

[8] J. S. Nico and W. M. Snow. Fundamental Neutron Physics. *Annual Review of Nuclear and Particle Science*, 55:27–69, December 2005.

[9] P. A. Egelstaff. The Scattering of Thermal Neutrons by Moderators. *Nuclear Science and Engineering*, 12:250, 1962.

[10] P. A. Egelstaff. *Thermal Neutron Scattering*. Academic Press, 1965.

[11] M. Utsuro. Simple Relations for Effective Neutron Temperature in Cold Moderators with Lattice Vibrational Modes. *Journal of Nuclear Science and Technology*, 10(7):428–434, 1973.

[12] J. J. Duderstadt and L. J. Hamilton. *Nuclear Reactor Analysis*. Wiley, 1976.

[13] B. Davison. *Neutron Transport Theory*. Oxford University Press, 1957.

[14] A. Foderaro. *The Elements of Neutron Interaction Theory*. The MIT Press, 1971.

[15] D. E. Parks. *Slow Neutron Scattering and Thermalization, with Reactor Applications*. Benjamin, W. A., 1970.

[16] E. Fermi. On the motion of neutrons in hydrogeneous substances. *Ricerca Scientifica VII*, 2:13, 1936.

[17] R. Golub, D. Richardson, and S. Lamoreaux. *Ultra-Cold Neutrons*. Institute of Physics Publishing, 1991.

[18] E. P. Wigner and J. E. Wilkins Jr. Effect of the Temperature of the Moderator on the Velocity Distribution of Neutron with Numerical Calculation for H as Moderator. Technical report, Oak Ridge National Laboratory, 1944.

[19] A. W. McReynolds, A. L. Wittemore, A. K. Horn, and A. Kier. Differential Neutron Thermalization. Technical Report GA-2503, General Atomic, 1960.

[20] J. J. Rush, D. W. Connar, and R. S. Carter. Study of D_2O Ice as a Cold Neutron Source. *Nuclear Science and Engineering*, 25(4):383, 1966.

[21] J. U. Koppel. Mean Emission Time Correction for the Measurement of Stationary Spectra by the Pulsed Neutron Source Technique. Technical Report GAMD-4131, General Atomic Division, General Dynamics Coporation, 1963.

[22] K. Inoue, Y. Kiyanagi, and H. Iwasa. An accelerator-based cold neutron source. *Nuclear Instruments and Methods*, 192:129–136, 1982.

[23] N. Watanabe. Neutronics of pulsed spallation neutron sources. *Reports of Progress in Physics*, 66:339, 2003.

[24] B. D. Bartolo and J. Danko, editors. *Collective Excitations in Solids*. Springer, 1983.

[25] M. T. Dove. *Structure and Dynamics*. Oxford University Press, 2003.

[26] I. I. Gurevich and L. T. Tarasov. *Low Energy Neutron Physics*. North-Holland Publishing Co, 1968.

[27] W. Greiner, L. Neise, H. Stöcker, and D. Rischke. *Thermodynamics and Statistical Mechanics*. Springer, 2001.

[28] A. I. Akhiezer, V. G. Bar'yakhtar, and M. I. Kaganov. Spin Waves in Ferromagnets and Antiferromagnets. II. *Soviet Physics Uspekhi*, 3(5):661–676, 1961.

[29] A. J. Nijman and A. J. Berlinsky. Theory of Nuclear Spin Conversion in the β Phase of Solid Methane. *Physical Review Letters*, 38:408–411, 1977.

[30] K. J. Lushington and J. A. Morrison. Neutron Scattering and Proton Spin Conversion in Solid CH_4. *Canadian Journal of Physics*, 55:1580, 1977.

[31] Y. Ozaki, Y. Kataoka, and T. Yamamoto. Theory of phase transitions in solid methanes. XIII. The differential neutron scattering cross section in phase II of solid CH_4. *Journal of Chemical Physics*, 73:3442–3451, 1980.

[32] Y. Ozaki, Y. Kataoka, K. Okada, and T. Yamamoto. Theory of phase transitions in solid methanes. XIV. The total neutron scattering cross section in phase II of solid CH_4. *Canadian Journal of Physics*, 59:275, 1981.

[33] S. Grieger, H. Friedrich, K. Guckelsberger, R. Scherm, and W. Press. The total neutron scattering cross section of solid methane in phase II. *Journal of Chemical Physics*, 109:3161–3175, August 1998.

[34] Y. D. Harker and R. M. Brugger. Investigation of the Low-Temperature Phase Transition in Solid Methane by Slow Neutron Inelastic Scattering. *Journal of Chemical Physics*, 46:2201–2208, March 1967.

[35] W. Press. *Single-Particle Rotations in Molecular Crystals*. Berlin Springer Verlag, 1981.

[36] H. Conrad. In G. Mank and H. Conrad, editors, *16th Meeting of the International Collaboration on Advanced Neutron Sources*, page 39, 2003.

[37] M. Nelkin. Scattering of Slow Neutrons by Water. *Physical Review*, 119:741–746, July 1960.

[38] M. Utsuro. Simple Expression for Effective Neutron Temperature due to Rotational Motions of Cold Moderators Molecules. *Journal of Nuclear Science and Technology*, 11:434–444, 1974.

[39] A. Hüller and D. M. Kroll. Rotational tunneling in solids. *Journal of Chemical Physics*, 63:4495–4504, November 1975.

[40] A. Hüller. Rotational tunneling in solids: The theory of neutron scattering. *Physical Review B*, 16:1844–1857, September 1977.

[41] J. R. Granada. Synthetic scattering kernel to describe the interaction of slow neutrons with solid methane in phase II. *Nuclear Instruments and Methods in Physics Research B*, 266:164–172, 2007.

[42] T. Yamamoto, Y. Kataoka, and K. Okada. Theory of phase transitions in solid methanes. X. Centering around phase II in solid CH_4. *Journal of Chemical Physics*, 66:2701–2730, March 1977.

[43] V. G. Manzhelii and A. I. Prokhavatilov. *Structure and Thermodynamic Properties of Cryocrystals*. Begell House Inc, 1998.

[44] Strictly speaking the point symmetry of the high-symmetry sites is O, but the crystal field at these sites has symmetry O_h.

[45] H. M. James and T. A. Keenan. Theory of Phase Transitions in Solid Heavy Methane. *Journal of Chemical Physics*, 31:12–41, July 1959.

[46] W. Press. Structure and Phase Transitions of Solid Heavy Methane CD_4. *Journal of Chemical Physics*, 56:2597–2609, March 1972.

[47] M. A. Caprio. LevelScheme: A level scheme drawing and scientific figure preparation system for Mathematica. *Computer Physics Communications*, 171:107, 2005.

[48] M. Prager and A. Heidemann. Rotational Tunneling and Neutron Spectroscopy: A Compilation. *Chem. Rev.*, 97(8):2933, 1997.

[49] M. Prager, W. Press, B. Asmussen, and J. Combet. Phase III of methane: Crystal structure and rotational tunneling. *Journal of Chemical Physics*, 117:5821–5826, September 2002.

[50] H. Friedrich, S. Grieger, K. Guckelsberger, R. Scherm, and W. Press. Measurement of total cross-section and spin conversion in solid methane. *Physica B Condensed Matter*, 226:218–220, February 1996.

[51] W. Press and A. Kollmai. CH_4: Tunneling States, Rotations, and Phase Transition in a Quantum Molecular Crystal. *Solid State Communications*, 17(4):405–408, 1975.

[52] W. Press, J. A. Morrison, and K. Neumaier. Rotational Exciations of A-CH_4 in the meV range studied by Inelastic Neutron Scattering. *Canadian Journal of Physics*, 66:686–691, 1988.

[53] S. W. Lovesey. *Theory of Neutron Scattering from Condensed Matter*. Number 72

in International Series of Monographs on Physics. Oxford University Press, 1984.

[54] A. M. Messiah. Scattering of Slow Neutrons by H_2 and CH_4. *Physical Review*, 84:204–214, October 1951.

[55] P. A. Egelstaff, S. J. Cocking, and R. Royston. Thermal Neutron Scattering Law for Light and Heavy Water. In *Proceedings of Symposium on Inelastic Scattering of Neutrons in Solids and Liquids*, page 309. International Atomic Energy Agency, 1961.

[56] P. A. Egelstaff. *Experimental Neutron Thermalisation, (International Series of Monographs in Nuclear Energy)*. Pergamon Press, 1967.

[57] B. Y. Gorodilov, V. V. Sumarokov, P. Stachowiak, and A. Jeżowski. Heat transfer in solid CH_4: Influence of an atomic impurity (Kr). *Physical Review B*, 58:3089–3093, August 1998.

[58] M. Prager, B. Asmussen, W. Press, H. Blank, and C. J. Carlile. Rotational spectra and the phase diagram of CH_4/Ar mixtures. *The Journal of Chemical Physics*, 95(1):569–575, 1991.

[59] Y. Shin, W. M. Snow, C. Y. Liu, C. M. Lavelle, and D. V. Baxter. A Microscpoic Model for the Neutron Dynamic Structure Factor of Solid Methane in phase II. *preprint*, arXiv:0705.08241v3, 2007.

[60] M. B. Leuschner, D. V. Baxter, J. M. Carmeron, J. Derenchuk, C. M. Lavelle, A. Lone, H. Nann, T. Rinkel, and W. M. Snow. LENS: A New Pulsed Neutron Source for Research and Education. *Journal of Research of National Institute of Standards and Technology*, 110(3):153155, 2005.

[61] Y. Wen and L. Jiu-Qing. Neutronics studies of solid targets for spallation neutron source using Monte Carlo simulation. *Chinese Physics*, 12:599–603, June 2003.

[62] J. M. Carpenter, T. L. Scott, and M. E. Miller. The Develpment of Solid Methane Neutron Moderators at Intense Pulsed Neutron Source Facility of Argonne National Laboratory. ANL/IPNS/CP-98533, Argonne National Laboratory, 1999.

[63] E. P. Shabalin, V. V. Golikov, E. N. Kulagin, S. A. Kulikov, and V. V. Melikov. Study of Fast Neutron Radiation Effect in Cold Moderator Materials. *Particle and Nulcei Letters*, 114(5):82, 2002.

[64] K. Inoue. Slowing down of Neutrons to Very Low Temperature by Cold Solid Hydrogenous Moderators. *Journal of Nuclear Science and Technology*, 7(11):580–587, 1970.

[65] J. M. Carpenter. Thermally Activated Release of Stored Chemical Energy in Cryogenic Media. *Nature*, 330(6146):358–360, Nov 1987.

[66] B. Asmussen, M. Prager, W. Press, H. Blank, and C. J. Carlile. Rotational motions of CH_4 molecules in weak orientational potentials of cubic symmetry. *Journal of Chemical Physics*, 97:1332–1342, July 1992.

[67] R. F. Curl, Jr., J. V. V. Kasper, and K. S. Pitzer. Nuclear Spin State Equilibration through Nonmagnetic Collisions. *Journal of Chemical Physics*, 46:3220–3228, April 1967.

[68] J. J. Kim and K. S. Pitzer. Crystal field effects on oxygen in solid methane and the catalysis of spin-species conversion of methane. *Journal of Chemical Physics*, 66:2400–2407, March 1977.

[69] C. M. Lavelle, D. V. Baxter, A. Bogdanov, V. P. Derenchuk, H. Kaiser, M. B. Leuschner, M. A. Lone, W. Lozowski, H. Nann, B. V. Przewoski, N. Remmes, T. Rinckel, Y. Shin, W. M. Snow, and P. E. Sokol. Neutronic design and measured performance of the Low Energy Neutron Source (LENS) target moderator reflector assembly. *Nuclear Instruments and Methods in Physics Research A*, 587:324–341, March 2008.

[70] H. F. Nieman, D. C. Tennant, and G. Dolling. Single crystal filters for neutron spectrometry. *Review of Scientific Instruments*, 51:1299–1303, October 1980.

[71] G. F. Knoll. *Radiation Detection and Measurement*. John Wiley & Sons, 2nd edition, 1989.

[72] I. L. Fowler and P. R. Tunnicliffe. Boron Trifluoride Proportional Counters. *Review of Scientific Instruments*, 21(8):734, 1950.

[73] B. J. Micklich and J. M. Carpenter, editors. *Proceedings of the Workshop on Applications of a Very Cold Neutron Source*. Argonne National Laboratory, 2005.

[74] J. S. Tse, C. I. Ratcliffe, B. M. Powell, V. F. Sears, and Y. P. Handa. Rotational and Translational Motions of Trapped Methane. Incoherent Inelastic Neutron Scattering of Methane Hydrate. *Journal of Physical Chemistry A*, 101(25):4491, 1997.

[75] T. Kamiyama, Y. Kiyanagi, T. Horikawa, H. Iwasa, T. Uchida, T. Ebinuma, H. Narita, and S. M. Bennington. Dynamical features of methane hydrate around 12K. *Physica B Condensed Matter*, 350:e395, 2004.

[76] M. Prager and W. Press. Methane clathrate: CH_4 quantum rotor state dependent rattling potential. *The Journal of Chemical Physics*, 125(21):214703, 2006.

[77] C. Gutt, W. Press, A. Hüller, and J. S. Tse. Rotational dynamics in methane hydrate. *Applied Physics A: Materials Science & Processing*, 74(0):s1299, 2002.

[78] T. Kamiyama, N. Seki, H. Iwasa, T. Uchida, T. Ebinuma, H. Narita, N. Igawa, Y. Ishii, S. M. Bennington, and Y. Kiyanagi. Methane molecular motion in clathrate hydrate host framework. *Physica B Condensed Matter*, 385:202, 2006.

[79] H. Conrad, W. F. Kuhs, K. Nünighoff, C. Pohl, M. Prager, and W. Schweika. Inelastic scattering and spectral measurements of advanced cold moderator media. *Physica B: Condensed Matter*, 350(1-3, Supplement 1):E647, 2004.

[80] C. Gutt, B. Asmussen, W. Press, C. Merkl, H. Casalta, J. Greinert, G. Bohrmann, J. S. Tse, and A. Hüller. Quantum rotations in natural methane-clathrates from the Pacific sea-floor. *EPL (Europhysics Letters)*, 48(3):269, 1999.

[81] M. Utsuro and N. Morishima. Total Neutron Cross Section in Heavy Ice at 77 and 15K for Neutron Energies between 0.3 and 100 meV. *Journal of Nuclear Science and Technology*, 18(739), 1981.

[82] C. Y. Liu and A. R. Young. Ultra-Cold Neutron Production in Anti-ferromagnetic Oxygen Solid. *Preprint nucl-th 0406004*, April 2004.

[83] A. Steyerl. A "Neutron Turbine" as an Efficient Source of Ultracold Neutrons. *Nuclear Instruments and Methods*, 125(3):461–469, 1975.

[84] R. Golub and J. M. Pendlebury. Super-thermal Sources of Ultra-cold Neutrons. *Physics Letters A*, 53:133–135, June 1975.

[85] Yu. A. Freiman and H. J. Jodl. Solid oxygen. *Physics Reports*, 401(1-4):1, 2004.

[86] A. J. R. da Silva and L. M. Falicov. Many-body calculation of the magnetic,

optical, and charge-transfer spectra of solid oxygen in the α and β phases. *Physical Review B*, 52:2325–2335, July 1995.

[87] E. J. Wachtel and R. G. Wheeler. Antiferromagnetic Solid Oxygen. *Journal of Applied Physics*, 42:1581–1587, March 1971.

[88] E. J. Wachtel and R. G. Wheeler. Magnon Spectrum of Alpha Oxygen. *Physical Review Letters*, 24:233–236, February 1970.

[89] E. M. Hörl. Structure and Structure Imperfections of Solid β-Oxygen. *Acta Crystallographica*, 15(9):845, 1962.

[90] A. P. J. Jansen and A. van der Avoird. Magnetic coupling and dynamics in solid α and β-O_2. II. Prediction of magnetic field effects. *Journal of Chemical Physics*, 86:3597–3601, March 1987.

[91] A. de Bernabé, G. J. Cuello, F. J. Bermejo, F. R. Trouw, and A. P. J. Jansen. Vibrational dynamics in solid α-oxygen: Experimental assessment of spin-phonon couplings. *Physical Review B*, 58:14442–14451, December 1998.

[92] Yu. A Freiman and H. J Jodi. Elementary excitations in solid oxygen. *Low Temperature Physics*, 28(7):491, 2002.

[93] W. F. Giauque and H. L. Johnston. An isotope of oxygen, mass 18. *Nature*, 123:318, 1929.

[94] C. L. Morris, J. M. Anaya, T. J. Bowles, B. W. Filippone, P. Geltenbort, R. E. Hill, M. Hino, S. Hoedl, G. E. Hogan, T. M. Ito, T. Kawai, K. Kirch, S. K. Lamoreaux, C.-Y. Liu, M. Makela, L. J. Marek, J. W. Martin, R. N. Mortensen, A. Pichlmaier, A. Saunders, S. J. Seestrom, D. Smith, W. Teasdale, B. Tipton, M. Utsuro, A. R. Young, and J. Yuan. Measurements of Ultracold-Neutron Lifetimes in Solid Deuterium. *Physical Review Letters*, 89(26):A262501–1, 2002.

[95] A. P. Brodyanski, S. A. Medvedev, M. Vetter, J. Kreutz, and H. J. Jodl. Nature of infrared-active phonon sidebands to internal vibrations: Spectroscopic studies of solid oxygen and nitrogen. *Physical Review B*, 66(10):104301–1, September 2002.

Yunchang Shin

Department of Physics
2401 Milo B. Sampson Ln.
Cyclotron Facility
Indiana University
Bloomington, IN 47408

Phone: (812) 855-1435
Fax: (812) 855-6645
yunshin@indiana.edu
http://mypage.iu.edu/~yunshin/

Citizenship

Republic of Korea (South Korea)

Education

Ph.D. Physics, Indiana University, 2008 (Expected)

M.A. Physics, Yonsei University, Seoul, South Korea, 1999

B.S. Physics, Suwon University, Suwon, South Korea, 1997

Research Experience

Research Assistant   1996
Jong-Gul Yun   Suwon University
Development of method of ferroelectric thin film deposition onto SiO_2 layer. X-ray diffraction study of thin film.

Research Assistant   1997~1999
Il-Tong Cheoun   Yonsei Univeristy
Investigation of effective chiral lagrangian for pion interaction with vector and axial vector mesons. Development of updating methods for photon production in heavy ion collision.

Research Assistant   2003~Present
W. Mike Snow and Chen-Yu Liu   Indiana University
Structural estimation of neutron moderation in solid methane including scattering model development. Development of scattering kernels of solid methane for MCNP at temperatures below 20K. Participation in design of solid methane moderator and its gas handling system of LENS. Operating the moderator with O_2 doping and slow cooling. The neutron spectrum measurement and data analysis of LENS neutron source. Study of ultra-cold neutron production in solid oxygen using its magnetic degree of freedom. Run an experiment at PSI on UCN production with solid D_2, CD_4 and O_2. Working on solid O_2 crystals growth and UCN production in solid O_2 under low temperatures and high B field.

Teaching Experience

Teaching Assistant, General Physics, Yonsei University, Fall 1998

Teaching Assistant, Nuclear Physics, Yonsei University, Spring 1999

Teaching Assistant, Physics 101, Indiana University, Spring 2004

Employment

Cyclotron Application Lab, Korea Cancer Center   Seoul, Korea
Hospital
Assistant Scientist   1999~2001
Development of negative ion source for 13MeV medical purpose cyclotron. Design, Simulation and Beam extraction test in prototype cyclotron. Supervisor: Jong Seo Chai.

Yunchang Shin

Working Papers

"Pion and Kaon Electromagnetic Form-factors in $SU_R(3) \otimes SU_L(3)$ effective lagrangian" with M. K. Cheon, B. S. Han, K. S. Kim and I. T. Cheon, Eur. Phys. J. **A 9**, 269$\sim$276, (2000).

"A Role of the Axial Vector Mesons on the Photon Production in Heavy Ion Collisions and Their Relevant Decays" with M. K. Cheon, B. S. Han, K. S. Kim and T. K. Choi, Eur. Phys. J. **A 14**, 87$\sim$93, (2002).

"Cold Neutron Energy Dependent production of Ultra-cold Neutrons in Solid Deuterium" F. Atchison *et al*, accepted in Phys. Rev. Lett, (2007).

"Neutronic Design and Measured Performance of the Low Energy Neutron Source (LENS) Target Moderator Reflector Assembly" C. Lavelle *et al*, submitted in Nucl. Instr. and Meth. **A**, (2007).

"A Microscpoic Model for the Neutron Dynamic Structure Factor of Solid Methane in phase II" with W. M. Snow, C. Y. Liu, C. M. Lavelle and D. V. Boxter, **arXiv:0705.0824v3**, to be submitted, (2007).

"The Neutron Energy Spectrum Study from the Phase II Solid Methane Moderator at the LENS Neutron Source" with W. M. Snow, C. M. Lavelle and D. V. Boxter, **arXiv:0711.2948v1**, to be submitted, (2007).

Conference Proceedings

"Pion and Kaon Electromagnetic Form-factors and their related decay in $SU_R(3) \otimes SU_L(3)$ effective lagrangian," with M. K. Cheon, K. S. Kim and T. K. Choi, "Hadron and Nuclei, first international symposium", Frb, 2001 Seoul, Korea, (2001).

"Phase II Solid Methane Scattering Kernel with Comparison to LENS Energy Spectrum Measurement," with W. M. Snow, C. M. Lavelle and D. V. Baxtor, ICANS-XVII, 542, (2005).

The other Papers

"Negative PIG ion source for 13 MeV Cyclotron", with J. H. Hu and J. S. Chai, not published, (2001).

Presentations

"LENS, The Low Energy Neutron Source at Indiana University," International Conference on Precision Measurements with Slow Neutron, NIST, Gaithersburg, MD, April 5 7 (2004)

"Phase II Solid Methane Scattering Kernel with Comparison to LENS Energy Spectrum Measurement," International Collaboration on Advanced Neutron Sources, Santa Fe NM, April 24 29 (2005)

"Solid Oxygen Ultra-cold Neutron Source for Fundamental Physics Experiments," Division of Nuclear Physics Annual Meeting, Nashville, TN, October 25 28 (2006)

"Scattering Kernel for Solid Methane in Phase II," Division of Nuclear Physics Annual Meeting, Nashville, TN, October 25 28 (2006)

Scientific Software

A Mathematica program for the numerical solution of integral eqautions,

NJOY for creating multi-group energy cross section of neutron in solid methane media,

Geant4 for the simulation of transportation of Ultra-cold Neutron,

MCNP for the neutron scattering study in a moderator media.